The Other 99 Percent

Niyayesh Afshordi

A DISSERTATION
PRESENTED TO THE FACULTY
OF PRINCETON UNIVERSITY
IN CANDIDACY FOR THE DEGREE
OF DOCTOR OF PHILOSOPHY

RECOMMENDED FOR ACCEPTANCE
BY THE DEPARTMENT OF
ASTROPHYSICAL SCIENCES

November, 2004

I certify that I have read this thesis and that in my opinion it is fully adequate, in scope and in quality, as a dissertation for the degree of Doctor of Philosophy.

David N. Spergel
(Principal Advisor)

I certify that I have read this thesis and that in my opinion it is fully adequate, in scope and in quality, as a dissertation for the degree of Doctor of Philosophy.

Bruce T. Draine

I certify that I have read this thesis and that in my opinion it is fully adequate, in scope and in quality, as a dissertation for the degree of Doctor of Philosophy.

Lyman A. Page

Approved for the Princeton University Graduate School:

Dean of the Graduate School

For My Parents

Assuredly the creation of the heavens and the earth is greater than the creation of mankind; but most of mankind know not.
— The Quran, 40:57

As far as we can discern, the sole purpose of human existence is to kindle a light of meaning in the darkness of mere being.
— Carl Jung (1875 - 1961)

Acknowledgements

… Then when (Solomon) saw it placed firmly before him, he said: "This is by the grace of my Lord!- to test me whether I am grateful or ungrateful! and if any is grateful, truly his gratitude is (a gain) for his own soul; but if any is ungrateful, truly my Lord is free of all needs, supreme in honor!"

— *from the story of the Queen of Saba, Quran, 27:40*

This thesis puts a formal end to my twenty years of life as a student; twenty years filled with memories; memories identified with people. Those who helped me get through those years, and those who years helped me get through. The tradition calls for me to begin the thesis by acknowledging those who played a significant role in its completion, and yet the tradition does not account for how gross an understatement, that acknowledgement can be.

I should start by thanking my parents, to whom I dedicate this thesis. My father, who spent countless days in cold winters and impossible summers of Iranian deserts, trying to guarantee my and my sisters' education and future, and my mother, who sacrificed her education, and her future, seeing us and helping us through every step of our lives. It is so painful to grow the fruit of your life for twenty years, and yet miss its blossom. Let us hope and pray for a day that man-made borders are only part of history books.

I then thank my elder sister, Setayesh, whose constant support has been so heartwarming through my many cold moments during high school and college, and my younger sister, Parastesh, whose vitality and curiosity have given me so much joy through these years.

My interest in Astronomy started with middle school, but really took off when I discovered the *Kanoon* observatory in Zafarniyeh, Tehran, which gathered amateur astronomers of different groups and ages from all around the city. It is hard to forget the many evenings and days that we spent enjoying the sights of the night sky, and discussing wonders of cosmos. Among the people who I recall from those years is the witty and outgoing director, Mr. Rezaei, the always cheerful, yet knowledgable instructors, Reza Giyahi, Omid Vahhabi, Alireza Movahednezhad, and Mr. Seghri, many of whom I still remain good friends with, along with all the students whose names are mostly beyond my memory. I am grateful to all of them for introducing Astronomy to me, as the interactive science that it is, rather than my solitary nights out on the roof. And speaking of solitary nights, I should also thank my oldest friend, since primary school till now, Behnam Rezaei, who bore with me through some of my less boring nights out on the roof.

By the end of high school, driven by the incredible odyssey of Physics Olympiad, I had turned from an amateur astronomer to an amateur physicist, which would later lay the foundation for my pursuit of professional Astronomy. Those who accompanied me through this amazing journey, from the classrooms of our high school, to the International Physics Olympiad in Oslo, Norway, my good friend Kaveh Khodjasteh, along with the rest of the gang, Farzin Habibbeigi, Sina Valadkhan, Farzan Nikpour, Reza Imani, and Ali Farhang-Mehr will always be parts of the best of my memories. As strange as it may sound, I owe to them whatever confidence that I have left in doing science. Their company is one of the things that I missed the most during my time at Princeton.

Later, at Sharif University, I had the opportunity to interact with the brightest physics students in my country. Among them were Saman Moghimi, Ali Naji, Bahman Roostai, and Sima Ghassemi who helped me adapt to the academic lifestyle through many fruitful scientific discussions and interactions. I am grateful to them, and all my former classmates at Sharif University for creating such a lively atmosphere, and wish them success in their own fields.

This section would not be complete without thanking my many teachers during the past twenty years, many of whom taught me much more than they were supposed to. From my 2nd and 3rd grade teachers (Ms. Mir and Mr. Galavi) who taught me love and integrity, to my high school physics teacher (Mr. Sadeghi) who showed me how to think like a physicist, and to my Electrodynamics teacher at Sharif University (Prof. Arfaei) who demonstrated how to be a physicist with love and integrity. In particular, I am thankful to my instructors at the olympiad camp, Profs. Agha-Mohammadi, Khorrami, Bahman-Abadi, Ejtehadi, Shariati, and Tavalla, who taught me the fundamentals of Physics, with such skill and depth that few teachers are capable of. Their combination of rigor and enthusiasm has been one of the goals that I have always strived to achieve. I am then grateful to Prof. Farhad Ardalan for giving me a position at IPM, which provided my first exposure to a research environment, and to Prof. Reza Mansouri for his many helps through my academic career, including, but not limited to introducing me to General Relativity and Cosmology. Finally, my journey into the world of Astrophysics would have not been possible without the mentorship of Ali Nayeri and Prof. Jalal Samimi, who taught me so many valuable lessons, and provided me with so many opportunities.

My academic life in the United States started at Brown University. I am specially grateful to the chairman of Brown Physics department, Prof. Dave Cutts, and my previous advisor, Prof. Robert Brandenberger, who helped me and my wife through the painstaking US visa application process, and adapting to the new academic environment. Robert has helped us through so many difficult steps of our lives, and will always be our good friend, teacher, and role model.

My last four years, which are the most relevant ones to this thesis, were spent at Peyton Hall, whose residents I have grown to love, cherish, and admire. Most significant of them is my thesis advisor, David Spergel, who was the first to welcome me as a prospective student, and will be the last to see me off to the post-doctoral world. While I will be forever in debt to his scientific guidance, his physical intuition and warm attitude have constantly inspired and encouraged me through these years. I also owe a huge debt to my other advisors at Peyton Hall. Renyue Cen walked this naive graduate student through his first real Astrophysics project. His mastery of both numerical and analytic skills have never stopped impressing me. Bohdan Paczyński, with his incredible discipline, taught me how to endure through the many steps of a research project. Through these years, he has been, without a question, the heart of Peyton Hall's social life, and I hope and pray for his fast recovery from his temporary illness. Finally, Jerry Ostriker, with his unmatched intuition, Scott Tremaine with his transcendent rigor, and Michael Strauss with his masterful knowledge of cosmology will always be my role models as scientists.

The atmosphere of Peyton Hall provides a rare combination of friendliness, cultural diversity, and scientific excellence. Robert Lupton may sound intimidating at first, but he turns out to be one of the most helpful, friendly, and down-to-earth characters at this department. Jeremy Goodman's mathematical logic brings common sense to every scientific discussion. Bruce Draine knows almost everything that you don't, and doesn't hesitate to share it with you. I am indebted to him for being a member of my thesis committee, my thesis reader, and the teacher of his great course on Inter-Stellar Medium. Neta Bahcall, Rich Gott, Jim Gunn, Jill Knapp, and Russel Kulsrud have also touched my life immensely with their open doors, kind attitudes, and unique expertise.

Behind the inter-woven walls of copper, just a short walk from Peyton Hall, is the famous physics department of Princeton University. There you can find some of the greatest cosmologists of the world, namely Paul Steinhardt, and Uros Seljak who have been very helpful to me during these years, as well as Lyman Page who has kindly accepted to be one of the readers of my thesis.

The postdocs are big parts of the social and scientific life at Peyton Hall. I specifically thank Rachel Bean, Olivier Dore, Laurent Eyer, Brenda Frye, Doug Finkbeiner, Pat Hall, Eiichiro Komatsu, Elena Pierpaoli, and Licia Verde for our valuable interactions, scientific and otherwise. Then, there are the students, who make the Peyton basement almost livable. My gratitude goes to my senior peers Hiranya Peiris, Leonid Malyshkin, Roman Rafikov, Arielle Phillips, Bart Pindor, Qinjuan Yu, Eric Ford, and Iskra Strateva for making me feel so welcome during my beginning years here, to the *other* student in my class, Joe Hennawi, for being a good friend and a helpful classmate, and to the younger folks Simon DeDeo, Matt Collinge, Ed Sirko, Nadia Zakamska, Feng Dong, Mario Juric, Xiaoan Wu, Nick Bond, Cullen Blake, Will Serber, Dan Fabrycky, and Khosrow Allaf-Akbari for providing such a warm and interactive environment in the cold basement of Peyton Hall, during the recent years. I am sure that I will miss our memorable daily coffee and tea hours, as well as our weekly Wunch and Thunch gatherings.

I should also thank my great scientific collaborators during these years: Pat McDonald, the Ly-α forest guru from the physics department, Yeong-Shang Loh who helped me through understanding the observers' jargon, Yen-Ting Lin from the University of Illinois, my personal guide to the world of X-ray cluster observations, and Steve Boughn, the expert on the ISW effect.

There are many non-scientists who have made the life at Peyton Hall so fun. There is, of course, my favorite librarian, Jane Holmquist with her always smiley face and helpful hands. Susan Dawson, our great Department Manager, who has handled our financial matters so smoothly. The graduate student secretary, Mindy Lipman, who has so patiently helped me through preparations for my thesis defense. Steve Huston, our sysadmin, who has kept our computers running so skillfully, and finally, Leroy Truehart, our friendly janitor, whose warm smile would start our days.

Last, but by no means least, my love, admiration, and gratitude goes to my wife, Ghazal Geshnizjani. During the last six years, she bore with me through thick and thin, endured my decision to come to Princeton, while she was a graduate student at Brown, cheered my success and protected me through the dark times. Her beauty, passion, and intelligence have always been a source of inspiration to me, and I hope and pray that they remain this way for years to come.

Abstract

There is now overwhelming evidence that only less than one percent of the mass in the universe can be observed via its optical signature. This thesis examines some of the signatures of (optically) invisible components of our universe, which comprise more than *99 percent* of its energy content, namely dark energy ($\sim 70\%$), dark matter ($\sim 25\%$), and hot gas ($\sim 4\%$).

We start by introducing an alternative model for Cold Dark Matter (CDM), which consists of massive Primordial Black Holes (PBH's). We study the imprint of Poisson fluctuations, due to the discrete nature of PBH's, on the cosmological power spectrum. Combining our results with Ly-α forest observations, we arrive at a new upper limit on the mass of PBH's. We then point out that evaporation of haloes with a small of number of PBH's puts a lower cut-off on the mass of CDM haloes.

The Wilkinson Microwave Anisotropy Probe (WMAP) has recently provided us with an all-sky map of Cosmic Microwave Background (CMB) with a resolution of $\sim 0.5^\circ$. The rest of the thesis is devoted to techniques that can be used to extract signatures of dark energy and hot gas from WMAP CMB maps. We first cross-correlate the WMAP maps with the distribution of galaxies in the Two Micron All Sky Survey (2MASS), and demonstrate the presence of Integrated Sachs-Wolfe (ISW) and thermal Sunyaev-Zel'dovich (SZ) effects at large and small angles respectively. In a flat universe, the ISW effect is interpreted as a signature of late time acceleration of the universe, caused by dark energy, while the thermal

SZ effect traces the distribution of hot gas in clusters of galaxies. We go on to consider different aspects of *observing dark energy* via cross-correlating the CMB sky with galaxy surveys, and describe the potential of the method for constraining cosmological parameters. Finally, we devise an optimized filter match method to study the thermal SZ signature of 100 low-redshift X-ray clusters. Applying this method to the WMAP maps, we can put novel constraints on the gas fraction and concentration parameter of the Intra-Cluster Medium (ICM) in these clusters.

Preface

This thesis consists of five chapters. The first chapter is the introduction, which sets the stage for the rest of the thesis, and explains the reason behind the title.

Chapters 2 is already published in *Astrophysical Journal Letters*, and appears only with slight modifications, based on the readers' comments. This chapter was done in collaboration with Patrick McDonald who performed and analyzed the Hydro-PM simulations of the Ly-α forest, and David Spergel who came up with the idea of using Poisson noise as a way of constraining the dark matter particle mass.

Chapters 3 is published in *Physical Review D*, and again appears with slight modifications, based on the readers' comments. My collaborators for this chapter were Yeong-Shang Loh and Michael Strauss who helped me with the use and the interpretation of the observational data used in the treatment.

Chapter 4 is a single author paper (although it heavily relies on comments by those acknowledged below, specially Michael Strauss), which is available on the web, through arXiv preprints, and is submitted to *Physical Review D* for publication.

Finally, Chapter 5 will also be soon submitted for publication. It is done in collaboration with Yen-Ting Lin, who is responsible for the compilation and analysis of the X-ray observations used in the chapter.

The following lists the bibliography for the chapters, collaborators, and individual acknowledgments for each chapter:

Chapter 2

N. Afshordi, P. McDonald, and D. N. Spergel

Primordial Black Holes as Dark Matter: The Power Spectrum and Evaporation of Early Structures

Astrophys. J. **594**, L71 (2003)

arXiv:astro-ph/0302035

PM thanks Nick Gnedin for the hydro-PM code. NA and DNS are grateful to J.P.Ostriker for critical and illuminating discussions. The Ly-α forest simulations were performed at the National Center for Supercomputing Applications.

Chapter 3

N. Afshordi, Y. S. Loh, and M. A. Strauss

Cross-Correlation of the Cosmic Microwave Background with the 2MASS Galaxy Survey: Signatures of Dark Energy, Hot Gas, and Point Sources

Phys. Rev. D **69**, 083524 (2004)

arXiv:astro-ph/0308260

NA wishes to thank David N. Spergel for the supervision of this project and useful discussions. We would also like to thank Eiichiro Komatsu, Andrey Kravstov and Christopher Hirata for illuminating discussions and helpful suggestions, Doug Finkbeiner for help on the analysis of WMAP temperature maps, and R.M. Cutri and Mike Skrutskie on the 2MASS dataset. MAS acknowledges the support of NSF grants ASF-0071091 and AST-0307409.

Chapter 4

N. Afshordi

Integrated Sachs-Wolfe effect in Cross-Correlation: The Observer's Manual

Submitted to Physical Review D
arXiv:astro-ph/0401166

The author wishes to thank Steve Boughn, Yeong-Shang Loh, David Spergel, and Michael Strauss for illuminating discussions and useful comments. This work was originated as response to a question asked by Yeong-Shang Loh, and the author is grateful to him for asking that question.

Chapter 5
N. Afshordi, and Y. Lin
WMAP Constraints on the Intra-Cluster Medium
in preparation

NA wishes to thank David N. Spergel for the supervision of this project.

Contents

Chapter 1

Introduction

Most of the theses written at Princeton are concerned with various aspects of the visible universe. However, as our modern understanding of cosmology develops, it is becoming more and more clear that more than 99% of the energy/mass content of our universe is invisible to our eyes (see Fukugita & Peebles, 2004, for a comprehensive review).

The first evidence for the presence of dark components in our universe came from observations of velocity dispersion of galaxy clusters, based on the spectral Doppler shift of cluster members (Zwicky, 1937). The gravitational mass, required by virial theorem, to sustain the velocity dispersion of large galaxy clusters is about 400 times larger than the mass of stars observed in the cluster members.

Further evidence followed from the investigation of rotation curves in spiral galaxies (Freeman, 1970; Bosma, 1978; Rubin, Thonnard, & Ford, 1980). It turns out that the rotation velocity of stars orbiting in the outskirts of spiral galaxies, again inferred from their observed spectral Doppler shift, requires gravitational masses significantly larger than the mass of the stars observed in the galaxy. This discrepancy seems to increase as one probes larger distances towards the galactic center.

These observations led to the speculation that an invisible species of matter, the so-called *dark matter* (Gunn, 1980), dominates the mass of astronomical objects on galactic and cosmological scales. The 2nd chapter examines a model for dark matter, which consists of massive Primordial Black Holes that form in the radiation dominated phase of the early universe.

A yet more mysterious component of our universe was discovered by mistake. Einstein realized that a static universe of stars was not compatible with equations of classical General Relativity. Motivated by a desire to make the equations compatible with a static universe, Einstein added a constant, the so-called cosmological constant, to the equations, which would resemble a homogeneous component of matter, with constant density and equally large, but *negative pressure*. While this constant has virtually no effect close to dense objects (e.g., earth or sun), on large scales it can cancel self-gravity of ordinary matter, and thus allow a static universe. After Hubble's discovery of cosmological expansion, cosmologists abandoned the static universe model. However, the cosmological constant remained in textbooks on cosmology and general relativity as the simplest modification of Einstein gravity, as well as a pedagogical lesson on the history of science (see Carroll, 2001, for an overview).

Followed by the advent of quantum field theories, and their success in explaining the quantum relativistic interaction of elementary particles, the cosmological constant was re-introduced as the quantum field zero point energy, or the so-called vacuum energy. While the vacuum energy does not affect the particle interactions (and thus cannot be observed directly), it can affect gravity as a cosmological constant. The non-existence of this vacuum energy/cosmological constant, at least at the energy scales expected from high energy physics, is now known as the *cosmological constant problem* (e.g., Weinberg, 1989; Garriga & Vilenkin, 2001).

During the past ten years, our ideas about the cosmological constant changed radically(e.g., Carroll, 2001). Most notably, the observations of high redshift supernovae Ia, combined with the empirical finding that they behave as standard candles, seem to indicate that the Hubble expansion is accelerating, while ordinary gravity can only cause a deceleration (e.g., Riess et al., 2004, and refernces therein). Of course, this observation could be naturally explained by a cosmological constant which dominates the energy density of the universe on cosmological scales. These observations were then complemented by the combination of Cosmic Microwave Background (CMB) anisotropy, and large scale structure observations, which required a homogeneous component of the universe that dominates the average energy density, but does not cluster (e.g., Spergel et al., 2003).

The more generic term of *dark energy* was later invented to accommodate more exotic possibilities (e.g., quintessence, k-essence) for this component, rather than a simple cosmological constant (Peebles & Ratra, 2003). Chapters 3 and 4 discuss the observational signature and theoretical expectations for an independent measure of dark energy, the Integrated Sachs-Wolfe (ISW) effect.

The past few years have witnessed the emergence of a concordance cosmological model, which can explain a host of cosmological observations (e.g., Bahcall et al., 2002). The concordance cosmological model requires $\sim 70\%$ of the energy density of the universe in the form of dark energy, and $\sim 25\%$ in the form of dark matter, leaving only $4-5\%$ room for the ordinary baryonic matter (e.g., Spergel et al., 2003). However, the amount of baryonic matter that is observed via its optical signature (i.e. stars and quasars), or even the amount of baryonic matter that is bound into galaxies is far less than this value ($< 0.5\%$) (e.g., Fukugita & Peebles, 2004, and references therein). Given that both observations of CMB anisotropies, and expectations from Big Bang Nucleosynthesis (BBN), in fact, require a $4-5\%$

density in baryons, the current apparent deficit in the baryon budget of the universe is known as the *missing baryon problem.* It is now believed that the missing baryons are in fact located in a warm inter-galactic plasma (Cen & Ostriker, 1999). Chapters 3 and 5 provide observational evidence for the thermal Sunyaev-Zel'dovich effect, which trace the hot tail of this warm inter-galactic plasma within clusters of galaxies.

Within the history of science, it has been demonstrated over and over again that more careful observations always uncover new components of our universe. The moral of modern cosmology is that the more mysterious a component is, the more of it can be found.

Bibliography

Bahcall, N.A., et al. 1999, Science, 214, 1481

Bosma, A. 1978, Ph.D. Thesis,

Carroll, S. M. 2001, Living Reviews in Relativity, 4, 1

Cen, R. & Ostriker, J. P. 1999, ApJ, 514, 1

Freeman, K. C. 1970, ApJ, 160, 881

Fukugita, M. & Peebles, P. J. E. 2004, ArXiv Astrophysics e-prints, astro-ph/0406095

Garriga, J. & Vilenkin, A. 2001, Phys. Rev. D, 64, 023517

Gunn, J. E. 1980, Royal Society of London Philosophical Transactions Series A, 296, 313

Peebles, P. J. & Ratra, B. 2003, Reviews of Modern Physics, 75, 559

Riess, A. G., et al. 2004, ApJ, 607, 665

Rubin, V. C., Thonnard, N., & Ford, W. K. 1980, ApJ, 238, 471

Spergel, D. N., et al. 2003, ApJS, 148, 175

Weinberg, S. 1989, Reviews of Modern Physics, 61, 1

Zwicky, F. 1937, ApJ, 86, 217

Chapter 2

Primordial Black Holes as Dark Matter

Abstract

We consider the possibility that massive primordial black holes are the dominant form of dark matter. Black hole formation generates entropy fluctuations that add Poisson noise to the matter power spectrum. We use Ly-α forest observations to constrain this Poisson term in the matter power spectrum, then we constrain the mass of black holes to be less than $\sim$ few $\times\, 10^4\, \mathrm{M}_\odot$. We also find that structures with less than $\sim 10^3$ primordial black holes have evaporated by now.

1. Introduction

The nature of Cold Dark Matter (CDM) is one of the most important and profound mysteries in modern cosmology. One of the clues towards solving this mystery is the fact that the Big Bag Nucleosynthesis (BBN) paradigm (e.g., Burles et al. 2001) predicts a much lower density for the baryonic matter (by a factor of $5-10$) than almost all the measurements of the CDM density in the last decade (see

Bahcall et al. 1999 for a review and Spergel et al. 2003 for a discussion of recent CMB constraints). Black holes are an alternative to the most popular candidate for the dark matter: massive, non-baryonic, elementary particles (see Khalil & Munoz 2002 for a recent review). If Primordial Black Holes (PBH's) formed in the early universe, they could become the dominant form of dark matter.

There are various mechanisms proposed for PBH formation: during inflationary reheating (Garcia-Bellido & Linde 1998), from a blue spectrum of primordial density fluctuations (Carr & Lidsey 1993), or during a phase transition in the early universe (e.g., Rubin et al. 2000). The typical mass of PBH's at the formation time can be as large as the mass contained in the Hubble volume, M_H, down to around $10^{-4}M_H$ (Hawke & Stewart 2002). Carr & Hawking (1974) show that there is no physical self-similar growth mode for the PBH's in a radiation gas, and so there will be no significant accretion after PBH formation. However, Bean & Magueijo (2002) speculate that the accretion of quintessence (i.e., a scalar field) into the PBH's could lead to the scaling of the PBH mass with M_H.

In this chapter, we consider PBH's with $10\ \mathrm{M}_\odot < M_{\rm PBH} < 10^6\,\mathrm{M}_\odot$ as the constituents of CDM. The dynamical constraints on such objects has been thoroughly reviewed and discussed by Carr & Sakellariadou (1999). They show that the strongest upper limit on the mass of such compact objects in the galactic halo is $\sim 10^4\,\mathrm{M}_\odot$ which comes from two independent methods: (1) the rate of globular cluster disruptions, and (2) the mass of the galactic nucleus, accumulated due to dynamical friction. However, the globular cluster disruption limit depends on the completely unknown initial number of globular clusters, while the galactic nucleus limit ignores black hole ejection through gravitational slingshot which may prevent mass accumulation at the center (Xu & Ostriker 1994). Therefore we will take a more conservative value of $10^6\,\mathrm{M}_\odot$ as our upper limit. On the lower end, the non-detection of long duration lensing events by the MACHO microlensing experiment excludes the mass range $0.3 - 30\,\mathrm{M}_\odot$ for the halo objects (Alcock et al. 2001). This chapter studies the impact of these PBH's on the large scale structure of the universe, and specifically the signatures of discreteness in CDM. In §2 we study the impact of the Poisson noise due to the discreteness of PBH's on the linear power spectrum. §3 compares the numerical simulations with this linear power spectrum with the observational data of the Ly-α forest power spectrum. This puts an upper limit on the mass of PBH's. In §4 we discuss the effect of evaporation of early structures, which puts a lower cutoff on the mass function of the PBH haloes. Finally, §5 concludes the chapter.

2. The Linear Spectrum

The linear growth of perturbations generated as a result of the generation of PBH's was first studied by Meszaros 1975. This work was later corrected by Freese et al. 1983, and Carr and Silk 1983, as in Meszaros 1975, super-horizon perturbations had an erroneous growth during the radiation dominated era. In this section, we repeat this calculation.

In the following analysis we assume that PBH's form as the result of a phase transition at some temperature T_c, in the radiation dominated era. Furthermore, we will assume that there is no substantial accretion following their formation era and all of their masses are around $\sim M_{\text{PBH}}$. This assumption can be generalized to an extended accretion scenario where T_c marks the end of accretion period (Magueijo and Bean 2002). The black hole density follows

$$\rho_{\text{PBH}} = M_{\text{PBH}} n_{0,\text{PBH}} (1 + \delta_p) \left(\frac{T}{T_c}\right)^3, \tag{2-1}$$

where $n_{0,\mathrm{PBH}}$ is the number density of PBH's, δ_p is the fluctuation in the number of PBH's due to Poisson noise, and the T/T_c factor describes the dilution in PBH density due to cosmic expansion. Since the PBH's are not correlated on acausal distances, one expects that on scales larger than the Hubble radius

$$P_p =< |\delta_p(k)|^2 > n_{0,\mathrm{PBH}}^{-1}. \tag{2-2}$$

For linear perturbations, on large scales, Eq.(2-1) leads to

$$\delta_{\mathrm{PBH}} = \delta_p + \frac{3}{4}\delta_r, \tag{2-3}$$

where the δ_{PBH},δ_p and δ_r are the relative overdensities of PBH's, Poisson fluctuations and radiation, respectively. Since δ_p in Eq.(2-1) is observable *and* constant, one would conclude that the quantity

$$S \equiv \delta_{\mathrm{PBH}} - \frac{3}{4}\delta_r = \delta_p \tag{2-4}$$

is gauge-invariant and conserved on super-horizon scales. Indeed this is the entropy per PBH, which should remain constant, as long as the universe expands adiabatically (e.g. see Mukhanov et al. 1992). The associated perturbations, generated in this way are isocurvature (or entropy) perturbations, as the curvature at large scales is not (immediately) affected by the formation of compact objects at small scale.

As we are assuming that PBH's are the present day Cold Dark Matter (CDM), the overdensity of CDM is given by

$$\delta_{\mathrm{CDM}}(k) = T_{ad}(k)\delta_{i,ad}(k) + T_{iso}(k)S(k), \tag{2-5}$$

where $T_{ad}(k)$ and $T_{iso}(k)$ are the transfer functions for adiabatic and isocurvature perturbations respectively, while $\delta_{i,ad}(k)$ is the initial condition for the adiabatic perturbations. For the following analysis we will use the analytical fits quoted in Bardeen et al. 1986 to the transfer functions. Eq. (2-5) leads to the following power spectrum

$$P_{\rm CDM}(k) = T_{ad}^2(k) P_{i,ad}(k) + T_{iso}^2(k) P_p. \tag{2-6}$$

In this expression,$P_{i,ad}(k) = A\, k^n$ with $n \simeq 1$ is the adiabatic power spectrum which is produced through inflation (or an alternative method of generating scale-invariant adiabatic perturbations), while P_p is given in Eq.(2-2).

One can see that the isocurvature term on the RHS of Eq. (2-2) contributes a constant to the power spectrum as both P_p and

$$T_{iso}(k) = \frac{3}{2}(1+z_{eq})\,{\rm for}\, k \gg a_{eq} H_{eq} \tag{2-7}$$

are independent of k (e.g., Peacock 1998). Note that this is the simple linear growth due to gravitational clustering which is the same for adiabatic fluctuation. Since the power spectrum of adiabatic fluctuations decays as k^{-3} at small scales, one expects to see the signature of this Poisson noise at large k's. Combining Eqs. (2-2),(2-6) and (2-7) gives the power offset

$$\begin{aligned} \Delta P_{\rm CDM} &\simeq \frac{9 M_{\rm PBH}(1+z_{eq})^2}{4\rho_{\rm CDM}} \\ &= 4.63 \left(\frac{M_{\rm PBH}}{10^3 M_\odot}\right) (\Omega_{\rm CDM} h^5)(h^{-1}{\rm Mpc})^3 \end{aligned} \tag{2-8}$$

which is also a lower bound on the matter linear power spectrum.

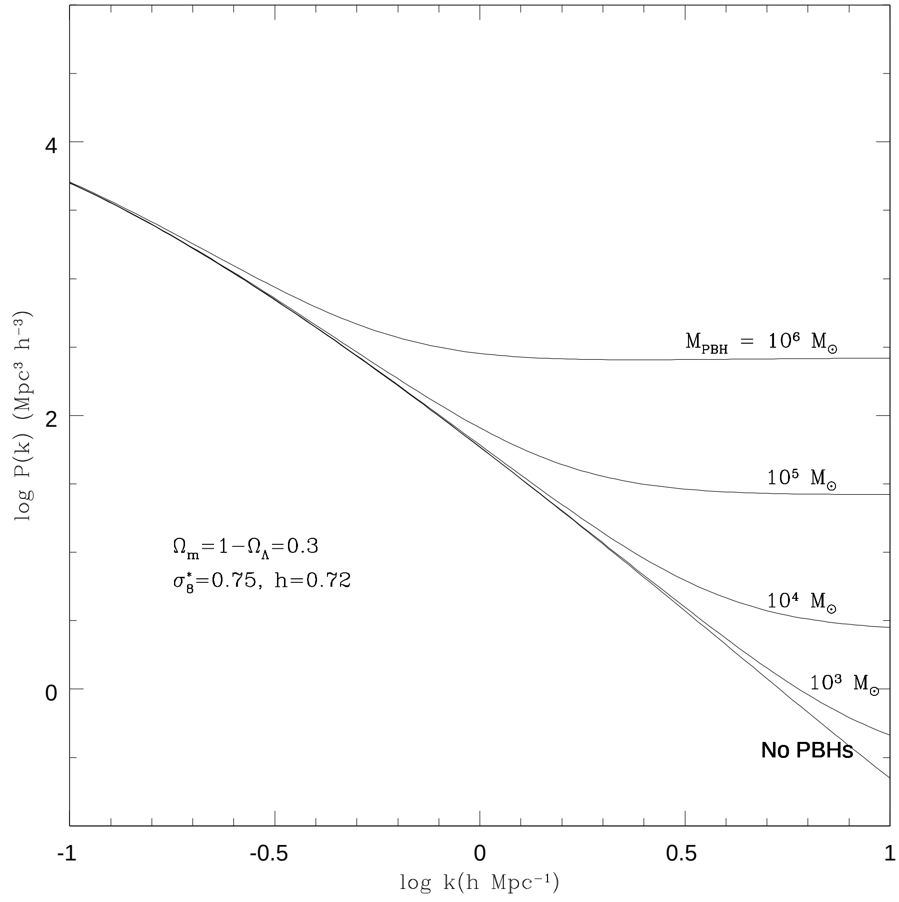

Fig. 2.1.— Linear power spectrum for different masses of the PBH's. σ_8^* is σ_8 for the model without the PBH's and the amplitude of the (initially) adiabatic modes is the same for all models.

Fig. (2.1) shows the linear power spectrum for different masses of the PBH's. We see the Poisson plateau (Eq. 2-8) at large k's which drops with decreasing mass. The impact of this plateau on the Ly-α forest power spectrum is discussed in the next section.

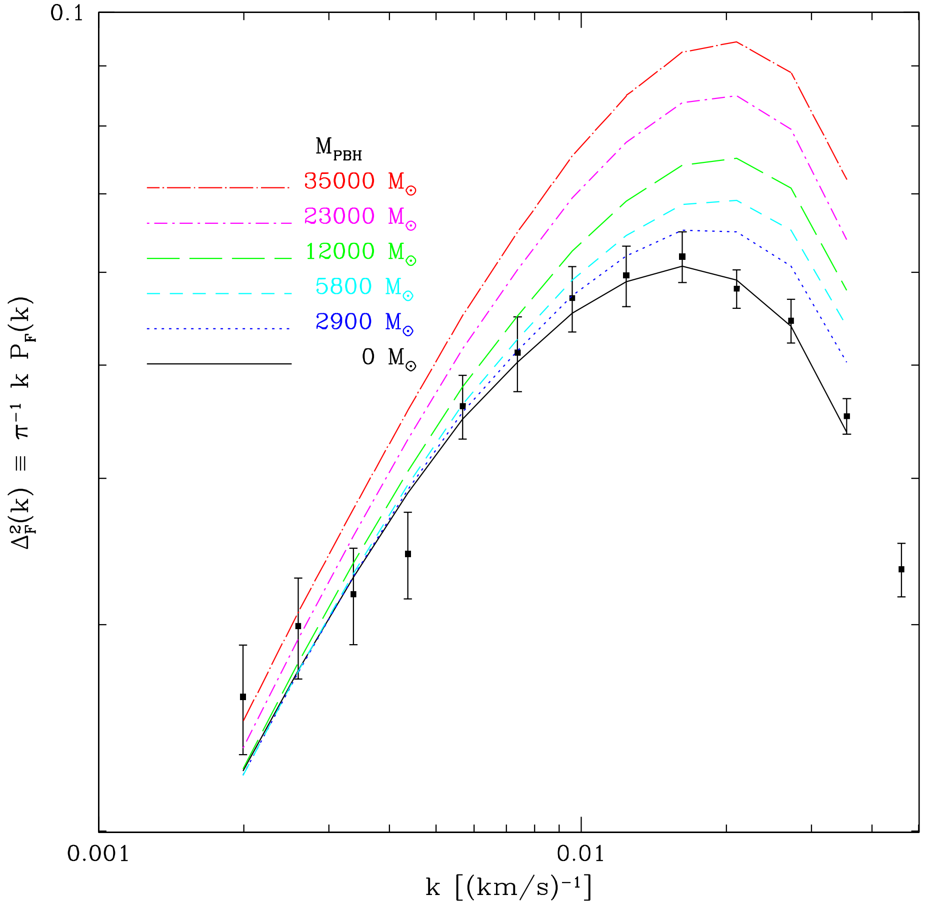

Fig. 2.2.— Influence of PBH's on the Ly-α forest flux power spectrum, $P_F(k)$. The black, solid curve shows our prediction for $P_F(k)$ in a standard ΛCDM model (i.e., no PBH's) in which the amplitude of the linear power spectrum, σ_8^*, was adjusted to match the data points from Croft et al. (2002). The other curves show the predicted $P_F(k)$ when white noise power due to PBH's with various masses is added. The Ly-α forest model parameters and σ_8^* were not adjusted to find a best fit for each mass so the disagreement between the PBH models and the data points does *not* indicate that the models are ruled out.

3. Simulations of Ly-α forest

The lines in Fig. (2.2) show the predicted change in the power spectrum of the Ly-α forest transmitted flux, $P_F(k)$, as M_{PBH} is varied. The points with error bars are $P_F(k)$ measured by Croft et al. (2002) using their fiducial sample ($\bar{z} = 2.72$). The predictions were made using the large set of numerical simulations and the interpolation code described in McDonald et al. (2003). We have not yet performed fully hydrodynamic simulations using PBH power spectra, so our result is based entirely on hydro-PM simulations (e.g., Gnedin & Hui 1998; McDonald, Miralda-Escudé, & Cen 2002; McDonald 2003), where the impact of PBH's is only included as an offset in the initial CDM power spectrum (Eq. 2-8). The curves we show are smooth because the power spectra computed from the simulations have been compressed into the parameters of an analytic fitting formula. The background cosmological model used in Fig. (2.2) is assumed to be flat with a cosmological constant, $\Omega_{\text{CDM}} = 0.26$, $\Omega_b = 0.04$, $h = 0.72$, and $n = 0.9$ (this value of n is close to the best fit found by Croft et al. 2002 for our model). The Ly-α forest model assumed in the simulation is controlled by 3 parameters: the mean transmitted flux fraction in the forest, $\bar{F}$, and the parameters, $T_{1.4}$ and $\gamma - 1$, of a power-law temperature-density relation for the gas in the IGM, $T = T_{1.4}(\Delta/1.4)^{\gamma-1}$, where Δ is the density of the gas in units of the mean density (see McDonald 2003 for a demonstration of the effects of these parameters on the flux power spectrum). The allowed range of each of these parameters has been constrained by independent observations. We use the measurement $\bar{F} = 0.746 \pm 0.018$ from McDonald et al. (2000) and the measurements $T_{1.4} = 20500 \pm 2600$ K and $\gamma - 1 = 0.4 \pm 0.2$ from McDonald et al. (2001). To obtain these values at $z = 2.72$, we interpolated between the redshift bins used by McDonald et al. (2000, 2001). We subtracted 50% of the potential continuum fitting bias they discuss from $\bar{F}$, and add the same number in quadrature to their error on $\bar{F}$. We add 2000 K in quadrature to the error bars on $T_{1.4}$ to help absorb any systematic errors. To produce Fig. (2.2), we fixed these Ly-α forest parameters to their measured values, and fixed the normalization of the initially adiabatic component of the linear power spectrum, σ_8^*, to the value that gives the best fit when $M_{\rm PBH} = 0$. It is not surprising to see that the Ly-α forest power increases dramatically as the white noise power from the PBH's becomes significant on the observed scales.

Fig. (2.2) is not sufficient to place constraints on $M_{\rm PBH}$ because we have not varied any of the other parameters to see if the predicted power can be adjusted to match the observations. To obtain an upper limit on the PBH mass we compute $\chi^2(M_{\rm PBH})$, marginalizing over the amplitude of the linear power and the three Ly-α forest parameters, subject to the observational constraints described above on $\bar{F}$, $T_{1.4}$, and $\gamma-1$. We follow Croft et al. (2002) in using only $P_F(k)$ points with $k < 0.04$ s/km. Defining an upper limit by $\chi^2(M_{\rm PBH}) - \chi^2(0) = 4$, we find $M_{\rm PBH} < 17000\,{\rm M}_\odot$. Fig. (2.3) shows how this limit is obtained. The temperature-density relation parameters play no role, but $\bar{F}$ is important. As $M_{\rm PBH}$ increases, the best fit value of $\bar{F}$ also increases until this trend is halted by the external constraint on $\bar{F}$. The effect of the increase in $\bar{F}$ is to reduce $P_F(k)$ (McDonald 2003), counteracting the increase in power due to $M_{\rm PBH}$. Finally, the unconstrained parameter σ_8^* also increases with $M_{\rm PBH}$, further decreasing the power on small scales while increasing $P_F(k)$ on large scales (see McDonald 2003; this freedom to adjust the tilt of $P_F(k)$ is significant – with σ_8^* fixed we find $M_{\rm PBH} < 5800\,{\rm M}_\odot$).

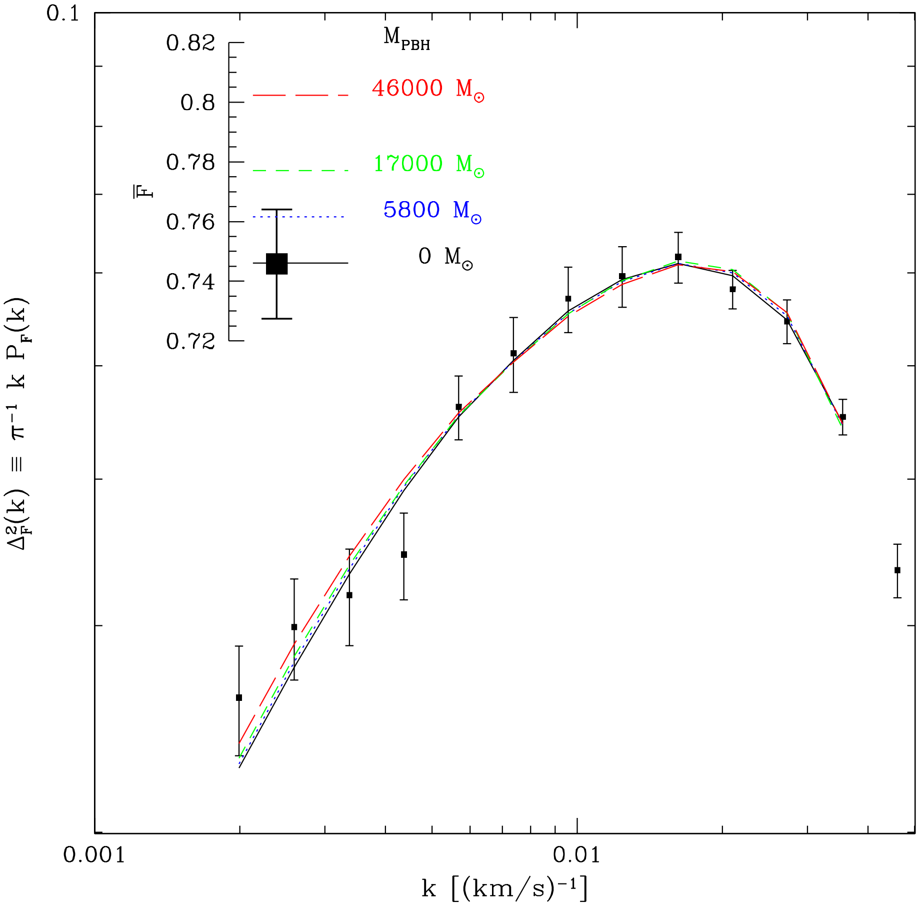

Fig. 2.3.— Joint fits to the observed Ly-α forest mean absorption level, $\bar{F}$, and power spectrum, $P_F(k)$, for several values of the PBH mass. Curves show the best predicted $P_F(k)$ for each value of $M_{\rm PBH}$, determined by a χ^2 minimization over 4 free parameters: σ_8^*, $\bar{F}$, $T_{1.4}$, and $\gamma - 1$. The best fit values of $\bar{F}$ for the different values of $M_{\rm PBH}$ are shown by the labeled horizontal lines. The large square is the measured value of $\bar{F}$ from McDonald et al. (2000), while the power spectrum data points are from Croft et al. (2002).

Fig. (2.3) may at first appear unconvincing to the reader unfamiliar with the Ly-α forest; however, the result is ultimately simple to understand. In Fig. (2.1) we see that the white noise power begins to dominate on the scales to which the Ly-α forest is sensitive when $M_{\rm PBH} \sim 10000 M_\odot$ (note that 1 comoving Mpc/h = 108 km/s at $z = 2.72$ in our model)[1]. As $M_{\rm PBH}$ increases there is simply too much power on the scale of the Ly-α forest to produce the observed level of fluctuations. Increasing $\bar{F}$ can cancel some of the effect but the size of the increase is limited because $\bar{F}$ is directly observable.

A factor of ~ 2 relaxation in the upper bound seems unlikely but not inconceivable. For example, if we arbitrarily increase the error bar on $\bar{F}$ to ± 0.03, the limit we derive is $M_{\rm PBH} < 41000 M_\odot$. The limit is $M_{\rm PBH} < 37000 M_\odot$ if we arbitrarily decrease the predicted $P_F(k)$ by 10% for all models. The assumed value of n has no effect on the result (we obtain $M_{\rm PBH} < 18000 M_\odot$ using $n = 1$). Equation (2-8) and our assumed cosmological model were used to compute $M_{\rm PBH}$.

4. Early Structures and Relaxation Effects

So, apart from the Poisson noise, is there any difference between the gravitational clustering of the conventional CDM (WIMP particles) and PBH's? The answer is yes. The collisional relaxation time for a gravitational system is of the order of the number of particles, times the dynamical time of the system. Therefore, one expects the relaxation related effects, e.g. evaporation and core collapse, to happen faster for systems with smaller number of particles. As the structures form bottom-up in a hierarchical structure formation scenario (and even more so in the presence of

---

[1] We remind the reader that the Ly-α forest only constrains the power spectrum in km/s units at a given redshift

PBH's as the spectrum is bluer), and the dynamical time for cosmological haloes is of the order of the age of the universe, such effects may be important only for the first structures, that form right after the recombination era, which have the smallest number of PBH's.

The possibility of small sub-haloes of compact objects in the galactic halo was first studied in Carr and Lacey (1987). Various dynamical constraints on such sub-haloes, including the evaporation limit, are reviewed in Carr and Sakellariadou (1999). In what follows, we implement this evaporation limit with the Poisson fluctuations of §2 as the seed for the formation of these sub-haloes.

Let us make a simple estimate of how evaporation of early structures sets a lower limit on the mass of virialized objects. The evaporation time of an isolated cluster can be estimated using

$$t_{evap} \sim 300 t_{rel} \sim 300 \left[\frac{0.14N}{\ln(0.14N)}\right] \sqrt{\frac{r_h^3}{GM}}, \tag{2-9}$$

(see Binney & Tremaine 1987), where the subscripts, "*evap*" and "*rel*" refer to the characteristic times, subsequently associated with the evaporation and relaxation of the structure, while N and r_h are the number of particles and the median radius, respectively. To relate r_h to the formation time, for simplicity, we consider a truncated singular isothermal sphere which within the spherical collapse model (e.g., Afshordi & Cen 2002) yields

$$r_h \simeq \frac{2GM}{15\sigma_v^2} \simeq (2GM)^{1/3} \left(\frac{t_f}{27\pi}\right)^{2/3}, \tag{2-10}$$

where t_f is the formation time of the object. Combining this with Eq.(2-9) gives

$$t_{evap} \simeq \left[\frac{0.7N}{\ln(0.14N)}\right] t_f. \tag{2-11}$$

The next assumption is that the approximate formation time of the structure is when the variance of fluctuations at the mass scale of the structure $\sigma(M)$ is around the critical overdensity in the spherical collapse model, δ_c (Gunn & Gott 1972),

$$\sigma(M)|_{\text{form}} \sim \delta_c \simeq 1.67. \tag{2-12}$$

Based on the calculations of §2, $\sigma(M)$, which is dominated by the Poisson noise at the small scales, is given by

$$\sigma^2(M) \simeq \frac{M_{\text{PBH}}}{M}\left[\frac{3}{2}\left(\frac{1+z_{eq}}{1+z}\right)\right]^2, \tag{2-13}$$

neglecting a late time cosmological constant which is not important at the formation time of the early structures. Now, combining Eqs.(2-11)-(2-13) with

$$\frac{t}{t_f} \simeq \Omega_m^{0.2}\left(\frac{1+z_f}{1+z}\right)^{3/2}, \tag{2-14}$$

for a flat universe, gives the minimum mass for the structure not to evaporate

$$\begin{aligned} M_{\min} &= N_{\min} M_{\text{PBH}} \\ &\sim M_{\text{PBH}}\left[\frac{3(1+z_{eq})}{2\delta_c(1+z)}\right]^{6/7}\left[\frac{\Omega_m^{0.2}\ln(0.14N_{\min})}{0.7}\right]^{4/7} \\ &\simeq 3\times 10^3\, M_{\text{PBH}}(1+z)^{-1}\left(\frac{\Omega_m}{0.3}\right)\left(\frac{h}{0.7}\right)^{12/7}, \end{aligned} \tag{2-15}$$

and consequently, the structures with $M < M_{\min}$ should evaporate by redshift z.

This calculation may be an underestimate of $M_{\min}$ since Eq.(2-9) is valid for an isolated object and ignores tidal effects. In general, tidal stripping can decrease t_{evap} significantly (by a factor of 5-10). However, accretion, on the other hand, can slow down the net mass loss rate of the structure and hence has a reverse effect. In reality, the exact lower limit will probably depend on the environment of the structures.

5. Conclusions

We have studied the possibility of having CDM in the form of PBH's (or any other massive compact object) and its impact on the large scale structure of the universe. We see that the simple Poisson noise, enhanced by gravitational clustering in the matter dominated era, leads to a plateau in the power spectrum at large wave numbers (see Fig. 2.1). Comparison of numerical simulations of Ly-α forest with the current observational data rules out the PBH masses larger than few $\times\, 10^4\,\mathrm{M}_\odot$. This leaves a small window for PBH's between this limit and the gravitational lensing limit of 30 $\mathrm{M}_\odot$. Improved Lyman-α measurements and future microlensing surveys should be able to close this window and either detect the effects of PBH's or rule out PBH's with masses above 0.3 $\mathrm{M}_\odot$ as the dominant component of the dark matter. The discrete nature of the PBH's can also lead to the evaporation of small (early) structures. A simple estimate shows that this puts a lower limit of about $10^3 M_{\rm PBH}$ on the mass of small structures.

Bibliography

Afshordi, N., & Cen, R. 2002, ApJ 564, 669.

Bahcall, N.A., Ostriker, J.P., Perlmutter, S., and Steinhardt, P.J. 1999, Science, 214, 1481.

Bardeen, J. M., Bond, J.R., Kaiser, N., & Szalay, A.S. 1986, ApJ, 304, 15.

Bean, R., & Magueijo, J. 2002, Phys.Rev. D66, 063505.

Binney, J., & Tremaine, S 1987, *Galactic Dynamics*, Princeton University Press.

Burles, S., Nollett, K.M., & Turner, M.S. 2001, ApJL 552, L1.

Carr, B.J., & Hawking, S.W. 1974, MNRAS, 168, 399.

Carr, B.J., & Lacey, C.G. 1987, ApJ, 316, 23.

Carr, B.J., & Lidsey,J.E. 1993, Phys. Rev. D48, 543C.

Carr, B.J., & Sakellariadou, M. 1999, ApJ, 516, 195.

Carr, B.J., & Silk, J. 1983, ApJ, 268, 1.

Croft, R. A. C., Weinberg, D. H., Bolte, M., Burles, S., Hernquist, L., Katz, N., Kirkman, D., & Tytler, D. 2002, ApJ, 581, 20.

Freese, K., Price, R., & Schramm, D.N. 1983, ApJ, 275, 405.

Garcia-Bellido, J., & Linde, A. 1998, Phys. Rev. D57, 6075G .

Gnedin, N. Y. & Hui, L. 1998, MNRAS, 296, 44.

Gunn, J.E. & Gott, J.R. 1972, ApJ 176, 1.

Hawke, I., & Stewart, J.M. 2002, Class. Quant. Grav., 19, 3687.

Khalil, S., & Munoz, C. 2002, Contemp.Phys. 43, 51.

Peacock, J.A. 1998, *Cosmological Physics*, Cambridge University Press.

McDonald, P. 2003, ApJ, in press (astro-ph/010806)

McDonald, P., Miralda-Escudé, J., & Cen, R. 2002, ApJ, ApJ, 580, 42.

McDonald, P., Miralda-Escudé, J., Rauch, M., Sargent, W. L. W., Barlow, T. A., Cen, R., & Ostriker, J. P. 2000, ApJ, 543, 1.

McDonald, P., Miralda-Escudé, J., Rauch, M., Sargent, W. L. W., Barlow, T. A., & Cen, R. 2001, ApJ, 562, 52.

McDonald, P., et al. 2003, in preparation

Meszaros, P. 1975, A&A, 38, 5.

Mukhanov, V.F., Feldman, H.A, & Brandenberger, R.H. 1992, Phys. Rep. 215, 203.

Rubin, S.G., Khlopov, M.Yu., & Sakharov, A.S. 2000, Grav.Cosmol. S6, 1.

Spergel, D. N., et al. 2003, ApJS, 148, 175

Xu, G., & Ostriker, J.P. 1994, ApJ 437, 184.

Chapter 3

Cross-Correlating the CMB with the 2MASS Galaxy Survey

Abstract

We cross-correlate the Cosmic Microwave Background (CMB) temperature anisotropies observed by the Wilkinson Microwave Anisotropy Probe (WMAP) with the projected distribution of extended sources in the Two Micron All Sky Survey (2MASS). By modeling the theoretical expectation for this signal, we extract the signatures of dark energy (Integrated Sachs-Wolfe effect;ISW), hot gas (thermal Sunyaev-Zel'dovich effect;thermal SZ), and microwave point sources in the cross-correlation. Our strongest signal is the thermal SZ, at the $3.1 - 3.7\sigma$ level (after marginalizing over other signals), which is consistent with the theoretical prediction based on observations of X-ray clusters. We also see the ISW signal at the 2.5σ level, which is consistent with the expected value for the concordance ΛCDM cosmology, and is an independent signature of the presence of dark energy in the universe. Nevertheless, as the ISW signal is observed at large angles, it may be contaminated by Galactic or observational systematics. Finally, using its spatial and

spectral characteristics, we can isolate the signature of microwave point sources at the 2.7σ level.

1. Introduction

The recently released WMAP results (Bennett et al. , 2003a) constrain our cosmology with an unprecedented accuracy. Most of these constraints come from the linear fossils of the early universe which have been preserved in the temperature anisotropies of the CMB. These are the ones that can be easily understood and dealt with, within the framework of linear perturbation theory. However, there are also imprints of the late universe which could be seen in the WMAP results. Most notable was the measurement of the optical depth to the surface of last scattering, $\tau \simeq 0.17$, which implied an early reionization of the universe.

Can we extract more about the late universe from WMAP? Various secondary effects have been studied in the literature (see e.g., Hu & Dodelson, 2002). The main secondary anisotropy at large angles is the so-called Integrated Sachs-Wolfe (ISW) effect (Sachs & Wolfe, 1967), which is a signature of the decay of the gravitational potential at large scales. This could be either a result of spatial curvature, or presence of a component with negative pressure, the so-called dark energy, in the universe (Peebles & Ratra, 2003). Since WMAP (assuming a prior on the Hubble constant; Spergel et al., 2003) has constrained the deviation from flatness to less than 4% , the ISW effect may be interpreted as a signature of dark energy. At smaller angles, the dominant source of secondary anisotropy is the thermal Sunyaev-Zel'dovich (SZ) effect (Sunyaev & Zel'dovich, 1972), which is due to scattering of CMB photons by hot gas in the universe.

However, none of these effects can make a significant contribution to the CMB power spectrum below $\ell \sim 1000$, and thus they are undetectable by WMAP alone. One possible avenue is cross-correlating CMB anisotropies with a tracer of the density in the late universe (Crittenden & Turok, 1996; Peiris & Spergel, 2000; Cooray, 2002). This was first done by Boughn & Crittenden (2002) who cross-correlated the COBE/DMR map (Bennett et al. , 1996) with the NRAO VLA Sky Survey (NVSS; Condon et al. , 1998). After the release of WMAP, different groups cross-correlated the WMAP temperature maps with various tracers of the low-redshift universe. This was first done with the ROSAT X-ray map (Diego et al. , 2003), where a non-detection of the thermal SZ effect puts a constraint on the hot gas content of the universe. Hernandez-Monteagudo & Rubino-Martin (2003) and Bennett et al. (2003b) claim a 2-5σ detection of an SZ signal by filtering WMAP maps via templates made using known X-ray cluster catalogs. Nolta et al. (2003) looked at the cross-correlation with the NVSS radio galaxy survey, while Boughn & Crittenden (2003) repeated the exercise for NVSS, as well as the HEAO-1 hard X-ray background survey, both of which trace the universe around redshift of ~ 1. Both groups found their result to be consistent with the expected ISW signal for the WMAP concordance cosmology (Bennett et al. , 2003a), i.e., a flat ΛCDM universe with $\Omega_m \simeq 0.3$, at the $2-3\sigma$ level. Their result is consistent with the ΛCDM paradigm which puts most of the energy of the universe in dark energy (Peebles & Ratra, 2003).

More recently, Fosalba, Gaztañaga, & Castander (2003) cross-correlated WMAP with the APM galaxy survey (Madox et al. , 1990) which traces the galaxy distribution at $z \sim 0.15$. This led to an apparent detection of both the thermal SZ and ISW signals. However, the fact that they use a jack-knife covariance matrix to estimate the strength of their signal, while their jack-knife errors are significantly smaller than those obtained by Monte-Carlo realizations of the CMB sky (compare their Figure 2 and Figure 3) weakens the significance of their claim. Indeed, as we argue below (see §3.3), using Monte-Carlo realizations of the CMB sky is the only reliable way to estimate a covariance matrix if the survey does not cover the whole sky.

Myers et al. (2003) cross-correlates the highest frequency band (W-band) of the WMAP with the ACO cluster survey (Abell et al. , 1989), as well as the galaxy groups and clusters in the APM galaxy survey. They claim a 2.6σ detection of temperature decrement on angles less than $0.5°$, which they associate with the thermal SZ effect. However they only consider the Poisson noise in their cluster distribution as their source of error. This underestimates the error due to large spatial correlations (or cosmic variance) in the cluster distribution (see §3.3). Myers et al. (2003) also studies the cross-correlation of the W-band with the NVSS radio sources below a degree and claims a positive correlation at the scale of the W-band resolution. This may imply a possible contamination of the ISW signal detection in Boughn & Crittenden (2003) and Nolta et al. (2003). However the achromatic nature of this correlation makes this unlikely (Boughn, 2003).

Finally, Scranton et al. (2003) and Fosalba & Gaztañaga (2004) repeated the cross-correlation analysis with the 3400 and 2000 square degrees, respectively, of the Sloan Digital Sky Survey (York et al., 2000). Both groups claim detection of a positive signal, but they both suffer from the inconsistency of their jack-knife and Monte-Carlo errors.

The 2MASS Extended Source Catalog (XSC; Jarrett et al. , 2000) is a full sky, near infrared survey of galaxies whose median redshift is around $z \sim 0.1$. The survey has reliable and uniform photometry of about 1 million galaxies, and is complete, at the 90% level for K-magnitudes brighter than 14, over $\sim 70\%$ of the sky. The large area coverage and number of galaxies makes the 2MASS XSC a good tracer of the ISW and SZ signals in the cross-correlation with the CMB.

In this paper, we study the cross-correlation of the WMAP Q,V and W bands with four different K-magnitude bins of the 2MASS Extended Source Catalog, and fit it with a three component model which includes the ISW, thermal SZ effects and microwave sources. We compare our findings with the theoretical expectations from the WMAP+CBI+ACBAR+2dF+Ly-α best fit cosmological model (WMAP concordance model from here on; see Table 3 in Bennett et al. , 2003a), which is a flat universe with, $\Omega_m = 0.27, \Omega_b = 0.044, h = 0.71$, and $\sigma_8 = 0.84$. We also assume their values of $n_s = 0.93$, and $dn_s/d\ln k = -0.031$ for the spectral index and its running at $k = 0.05\,\mathrm{Mpc}$ (Spergel et al., 2003).

We briefly describe the relevant secondary anisotropies of the CMB in §2. §3 describes the properties of the cross-correlation of two random fields, projected on the sky. §4 summarizes the relevant information on the WMAP temperature maps and the 2MASS Extended Source Catalog. §5 describes our results and possible systematics, and §6 concludes the paper.

2. What are the secondary anisotropies?

The dominant nature of the Cosmic Microwave Background (CMB) fluctuations, at angles larger than ~ 0.1 degree, is primordial, which makes CMB a snapshot of the universe at radiation-matter decoupling, around redshift of ~ 1000. However, a small part of these fluctuations can be generated as the photons travel through the low redshift universe. These are the so-called secondary anisotropies. In this section, we go through the three effects which should dominate the WMAP/2MASS cross-correlation.

2.1. Integrated Sachs-Wolfe effect

The first is the Integrated Sachs-Wolfe (ISW) effect (Sachs & Wolfe, 1967) which is caused by the time variation in the cosmic gravitational potential, Φ. For a flat universe, the anisotropy due to the ISW effect is an integral over the conformal time η

$$\delta_{\mathrm{ISW}}(\hat{\mathbf{n}}) \;=\; 2\int \Phi^{'}[(\eta_0-\eta)\hat{\mathbf{n}},\eta]\; d\eta, \tag{3-1}$$

where $\Phi^{'} \equiv \partial\Phi/\partial\eta$, and $\hat{\mathbf{n}}$ is unit vector in the line of sight. The linear metric is assumed to be

$$ds^2 = a^2(\eta)\{[1+2\Phi(\mathbf{x},\eta)]d\eta^2 - [1-2\Phi(\mathbf{x},\eta)]\mathbf{dx}\cdot\mathbf{dx}\}, \tag{3-2}$$

and η_0 is the conformal time at the present.

In a flat universe, the gravitational potential Φ is constant for a fixed equation of state and therefore observation of an ISW effect is an indicator of a change in the equation of state of the universe. Assuming that this change is due to an extra component in the matter content of the universe, the so-called dark energy, this component should have a negative pressure to become important at late times (Peebles & Ratra, 2003). Therefore, observation of an ISW effect in a flat universe is a signature of dark energy.

The ISW effect is observed at large angular scales because most of the power in the fluctuations of Φ is at large scales. Additionally, the fluctuations at small angles tend to cancel out due to the integration over the line of sight.

2.2. Thermal Sunyaev-Zel'dovich effect

The other significant source of secondary anisotropies is the so-called thermal Sunyaev-Zel'dovich (SZ) effect (Sunyaev & Zel'dovich, 1972), which is caused by the scattering of CMB photons off the hot electrons of the intra-cluster medium. This secondary anisotropy is frequency dependent, i.e. it cannot be associated with a single change in temperature. If we define a frequency dependent $T(\nu)$ so that $I_B[\nu; T(\nu)] = I(\nu)$, where $I(\nu)$ is the CMB intensity and $I_B[\nu; T]$ is the black-body spectrum at temperature T, the SZ anisotropy takes the form

$$\frac{\delta T(\nu)}{T(\nu)} = -\frac{\sigma_T f(x)}{m_e c} \int \delta p_e[(\eta_0 - \eta)\hat{\mathbf{n}}, \eta] a(\eta)\, d\eta, \tag{3-3}$$

where

$$x \equiv h\nu/(k_B T_{\rm CMB}) \text{ and } f(x) \equiv 4 - x\coth(x/2), \tag{3-4}$$

and p_e is the electron pressure. Assuming a linear pressure bias with respect to the matter overdensity δ_m:

$$\frac{\delta p_e}{p_e} = b_p \delta_m, \tag{3-5}$$

Eq.(3-3) can be written as

$$\delta_{\rm SZ}(\nu) \equiv \frac{\delta T(\nu)}{T(\nu)} = -F(x) \int \tilde{T}_e \delta_m \frac{H_0 d\eta}{a^2(\eta)}, \tag{3-6}$$

where

$$\tilde{T}_e = b_p \bar{T}_e,$$
$$F(x) = \tfrac{n_e k_B \sigma_T f(x)}{4 m_e c H_0} = (1.16 \times 10^{-4} \text{keV}^{-1}) \Omega_b h f(x), \tag{3-7}$$

and $\bar{T}_e$ and n_e are the average temperature and the comoving density of (all) electrons, respectively. In Appendix A, we make an analytic estimate for $\tilde{T}_e$, based on the mass function and mass-temperature relation of galaxy clusters.

2.3. Microwave Sources

Although technically they are not secondary anisotropies, microwave sources may contribute to the cross-correlation signal, as they are potentially observable by both WMAP and 2MASS. For simplicity, we associate an average microwave luminosity with all 2MASS sources. We can relax this assumption by taking this luminosity to be a free parameter for each magnitude bin, and/or removing the clustering of the point sources. As we discuss in §5.3, neither of these change our results significantly.

For the microwave spectrum in different WMAP frequencies, we try both a steeply falling antenna temperature $\propto 1/\nu^{2-3}$ (consistent with WMAP point sources Bennett et al. , 2003b) and a Milky Way type spectrum which we obtain from the WMAP observations of the Galactic foreground (Bennett et al. , 2003b).

In Appendix B, assuming an exponential surface emissivity with a scale length of 5 kpc for the Galactic disk and a small disk thickness, we use the Galactic latitude dependence of the WMAP temperature to determine the luminosity per unit frequency of the Milky Way (Eq. B6) in different WMAP bands:

$$L^*_Q = 2.0 \times 10^{27} \text{ erg}\,\text{s}^{-1}\,\text{Hz}^{-1},$$

$$L^*_V = 2.1 \times 10^{27} \text{ erg}\,\text{s}^{-1}\,\text{Hz}^{-1},$$

$$\text{and } L^*_W = 4.9 \times 10^{27} \text{ erg}\,\text{s}^{-1}\,\text{Hz}^{-1}. \tag{B6}$$

These values are within 50% of the observed WMAP luminosity of the Andromeda galaxy(see Appendix B) [1]. In §5.3, we compare the observed average luminosity of the 2MASS sources to these numbers (see Table 3.2).

---

[1] We thank Doug Finkbeiner for extracting the fluxes of Andromeda in WMAP temperature maps.

The contribution to the CMB anisotropy due to Point Sources (see Eq.B2) is given by

$$\delta_{PS}(\hat{\mathbf{n}}) = \frac{\delta T(\hat{\mathbf{n}})}{T} = \frac{2\pi\hbar^2 c^2 \sinh^2(x/2) L_\nu(x)}{x^4 (k_B T_{\rm CMB})^3} \int dr \left(\frac{r}{d_L(r)}\right)^2 n_c(r)\delta_g(r, \hat{\mathbf{n}}), \qquad (3\text{-}8)$$

where $L_\nu(x)$ is the effective luminosity per unit frequency within of the WMAP band (Bennett et al. , 2003a), $n_c(r)$ is the average comoving number density of the survey galaxies, d_L is luminosity distance, and δ_g is the galaxy overdensity.

3. The cross-correlation power spectrum

3.1. The Expected Signal

We first develop the theoretical expectation value of the cross-correlation of two random fields, projected on the sky. Let us consider two random fields $A(\mathbf{x})$ and $B(\mathbf{x})$ with their Fourier transforms defined as

$$A_{\mathbf{k}} = \int \mathbf{d^3x}\; e^{-i\mathbf{k.x}} A(\mathbf{x}), \text{ and } B_{\mathbf{k}} = \int \mathbf{d^3x}\; e^{-i\mathbf{k.x}} B(\mathbf{x}). \qquad (3\text{-}9)$$

The cross-correlation power spectrum, $P_{AB}(k)$ is defined by

$$\langle A_{\mathbf{k_1}} B_{\mathbf{k_2}} \rangle \;=\; (2\pi)^3 \delta^{\mathbf{3}}(\mathbf{k_1} - \mathbf{k_2}) P_{AB}(k_1). \qquad (3\text{-}10)$$

The projections of A and B on the sky are defined using F_A and F_B projection kernels

$$\tilde{A}(\hat{\mathbf{n}}) \;=\; \int dr\; F_A(r) A(r\hat{\mathbf{n}}), \text{ and } \tilde{B}(\hat{\mathbf{n}}) \;=\; \int dr\; F_B(r) B(r\hat{\mathbf{n}}). \qquad (3\text{-}11)$$

For the secondary temperature anisotropies, these kernels were given in Eqs. (3-1), (3-6), and (3-8). For the projected galaxy overdensity, this kernel is

$$F_g(r) = \frac{r^2\; n_c(r)}{\int dr'\; r'^2\; n_c(r')}. \qquad (3\text{-}12)$$

For our treatment, we assume a constant galaxy bias, b_g, which relates the galaxy fluctuations, δ_g, to the overall matter density fluctuations δ_m, up to a shot noise δ_p

$$\delta_g = b_g \delta_m + \delta_p. \tag{3-13}$$

In this work, we constrain the galaxy bias, b_g, by comparing the auto-correlation of the galaxies with the expected matter auto-correlation in our cosmological model. Our bias, therefore, is model dependent.

Now, expanding $\tilde{A}$ and $\tilde{B}$ in terms of spherical harmonics, the cross-power spectrum, $C_{AB}(\ell)$ is defined as

$$\begin{aligned} C_{AB}(\ell) &\equiv \langle \tilde{A}_{\ell m} \tilde{B}^*_{\ell m} \rangle \\ &= \textstyle\int dr_1 dr_2 F_A(r_1) F_B(r_2) \times \\ &\textstyle\int \frac{\mathbf{d^3k}}{(2\pi)^3} P_{AB}(k)(4\pi)^2 j_\ell(kr_1) j_\ell(kr_2) Y_{\ell m}(\hat{\mathbf{k}}) Y^*_{\ell m}(\hat{\mathbf{k}}) \\ &= \textstyle\int dr_1 dr_2 F_A(r_1) F_B(r_2) \int \frac{2k^2 dk}{\pi} j_\ell(kr_1) j_\ell(kr_2) P_{AB}(k), \end{aligned} \tag{3-14}$$

where j_ℓ's are the spherical Bessel functions of rank ℓ and $Y_{\ell m}$'s are the spherical harmonics.

To proceed further, we use the small angle (large ℓ) approximation for the spherical Bessel functions

$$j_\ell(x) = \sqrt{\frac{\pi}{2\ell+1}} [\delta_{\rm Dirac}(\ell + \frac{1}{2} - x) + {\rm O}(\ell^{-2})], \tag{3-15}$$

which yields

$$C_{AB}(\ell) = \int \frac{dr}{r^2} F_A(r) F_B(r) P_{AB}\left(\frac{\ell + 1/2}{r}\right) \cdot [1 + {\rm O}(\ell^{-2})]. \tag{3-16}$$

This is the so called Limber equation (Limber, 1954). As we do not use the quadrupole due to its large Galactic contamination, the smallest value of ℓ that we use is 3. Direct integration of Eq. (3-14) (for the ISW signal which is dominant for low ℓ's, see Fig. 3.7) shows that the Limber equation overestimates the cross-power by less than 2-3% at $\ell = 3$, which is negligible compared to the minimum cosmic variance error (about 40%, see §3.2) at this multipole. Therefore, the Limber equation is an accurate estimator of the theoretical power spectrum.

Now we can substitute the results of §2 (Eqs. 3-1, 3-6, 3-8 and 3-12) into Eq.(3-16) which yields

$$C_{gT}(x,\ell) = \frac{b_g}{\int dr\ r^2 n_c(r)} \int dr\ n_c(r) \{ 2P_{\Phi',m}\left(\frac{\ell+1/2}{r}\right) \\ -\left[F(x)\tilde{T}_e H_0 (1+z)^2 - \frac{2\pi\hbar^2 c^2 \sinh^2(x/2) b_g L_\nu(x)}{x^4 (k_B T_{\rm CMB})^3 (1+z)^2}\right] P\left(\frac{\ell+1/2}{r}\right)\}, \tag{3-17}$$

where $P(k)$ is the matter power spectrum, z is the redshift, and x is defined in Eq.(3-4). The terms in Eq.(3-17) are the ISW, SZ and Point Source contributions respectively. Since the ISW effect is only important at large scales, the cross-power of the gravitational potential derivative with matter fluctuations can be expressed in terms of the matter power spectrum, using the Poisson equation and linear perturbation theory, and thus we end up with

$$C_{gT}(x,\ell) = \frac{b_g}{\int dr\ r^2 n_c(r)} \int dr\ n_c(r) \{ -3H_0^2 \Omega_m \frac{r^2}{(\ell+1/2)^2} \cdot \frac{g'}{g}(1+z) \\ -F(x)\tilde{T}_e (1+z)^2 + \frac{2\pi\hbar^2 c^2 \sinh^2(x/2) b_g L(x)}{x^4 (k_B T_{\rm CMB})^3 (1+z)^2}\} P\left(\frac{\ell+1/2}{r}\right), \tag{3-18}$$

where g is the linear growth factor of the gravitational potential,Φ, and g' is its derivative with respect to the conformal time. We will fit this model to our data in §5, allowing a free normalization for each term.

Finally, we write the theoretical expectation for the projected galaxy auto-power, C_{gg}, which we use to find the galaxy bias. Combining Eqs. (3-12), (3-13), and (3-16), we arrive at

$$C_{gg}(\ell) = \frac{\int dr\ r^2\ n_c^2(r) [b_g^2 \cdot P\left(\frac{\ell+1/2}{r}\right) + \gamma \cdot n_c^{-1}(r)]}{\left[\int dr\ r^2\ n_c(r)\right]^2}, \tag{3-19}$$

where the n_c^{-1} term is the power spectrum of the Poisson noise, δ_p, while the extra free parameter, γ, is introduced to include the possible corrections to the Poisson noise due to the finite pixel size. In the absence of such corrections $\gamma = 1$. In §5, we seek the values of b_g and γ that best fit our observed auto-power for each galaxy sub-sample.

To include the effects of non-linearities in the galaxy power spectrum, we use the Peacock & Dodds fitting formula (Peacock & Dodds, 1996) for the non-linear matter power spectrum, $P(k)$.

3.2. Theoretical errors: cosmic variance vs. shot noise

To estimate the expected theoretical error, again for simplicity, we restrict the calculation to the small angle limit. In this limit, the cross-correlation function can be approximated by

$$C_{AB}(\ell) \simeq \frac{4\pi}{\Delta\Omega}\langle \tilde{A}_{\ell m}\, \tilde{B}^*_{\ell m}\rangle, \tag{3-20}$$

where $\Delta\Omega$ is the common solid angle of the patch of the sky covered by observations of both $\tilde{A}$ and $\tilde{B}$ (Tegmark, 1997).

Assuming gaussianity, the standard deviation in C_{AB}, for a single harmonic mode, is given by

$$\begin{aligned} \Delta C^2_{AB}(\ell) &= \langle C^2_{AB}(\ell)\rangle - \langle C_{AB}(\ell)\rangle^2 \\ &= \Delta\Omega^{-2}[\langle \tilde{A}_{\ell m}\, \tilde{B}^*_{\ell m}\rangle\langle \tilde{A}_{\ell m}\, \tilde{B}^*_{\ell m}\rangle + \langle \tilde{A}_{\ell m}\, \tilde{A}^*_{\ell m}\rangle\langle \tilde{B}_{\ell m}\, \tilde{B}^*_{\ell m}\rangle] \\ &= C^2_{AB}(\ell) + C_{AA}(\ell)C_{BB}(\ell). \end{aligned} \tag{3-21}$$

The number of modes available between ℓ and $\ell+1$, in the patch $\Delta\Omega$, is

$$\Delta N \simeq \frac{(2\ell+1)\Delta\Omega}{4\pi}, \tag{3-22}$$

and so the standard deviation of C_{AB}, averaged over all these modes is

$$\Delta C_{AB}^2(\ell) \simeq \frac{4\pi}{\Delta\Omega(2\ell+1)}[C_{AB}^2(\ell) + C_{AA}(\ell)C_{BB}(\ell)]. \tag{3-23}$$

In fact, since the main part of CMB fluctuations is of primordial origin, the first term in brackets is negligible for the cross-correlation error, so the error in the cross-correlation function, as one may expect, depends on the individual auto-correlations.

We can use the CMBFAST code (Seljak & Zaldarriaga, 1996) to calculate the auto-correlation of the CMB temperature fluctuations. Also, the theoretical expectation for the auto-power of the projected galaxy distribution is given by Eq.(3-19).

The galaxy/CMB auto-power spectra are dominated by Poisson (shot) noise/detector noise at large ℓ's. Therefore, the measurement of the thermal SZ signal, which becomes important at large ℓ's, is limited by the number of observed galaxies, as well as the resolution of the CMB detector (the angle at which signal-to-noise ratio for the CMB measurement is of order unity). On the other hand, for the small ℓ portion of the cross-correlation which is relevant for the ISW signal, the error is set by the matter and CMB power spectra and thus, is only limited by cosmic variance. The only way to reduce this error is by observing a larger volume of the universe in the redshift range $0 < z < 1$, where dark energy dominates.

3.3. A Note On the Covariance Matrices

We saw in §3.3 that the errors in cross-correlations could be expressed in terms of the theoretical auto-correlation. However, this is not the whole story.

We have a remarkable understanding of the auto-power spectrum of the CMB. However, if one tries to use the frequency information to subtract out the microwave sources, the simple temperature auto-power does not give the cross-frequency terms in the covariance matrix. In fact, in the absence of a good model, the only way to constrain these terms is by using the cross-correlation of the bands themselves. Of course, this method is limited by cosmic variance and hence does not give an accurate result at low multipoles. To solve this problem, we use the WMAP concordance model CMB auto-power for $\ell \leq 13$. Since there is no frequency-dependent signal at low ℓ's, we only use the W-band information, which has the lowest Galactic contamination (Bennett et al. , 2003b), for our first 4 ℓ-bins which cover $3 \leq \ell \leq 13$ (see the end of §3.4 for more on our ℓ-space binning).

There is a similar situation for the contaminants of the 2MASS galaxy catalog. Systematic errors in galaxy counts, due to stellar contamination or variable Galactic extinction, as well as observational calibration errors, may introduce additional anisotropies in the galaxy distribution which are not easy to model. Again, the easiest way to include these systematics in the error is by using the auto-correlation of the observed galaxy distribution, which is inaccurate for low multipoles, due to cosmic variance. Unfortunately, this is also where we expect to see possible Galactic contamination or observational systematics. With this in mind, we try to avoid this problem by excluding the quadrupole, $C(2)$, from our analysis.

At this point, we should point out a misconception about the nature of Monte-Carlo vs. jack-knife error estimates in some previous cross-correlation analyses, and in particular Fosalba, Gaztañaga, & Castander (2003); Fosalba & Gaztañaga (2004). Many authors have used Gaussian Monte-Carlo realizations of the CMB sky to estimate the covariance matrix of their real-space cross-correlation functions (Boughn & Crittenden, 2003; Fosalba, Gaztañaga, & Castander, 2003;

Fosalba & Gaztañaga, 2004; Scranton et al., 2003). The justification for this method is that, since the first term in Eq.(3-23) is much smaller than the second term, the error in cross-correlation for any random realization of the maps is almost the same as the true error, and the covariance of the cross-correlation, obtained from many random Gaussian realizations is an excellent estimator of the covariance matrix. We may also obtain error estimates based on random realizations of one of the maps, as long as the observed auto-power is a good approximation of the true auto-power, i.e. the cosmic variance is low, which should be the case for angles smaller than 20 degrees ($\ell > 10$). Of course, at larger angles, as we mentioned above, one is eventually limited by the systematics of the galaxy survey and, unless they are understood well enough, since theoretical error estimate is not possible, there will be no better alternative rather than Monte-Carlo error estimates. In fact, contrary to Fosalba, Gaztañaga, & Castander (2003); Fosalba & Gaztañaga (2004), if anything, the presence of cross-correlation makes Monte-Carlo errors a slight underestimate (see Eq.3-23). On the other hand, there is no rigorous justification for the validity of jack-knife covariance matrices, and the fact that jack-knife errors could be smaller than the Monte-Carlo errors by up to a factor of three (Fosalba, Gaztañaga, & Castander, 2003; Scranton et al., 2003) implies that they underestimate the error.

As we argue below (see §3.4), since we do our analyses in harmonic space and use most of the sky, our ℓ-bins are nearly independent and performing Monte-Carlo's is not necessary. Our covariance matrix is nearly diagonal in ℓ-space and its elements can be obtained analytically, using Eq.(3-23).

3.4. Angular Cross-Power Estimator

The WMAP temperature maps are set in HEALPix format (Górski, Banday, Hivon, & Wandelt, 2002), which is an equal area, iso-latitude pixellization of the sky. As a component of the HEALPix package, the FFT based subroutine 'map2alm' computes the harmonic transform of any function on the whole sky. However, as we describe in the next section, in order to avoid contamination by Galactic foreground emission in WMAP temperature maps, and contamination by stars and Galactic extinction in the 2MASS survey, we have to mask out $\sim 15\%$ of the CMB and $\sim 30\%$ of the 2MASS sky. Therefore, we cannot obtain the exact values of the multipoles, C_ℓ, and should use an estimator.

We use a quadratic estimator which is based on the assumption that our masks, $W(\hat{\mathbf{n}})$, are independent of the data that we try to extract (see Efstathiou, 2003, for a review of different estimators). The real-space cross-correlation of the masked fields $\bar{A}(\hat{\mathbf{n}}) = W_A(\hat{\mathbf{n}})\tilde{A}(\hat{\mathbf{n}})$ and $\bar{B}(\hat{\mathbf{n}}) = W_B(\hat{\mathbf{n}})\tilde{B}(\hat{\mathbf{n}})$ on the sphere is given by

$$\begin{aligned}
&\langle \bar{A}(\hat{\mathbf{n}})\bar{B}(\hat{\mathbf{m}})\rangle\langle \tilde{A}(\hat{\mathbf{n}})\tilde{B}(\hat{\mathbf{m}})W_A(\hat{\mathbf{n}})W_B(\hat{\mathbf{m}})\rangle \\
&\quad = \langle \tilde{A}(\hat{\mathbf{n}})\tilde{B}(\hat{\mathbf{m}})\rangle\langle W_A(\hat{\mathbf{n}})W_B(\hat{\mathbf{m}})\rangle,
\end{aligned} \tag{3-24}$$

where, in the last step, we used the independence of data and masks, and averaged over all pairs of the same separation. Assuming that $\langle W_A(\hat{\mathbf{n}})W_B(\hat{\mathbf{m}})\rangle$ does not vanish for any separation (which will be true if the masked out area is not very large), we can invert this equation and take the Legendre transform to obtain the un-masked multipoles

$$\begin{aligned}
C_{\tilde{A}\tilde{B}}(\ell) &= \sum_{\ell=0}^{\ell_{max}} F_{\ell\ell'} C_{\bar{A}\bar{B}}(\ell'), \text{ where} \\
F_{\ell\ell'} &= (\ell' + \frac{1}{2}) \int \frac{P_\ell(\cos\theta)P_{\ell'}(\cos\theta)}{\langle W_A W_B\rangle(\theta)}\, d\cos\theta.
\end{aligned} \tag{3-25}$$

In fact this estimator is mathematically identical [2] to the one used by the WMAP team (Hivon et al. , 2002), and, within the computational error, should give the same result. The difference is that we do the inversion in real-space, where it is diagonal, and then transform to harmonic space, while they do the inversion directly in harmonic space. Indeed, using our method, we reproduce the WMAP binned multipoles (Hinshaw et al. , 2003) within 5%. However, we believe our method is computationally more transparent and hence more reliable. Also, the matrix inversion in harmonic space is unstable for a small or irregular sky coverage (although it is not relevant for our analyses).

Finally, we comment on the correlation among different multipoles in ℓ-space. Masking about 30% of the sky causes about 30% correlation among neighboring multipoles. We bin our multipoles into 13 bins that are logarithmically spaced in ℓ (covering $3 < \ell < 1000$) , while excluding the quadrupole due to its large Galactic contamination in both data sets. The highest correlation between neighboring bins is 15% between the first and the second bins ($C(3)$ and $(9C(4) + 11C(5))/20$). To simplify our calculations, we neglect this correlation, as any correction to our results will be significantly smaller than the cosmic variance uncertainty(see §5.2), i.e. we approximate our covariance matrix as diagonal in ℓ-space.

4. Data

4.1. WMAP foreground cleaned temperature maps

We use the first year of the observed CMB sky by WMAP for our analysis (Bennett et al. , 2003a). The WMAP experiment observes the microwave sky in

---

[2] We thank Eiichiro Komatsu for pointing out this identity.

5 frequency bands ranging from 23 to 94 GHz. The detector resolution increases monotonically from 0.88 degree for the lowest frequency band to 0.22 degree for the highest frequency. Due to their low resolution and large Galactic contamination, the two bands with the lowest frequencies, K(23 GHz) and Ka(33 GHz), are mainly used for Galactic foreground subtraction and Galactic mask construction (Bennett et al. , 2003b), while the three higher frequency bands, which have the highest resolution and lowest foreground contamination, Q(41 GHz), V(61 GHz), and W(94 GHz), are used for CMB anisotropy spectrum analysis. Bennett et al. (2003b) use the Maximum Entropy Method to combine the frequency dependence of 5 WMAP bands with the known distribution of different Galactic components that trace the dominant foregrounds to obtain the foreground contamination in each band. This foreground map is then used to clean the Q, V and W bands for the angular power spectrum analysis. Similarly, we use the cleaned temperature maps of these three bands for our cross-correlation analysis. We also use the same sky mask that they use, the Kp2 mask which masks out 15% of the sky, in order to avoid any remaining Galactic foreground, as well as ~ 700 identified microwave or radio point sources.

4.2. 2MASS extended source catalog

We use galaxies from the Near-IR *Two Micron All Sky Survey* (2MASS; Skrutskie et al. , 1997) as the large-scale structure tracer of the recent universe. Our primary data set is the public full-sky extended source catalog (XSC; Jarrett et al. , 2000). The K_s-band isophotal magnitude, K_{20}, is the default flux indicator we use to select the external galaxies for our analysis. K_{20} is the measured flux inside a circular isophote with surface brightness of 20 mag arcsec^{-2}. The raw magnitudes from the catalog were corrected for Galactic extinction using the IR reddening map of Schlegel et al. (1998):

$$K_{20} \rightarrow K_{20} - A_K, \tag{3-26}$$

where $A_K = R_K E(B-V) = 0.367 \times E(B-V)$ [3]. There are approximately 1.5 million extended sources with corrected $K_{20} < 14.3$ after removing known artifacts (cc_flag != 'a' and 'z') and using only sources from a uniform detection threshold (use_src = 1).

Completeness and Contamination

We use the standard log N-log S test to determine the completeness limit of the extended source catalog. The top panel of Fig. 3.1 shows the number of galaxies as a function of K_{20}. The log number counts can be approximated by a power-law:

$$\frac{dN^{\kappa}}{dm} \propto 10^{\kappa m}. \tag{3-27}$$

To infer the true number count-magnitude relation, we need to ensure that our catalog is free from contaminants since not all extended sources from the XSC are external galaxies. At low Galactic latitude where stellar density is high, unresolved multiple star systems are often confused as extended sources. For the purpose of fitting for the power-law slope κ, we use only sources with $|b| > 30°$. Using $\sim 250,000$ galaxies in the magnitude range $13.2 < m < 13.7$ (where the reliability has been determined to be 99% by Huchra & Mader, 2001), we fitted a number count slope $\kappa = 0.676 \pm 0.005$.

While the XSC is unreliable at low Galactic latitudes, the $|b| > 30°$ cut is too restrictive and would throw away a large area of the sky that can be used

---

[3] This is different from $R_K = 0.35$ used by Kochanek et al. (2001) whose luminosity function parameters we use to estimate the redshift distribution, but the median difference of extinction derived between the two is small (< 0.002 mag).

for analysis. In principle, we could use the stellar density n_{star} from the 2MASS Point-Source Catalog (PSC) to set a threshold for excluding region of high stellar density. However, since it has been shown by Bell et al. (2003) and Ivezic et al. (2000) that unresolved extended galaxies are found in the PSC(up to 2% of all point sources with $K_{20} \sim 14$), a mask derived from the observed stellar density would preferentially exclude regions of high galaxy density.

We use the extinction map of Schlegel et al. (1998) to exclude regions of the sky where the XSC is unreliable. Fig. 3.2 shows the average number of galaxies per HEALPix pixel of $0.83\,\mathrm{deg}^2$ ($N_{side} = 64$), as a function of Galactic extinction for the four magnitude ranges used in our analysis. For bright galaxies, e.g. $K_{20} < 13.5$, the Galactic density is constant on degree scales. For the faintest magnitude bin, the number density drops off at large A_K for A_K beyond ~ 0.065. We thus choose $A_K < 0.05$ [4]. This stringent threshold excludes $\sim 99\%$ of all regions with $n_{star} > 5000\,\mathrm{deg}^{-2}$. Moreover, it improves the global reliability of galaxy counts, as our flux indicator K_{20} for each source was corrected for Galactic extinction, which has an uncertainty that scales with A_K itself. This cut reduces the number of extended sources with $K_{20} < 14.3$ to ~ 1 million, covering $\sim 68.7\%$ of the sky. For the sake of completeness, we also repeat our cross-correlation analysis for a less stringent mask with $A_K < 0.1$, which covers $\sim 79.0\%$ of the sky.

Using $\kappa = 0.676$ derived from regions with $|b| > 30°$ as a model for the true underlying number counts, we infer the catalog completeness and contamination as a function of apparent magnitude for the extinction cropped sky. We deduce the intercept of the linear log counts - magnitude model by scaling the observed number counts from the $|b| > 30$ region to the larger A_K masked sky at the bright

---

[4] This is also the level chosen by Maller et al. (2003) for their auto-correlation analysis of the XSC.

magnitude range $12.5 < K_{20} < 13.0$. Essentially, we assumed the two number count distributions are identical at those magnitudes. The observed fractional deviation from Eq. (3-27)

$$I(m) \;=\; \left(\frac{dN^{\kappa}}{dm} - \frac{dN^{\rm obs}}{dm}\right) \Big/ \frac{dN^{\kappa}}{dm} \tag{3-28}$$

is positive at faint magnitudes indicating incompleteness but crosses zero to a constant negative level towards the bright-end, which we inferred as contamination to the XSC. Plotted in the bottom panel of Fig. 3.1 is the completeness function $C(m) \equiv 1 - I(m)$, where we parametrically fitted using

$$I(m) \;=\; I_o \exp\left[-\frac{(m-\bar{m})^2}{2\sigma^2}\right] - Const. \tag{3-29}$$

In Fig. 3.1, the term *Const* describes the low level of excursion beyond $C(m) = 1$. We obtained a $\sim 98\%$ completeness for $K_{20} < 13.85$ and contamination rate at 0.5% level for $A_K < 0.05$ (solid curve). As a comparison, a less stringent threshold of $A_K < 0.2$ (dotted curve), the completeness is $\sim 95\%$ with contamination at 1.5%. The dashed curve is computed using high latitude data ($|b| > 30^\circ$), serves roughly as the completeness upper-bound (as a function of apparent magnitude) for the XSC.

At a low level, contaminants in the catalog merely increase the noise of our signal with marginal systematic bias. The $A_K < 0.05$ extinction mask is close to optimal in terms of signal-to-noise for our cross-correlation analysis. On the other hand, catalog incompleteness at faint magnitudes affects our ability to infer the correct redshift distribution. We use galaxies up to $K_{20} = 14.0$ but weighted the redshift distribution at a given magnitude range (described below) by Eq. (3-29).

Redshift Distribution

The redshift distribution of our sample was inferred from the Schechter (1976) parameters fit of the K_{20} luminosity function from Kochanek et al. (2001). The redshift distribution, dN/dz of galaxies in the magnitude range $m_{\rm bright} < m < m_{\rm faint}$ is given by the integration of the luminosity function $\phi(M)$

$$\frac{dN}{dz}(z)\,dz = \int_{M_b(z)}^{M_f(z)} \phi(M)\,dM \times \frac{dV_c}{dz}(z)\,dz, \tag{3-30}$$

where dV_c/dz is the line-of-sight comoving volume element and

$$M_f(z) \equiv m_{\rm faint} - DM(z) - k(z) \tag{3-31}$$

$$M_b(z) \equiv m_{\rm bright} - DM(z) - k(z) \tag{3-32}$$

Here, $DM(z)$ and $k(z)$ are the distance modulus and k-correction at redshift z. To be consistent with Kochanek et al. (2001), we employ $k(z) = -6.0\log(1+z)$, but the redshift distribution is insensitive to the exact form of the k-correction. The Schechter parameters used were $M^* = -23.39$ and $\alpha_s = -1.09$. For analytic convenience, we further model dN/dz with the three parameter generalized-gamma distribution:

$$\begin{aligned}\frac{dN}{dz}(z\,|\,\lambda,\beta,z_o)\,dz &\propto \frac{\beta}{\Gamma(\lambda)}\left(\frac{z}{z_o}\right)^{\beta\lambda-1} \\ &\times \exp\left[-\left(\frac{z}{z_o}\right)^{\beta}\right] d\left(\frac{z}{z_o}\right).\end{aligned} \tag{3-33}$$

The fit were weighted by relative counts, hence they are exact near z_o, the mode of the distribution, but underestimate the true number at the high redshift tail by less than 1%. Table 3.1 gives the redshift distribution parameters for the four magnitude bins used in our analysis. We normalize the integral of dN/dz with the total number of observed galaxies in the respective magnitude range,

$$N_{\rm total}(\Delta\Omega) = \int_0^\infty \frac{dN}{dz}(z)\,dz \times \Delta\Omega \tag{3-34}$$

$$\begin{aligned} &= \int_0^\infty n_c(z)\,\frac{dV_c}{dz}(z)\;dz \int d\Omega \\ &\equiv \int n_c(r)\;r^2\,dr\,d\Omega.\end{aligned} \tag{3-35}$$

The observed $N_{\rm total}$ is consistent with the 10% uncertainty in the normalization, $\phi^* = 1.16 \times 10^{-2}\, h^3\, {\rm Mpc}^{-3}$ obtained by Kochanek et al. (2001) in their luminosity function analysis. Eq. (3-35) gives the explicit relation (in the absence of clustering) between the redshift distribution, dN/dz, and the comoving density, $n_c(r)$ used in §3.1.

Fig. 3.3 is a plot of the redshift distribution for the four magnitude bins used in our analysis. For the first three bright samples, where we are complete, the parameters for dN/dz were derived from a direct application of Eq. 3-30. For $13.5 < K_{20} < 14.0$, the redshift distribution was computed by summing up magnitude slices with interval $\Delta K_{20} = 0.05$, and weighted by their relative number counts.

5. Results

For the following results, unless we mention otherwise, we use the WMAP concordance cosmological model, with a running spectral index (Spergel et al., 2003).

By comparing the angular auto-power spectrum of the galaxies in each magnitude bin with the theoretical auto-power spectrum (Eq.3-19), we can obtain the bias of the 2MASS galaxies. In order to do this, we use a χ^2 fit, assuming

Table 3.1: $\frac{dN}{dz}$ parameters for the four magnitude bins

	z_o	β	λ	N
$12.0 < K_{20} < 12.5$	0.043	1.825	1.574	49817
$12.5 < K_{20} < 13.0$	0.054	1.800	1.600	102188
$13.0 < K_{20} < 13.5$	0.067	1.765	1.636	211574
$13.5 < K_{20} < 14.0$	0.084	1.723	1.684	435232

independent gaussian random errors at each ℓ-bin. Fig. (3.4) compares our best fit models of the auto-power (solid curves) with the measured auto-powers for each magnitude bin. The value of the bias for all the magnitude bins is within

$$b_g = 1.11 \pm 0.02, \tag{3-36}$$

which confirms our constant bias assumption[5]. Our values for the Poisson correction factor (see Eq.3-19), γ, are all within 1% of 1.02. The most significant deviation of the theoretical fit from the observed auto-power is about 30% at $\ell \sim 30 - 40$. One possibility may be that galaxy bias is larger at large (linear) scales than at the (non-linear) small scales. In order to estimate the effect, we can limit analyses to the first 7 ℓ-bins ($\ell \lesssim 70$, scales larger than $\sim 7 - 13\ h^{-1}\,\mathrm{Mpc}$). This yields the estimated bias on linear scales:

$$b_{g,\mathrm{lin}} = 1.18 \pm 0.08, \tag{3-37}$$

The angular scale corresponding to $\ell = 30 - 40$ is a few degrees, which is close to the length of the 2MASS scanning stripes (6°). The amplitude of deviation from the constant bias model would require systematic fluctuations of order 10% in the number counts on that scale. If these were due to systematic errors in the 2MASS photometric zero-point, such fluctuations would require a magnitude error $\Delta m \sim 0.06$, which is significantly larger than the calibration uncertainties in 2MASS (Nikolaev et al. , 2000). Therefore, we will use our estimated linear bias (Eq. 3-37) for the interpretation of our ISW signal, while we use the full bias estimate (Eq. 3-36), which is dominated by non-linear scales, to analyze our SZ signal.

---

[5] Given that the galaxy distribution is non-linear and non-gaussian, the χ^2 fit is not the optimal bias estimator. However, the fact that the biases for different bins are so close implies that the error in bias, as we see below, is much smaller than the error in our cross-correlation signal and so is negligible.

The points in Fig. (3.5) summarize our twelve observed cross-correlation functions (3 WMAP bands × 4 magnitude bins), while Fig. (3.6) shows the same data after subtracting out the best fit contribution due to microwave point sources. We fit our theoretical model (Eq. 3-18) to our cross-correlation points (including only the W-band for the first 4 ℓ-bins; see §3.3), allowing for free global normalizations for the ISW, SZ and Point Source components. The curves show this model with the best fit normalizations for these components, while the shaded region shows the 68% uncertainty around a null hypothesis. Fig. (3.7) shows how individual theoretical components depend on frequency and ℓ for our faintest magnitude bin. As we mentioned in §3.3, different ℓ-bins are nearly independent. However, different combinations of frequency bands and magnitude bins are highly correlated and we use the full covariance matrix which we obtain from the data itself (see §3.3) for our χ^2 analysis.

The apparent dispersion in our data points for the first 4-5 ℓ-bins is smaller than what we expect from gaussian statistics (the shaded regions in Fig. 3.5 and 3.6). This may be due to the non-gaussian nature of the systematics (observational or Galactic), which dominate the error on large angles, and make the variance (Eq. 3-23) significantly different from the 68% confidence region.

Figs. (3.5) & (3.6) show that our faintest magnitude bin has the smallest error. This is due to the fact that our faintest magnitude bin covers the largest effective comoving volume and number of galaxies (see Table 3.1 and Fig. 3.3), and as a result, between 50-70% of our signal (depending on the component) comes from this bin. Repeating the statistical analysis for individual magnitude bins leads to results consistent with the combined analysis within the errors.

5.1. Thermal SZ signal

In a model described in Appendix A, we quantify the amplitude of the SZ signal in terms of Q, the coefficient of temperature-mass relation for clusters of galaxies

$$T_e(M) = (6.62 \text{ keV})Q\left(\frac{M}{10^{15}h^{-1}M_\odot}\right)^{2/3}. \tag{A2}$$

Different theoretical and observational methods place Q somewhere between 1 and 2, with observations preferring the higher end. This amplitude could be equivalently described in terms of $\tilde{T}_e$, the product of pressure bias and average electron temperature (see Eq. 3-7), which is less model dependent. Our best fit value for the thermal SZ signal, which shows a signal at the 3.1σ level, is

$$Q = 1.19 \pm 0.38, \text{ or } \tilde{T}_e = b_p\bar{T}_e = (1.04 \pm 0.33) \text{ keV}, \tag{3-38}$$

which is consistent with the X-ray observations of galaxy clusters.

This result is slightly dependent on the spectrum of the microwave point sources, which we discuss below in §5.3. If we restrict the analysis to $\ell > 20$, which is where all the SZ signal comes from, and our estimates of the covariance matrix is robust, our reduced χ^2 is 0.93 which is within the 68% allowed range for our 12 × 13 degrees of freedom. This implies that there is no observable systematic deviation from our theoretical expectation for the shape of the thermal SZ cross-power (or its gaussianity).

Repeating the analysis with the $A_K < 0.1$ extinction mask (See §4.2) for the 2MASS galaxies, which has a 10% larger sky coverage, increases the SZ signal slightly to $Q = 1.27 \pm 0.35$, which is a detection at the $\sim 3.7\sigma$ significance level. This is probably because the Galactic contamination close to the plane is only at large angles and does not contribute to the SZ signal. Therefore, as long as the Galactic contamination does not completely dominate the fluctuations, increasing the area only increases the SZ signal.

5.2. ISW signal

Using our estimated linear bias (Eq. 3-37), our χ^2 fit yields an ISW signal of

$$\mathrm{ISW} = 1.49 \pm 0.61 \qquad (3\text{-}39)$$
$$\times \ \text{concordance model prediction},$$

a 2.5σ detection of a cross-correlation. As with the previous cross-correlation analyses (Boughn & Crittenden, 2002; Fosalba, Gaztañaga, & Castander, 2003; Fosalba & Gaztañaga, 2004; Nolta et al., 2003), this is consistent with the predictions of the concordance ΛCDM paradigm. However, among the three signals that we try to constrain, the ISW signal is the most difficult to extract, because almost all the signal comes from $\ell < 20$, given our redshift distribution. For such low multipoles, there are several potential difficulties:

1- The small Galactic contamination or observational systematics in 2MASS may dominate the fluctuations in the projected galaxy density at low multipoles and wipe out the signal. However, since we use the observed auto-power of 2MASS galaxies for our error estimates, this effect, which does contribute to the auto-power (and not to the signal), is included in our error.

2- Our covariance estimator loses its accuracy as the cosmic variance becomes important at low multipoles (see §3.3). A random error in the covariance matrix can systematically increase the χ^2 and hence decrease the estimated error of our signal. However, our reduced χ^2 is 0.88, which is in fact on the low side (although within 1σ) of the expected values for 124 degrees of freedom [6] (remember that we only used

---

[6] A low χ^2 is to be expected if we overestimate the noise in the ISW signal. In particular, this could be the case if the CMB power is suppressed on large angles.

the W band for the first 4 ℓ-bins). Assuming gaussian statistics, this implies that we do not significantly underestimate our error.

3- Possible Galactic contamination in WMAP may correlate with Galactic contamination in 2MASS at low multipoles, which may lead to a fake positive signal. However, the largest contribution of Galactic foreground is visible in the Q-band (Bennett et al. , 2003b), and our low ℓ multipoles have in fact a lower amplitude in Q band. Although this probably shows a large error due to contamination in the Q-band amplitude, the fact that this is lower than the amplitude of V and W bands implies that our main signal is not contaminated. Because of the reasons mentioned in §3.3, we only use the W-band information for $\ell < 14$.

Using the less stringent extinction mask, $A_K < 0.1$ (see §4.2), for the 2MASS sources yields a signal of ISW$= 1.9 \pm 1.1$, which is a lower signal to noise detection at the 1.7σ level. This is probably due to the fact that most of the ISW signal comes from angles larger than $\sim 10°$, which is highly contaminated in regions close to the Galactic Plane.

Finally, we should mention that since the ISW signal comes from small ℓ's, while the SZ and point source signals come from large ℓ's (See Fig. 3.7), there is a small correlation (less than 10%) between the ISW and other signals.

5.3. Microwave Point Sources

As described in §2.3, we assume that our point sources trace the 2MASS objects and have either a Milky Way spectrum, a ν^{-2}, or a ν^{-3} frequency dependence their

---

This would increase the significance of an ISW detection at such scales. This effect is elaborated in Kesden, Kamionkowski, & Cooray (2003).

Table 3.2: Best fit point source strengths for different assumed spectra. The associated best fit SZ signal and χ^2 are also quoted. Here, T_A stands for the antenna temperature, while L_V^*, defined in Eq.(B2), is the estimated luminosity of the Milky Way in WMAP's V-band.

Spectrum	L_V/L_V^*	Q	χ^2
Milky Way	16.2 ± 7.8	1.10 ± 0.40	111.2
$\delta T_A \propto \nu^{-2}$	21.0 ± 8.1	1.19 ± 0.38	109.5
$\delta T_A \propto \nu^{-3}$	10.9 ± 4.7	0.94 ± 0.33	110.8

antenna temperature (the last two are the expected synchrotron spectrum of radio sources). The results are shown in Table 3.2. We see that, although all the spectra are consistent at a 2σ level, we achieve the lowest χ^2 for a ν^{-2} spectrum which is similar to the spectrum of point sources, identified by the WMAP team Bennett et al. (2003b). We should also note that since the ℓ-dependence of the SZ and Point Source signals are very similar, the two signals are correlated at a $50 - 70\%$ level, which is shown in Fig. (3.8). Using a less stringent extinction mask ($A_K < 0.1$, see §4.2) increases the detection level of microwave sources by about 10%.

To relax our assumption for the redshift distribution of Point Sources (which we assume to be the same as 2MASS sources at each magnitude bin; see §2.3), we can also allow different magnitude bins to have different L_V's and treat each as a free parameter. It turns out that this does not affect either our ISW or SZ signals, or their significance, while L_V's for each magnitude bin are consistent with the values in Table 3.2, within the errors. As the Point Source signal is dominated by Poisson noise at large ℓ's, removing the assumed clustering among the Point Sources (see §2.3), does not affect the SZ or ISW signals either.

6. Conclusions

We obtain the cross-power spectrum of the three highest frequency bands of the WMAP cosmic microwave background survey with the 2MASS Extended Source Catalog of near infrared galaxies. We detect an ISW signal at the $\sim 2.5\sigma$ level, which, assuming a flat cosmology, confirms the presence of dark energy at a level consistent with the WMAP concordance cosmology. We also find evidence for an anti-correlation at small angles (large ℓ's), which we attribute to thermal SZ effect. The amplitude is at $3.1 - 3.7\sigma$ level and is consistent with the X-ray observations of galaxy clusters. Finally, we see a signal for microwave Point Sources at the 2.6σ level.

We've seen that the completeness limit of the extended source catalog is between 13.5 and 14 in K. However, matches with SDSS show that there are many unresolved sources in the 2MASS Point Source Catalog (PSC) that are in fact galaxies. If we can select out galaxies in the PSC, perhaps by their distinctive colors, we should be able to push the sample at least half a magnitude fainter than we have done here, probing higher redshifts with a substantially larger sample.

Future wide-angle surveys of galaxies should be particularly valuable for cross-correlation with the WMAP data, especially as the latter gains signal-to-noise ratio in further data releases. The Pan-STARRS project (Kaiser et al. , 2002) for example, should yield a multi-color galaxy catalog to 25th mag or even fainter over 20,000 square degrees or more of the sky well before the end of the decade; it will more directly probe the redshift range in which the SZ and ISW kernels peak, and therefore should be particularly valuable for cross-correlating with WMAP and other CMB experiments.

A. Semi-Analytical Estimate of SZ Signal

In order to find $\tilde{T}_e$ (defined in Eq.3-7) we need an expression for the dependence of the electron pressure overdensity on the matter overdensity. As the shock-heated gas in clusters of galaxies has keV scale temperatures and constitutes about $5-10\%$ of the baryonic mass of the universe, its contribution to the average pressure of the universe is significantly higher than the photo-ionized inter-galactic medium (at temperatures of a few eV). Thus, the average electron pressure in a large region of space with average density $\bar{\rho}(1+\delta_m)$ is given by

$$\begin{aligned}\delta p_e &\simeq \frac{\bar{n}_e}{\bar{\rho}}\int dM\cdot M\cdot k_B[T_e(M;\bar{\rho})\frac{\partial n(M;\bar{\rho})}{\partial\bar{\rho}}+n(M;\bar{\rho})\frac{\partial T_e(M;\bar{\rho})}{\partial\bar{\rho}}]\bar{\rho}\delta_m\\ &= \frac{\bar{n}_e}{\bar{\rho}}\int dM\cdot M\cdot n(M;\bar{\rho})[k_BT_e(M;\bar{\rho})][b(M)+\frac{\partial\log T_e}{\partial\log\bar{\rho}}]\delta_m, \qquad \text{(A1)}\end{aligned}$$

where $n(M;\bar{\rho})$ and $T_e(M;\bar{\rho})$ are the mass function and temperature-mass relation of galaxy clusters respectively. Also, $b(M)=\frac{\partial\log n(M;\bar{\rho})}{\partial\log\bar{\rho}}$ is the bias factor for haloes of virial mass M ($=M_{200}$; mass within the sphere with the overdensity of 200 relative to the critical density). For our analysis, we use the Sheth & Tormen analytic form (Sheth & Tormen, 1999), for $n(M)$ and $b(M)$, which is optimized to fit numerical N-body simulations.

We can use theoretical works on the cluster mass-temperature relation (which assume equipartition among thermal and kinetic energies of different components in the intra-cluster medium) to find $T_e(M)$, (e.g. Afshordi & Cen, 2002)

$$\begin{aligned}\frac{k_BT_e(M)}{m_p} &\simeq (0.32Q)(2\pi GHM)^{2/3}\\ \Rightarrow T_e(M) &= (6.62\text{ keV})Q\left(\frac{M}{10^{15}h^{-1}M_\odot}\right)^{2/3},\\ \text{while}\quad & 1<Q<2 \qquad \text{(A2)}\end{aligned}$$

for massive clusters, where $H=100h\ \mathrm{km\,s^{-1}/\,Mpc}$ is the (local) Hubble constant. Although there is controversy on the value of the normalization Q (see e.g. Komatsu

& Seljak, 2001, and references there in), Afshordi & Cen (2002) argue that, as long as there are no significant ongoing astrophysical feed-back or cooling (i.e., as long the evolution is adiabatic), the dependence on H and M should be the same. Combining this with the local comoving continuity equation

$$3(H+\delta H) = -\frac{\dot{\bar{\rho}}}{\bar{\rho}} - \dot{\delta}_m, \tag{A3}$$

yields

$$\frac{\partial \log T_e}{\partial \log \bar{\rho}} = \frac{2}{3}\frac{\partial \log H}{\partial \log \bar{\rho}} = -\frac{2\dot{D}}{9DH}, \tag{A4}$$

where D is the linear growth factor.

One may think is that observations may be the most reliable way of constraining Q in Eq.(A2). However, almost all the observational signatures of the hot gas in the intra-cluster medium come from the X-ray observations which systematically choose the regions with high gas density. With this in mind, we should mention that while observations prefer a value of Q close to 1.7, numerical simulations and analytic estimates prefer values closer to 1.2 (Afshordi & Cen, 2002). For our analysis, we treat Q as a free parameter which we constrain using our cross-correlation data (see §5.1).

Putting all the pieces together, we end up with the following expression for $\tilde{T}_e$

$$\begin{gathered}\tilde{T}_e = (0.32\ Q)(2\pi G H)^{2/3} \\ \times \int d\nu f_{ST}[\nu] M^{2/3}[b_{ST}(\nu) - \tfrac{2\dot{D}}{9DH}], \\ \nu(M) = \tfrac{\delta_c}{\sigma(M)} \qquad , \end{gathered} \tag{A5}$$

where $\sigma(M)$ is the variance of linear mass overdensity within a sphere that contains mass M of unperturbed density, while $\delta_c \simeq 1.68$ is the spherical top-hot linear growth threshold (Gunn & Gott, 1972). f_{ST} and b_{ST} are defined in Sheth & Tormen (1999). For the WMAP concordance cosmological model (Bennett et al. , 2003a), this integral can be evaluated to give

$$\tilde{T}_e = b_p \bar{T}_e = (0.88\ Q)\ \mathrm{keV}. \tag{A6}$$

The above simple treatment of the SZ signal fails at scales comparable to the minimum distance between clusters, where the average gas pressure does not follow the average matter density (Refreiger et al. , 2000; Zhang & Pen, 2001), which leads to a scale-dependent pressure bias. Moreover, efficient galaxy formation removes the hot gas from the intra-cluster medium, which causes Eq.A1 to overestimate the SZ signal. As this paper mainly focuses on the observational aspects of our detection, we delay addressing these issues into a further publication (Komatsu et al. , 2003). The preliminary results seem to be consistent with the above simple treatment at the 20% level.

B. Microwave Luminosities of the Andromeda Galaxy and the Milky Way

First we derive how much the flux received by a microwave source, with luminosity per unit frequency od L_ν, at distance d_L, and observed solid angle $\delta\Omega$ affects the observed CMB temperature. The apparent change in the black-body temperature is obtained by

$$\delta\Omega\ \cdot \delta\left[\frac{4\pi(\hbar/c^2)\nu^3}{\exp[h\nu/(k_B T_{\mathrm{CMB}})]-1}\right] = \frac{L_\nu}{4\pi d_L^2}. \tag{B1}$$

The left hand side of Eq. (B1) is the change in the Planck intensity per unit frequency, where ν and $\Delta\nu$ are the detector frequency and band width respectively. The right hand side is the observed Microwave flux per unit frequency. Defining x as the frequency in units of $k_B T_{\mathrm{CMB}}/h$, Eq. (B1) yields

$$\frac{\delta T}{T} = \frac{2\pi\hbar^2 c^2}{(k_B T_{\mathrm{CMB}})^3} \cdot \frac{\sinh^2(x/2)}{x^4} \cdot \frac{L_\nu}{\delta\Omega d_L^2}. \tag{B2}$$

To obtain the microwave luminosity of Milky Way, we assume an optically and geometrically thin disk, with a microwave emissivity, ϵ (defined as luminosity per unit frequency per unit volume), which is constant across its thickness and falls as $\epsilon_0 \exp(-r/r_0)$ with the distance, r, from its center. The disk thickness is $2H \ll r$, while we assume $r_0 \simeq 5\,\mathrm{kpc}$, our distance from the Galactic center is $r \simeq 8.5\,\mathrm{kpc}$, and our vertical distance from the center of the disk is z. Integrating Eq. (B2) over the disk thickness leads to the cosecant law for the Galactic emission

$$\frac{\delta T}{T}(b;r) = \frac{2\pi\hbar^2 c^2}{(k_B T_{\mathrm{CMB}})^3} \cdot \frac{\sinh^2(x/2)}{x^4} \cdot \epsilon_0 e^{-r/r_0}(H|\csc b| - z\csc b), \tag{B3}$$

where b is Galactic latitude. Integrating $\epsilon(r)$ over the disk volume gives the total luminosity of the Milky Way

$$L_\nu = 2H \int 2\pi r dr\ \epsilon_0 e^{-r/r_0} = 4\pi H r_0^2 \epsilon_0. \tag{B4}$$

Combining Eqs. (B3) and (B4), we can obtain the total luminosity of Milky Way from the observed Galactic emission

$$L_\nu = r_0^2 e^{r/r_0} \cdot \frac{(k_B T_{\mathrm{CMB}})^3}{\hbar^2 c^2} \cdot \frac{x^4}{\sinh^2(x/2)} \cdot |\sin b| \left[\frac{\delta T}{T}(b;r) + \frac{\delta T}{T}(-b;r)\right]. \tag{B5}$$

Figure 7 in Bennett et al. (2003b) gives the cosecant law for the Galactic emission in different WMAP bands. Using this information in Eq.(B5) (after conversion into thermodynamic units) gives the luminosity of the Milky Way in WMAP bands

$$\begin{aligned} L_Q^* &= 2.0 \times 10^{27}\ \mathrm{erg\,s^{-1}\,Hz^{-1}}, \\ L_V^* &= 2.1 \times 10^{27}\ \mathrm{erg\,s^{-1}\,Hz^{-1}}, \\ \text{and } L_W^* &= 4.9 \times 10^{27}\ \mathrm{erg\,s^{-1}\,Hz^{-1}}. \end{aligned} \tag{B6}$$

To confirm these values, we can use Eq.(B2) and the observed integrated flux of the Andromeda (M31) galaxy in the WMAP maps to obtain its microwave luminosity

$$\begin{aligned} L_{M31,Q} &= 2.5 \times 10^{27}\ \mathrm{erg\,s^{-1}\,Hz^{-1}}, \\ L_{M31,V} &= 3.8 \times 10^{27}\ \mathrm{erg\,s^{-1}\,Hz^{-1}}, \\ \text{and } L_{M31,W} &= 7.8 \times 10^{27}\ \mathrm{erg\,s^{-1}\,Hz^{-1}}. \end{aligned} \tag{B7}$$

We see that these values are larger, but within 50%, of the Milky Way microwave luminosities.

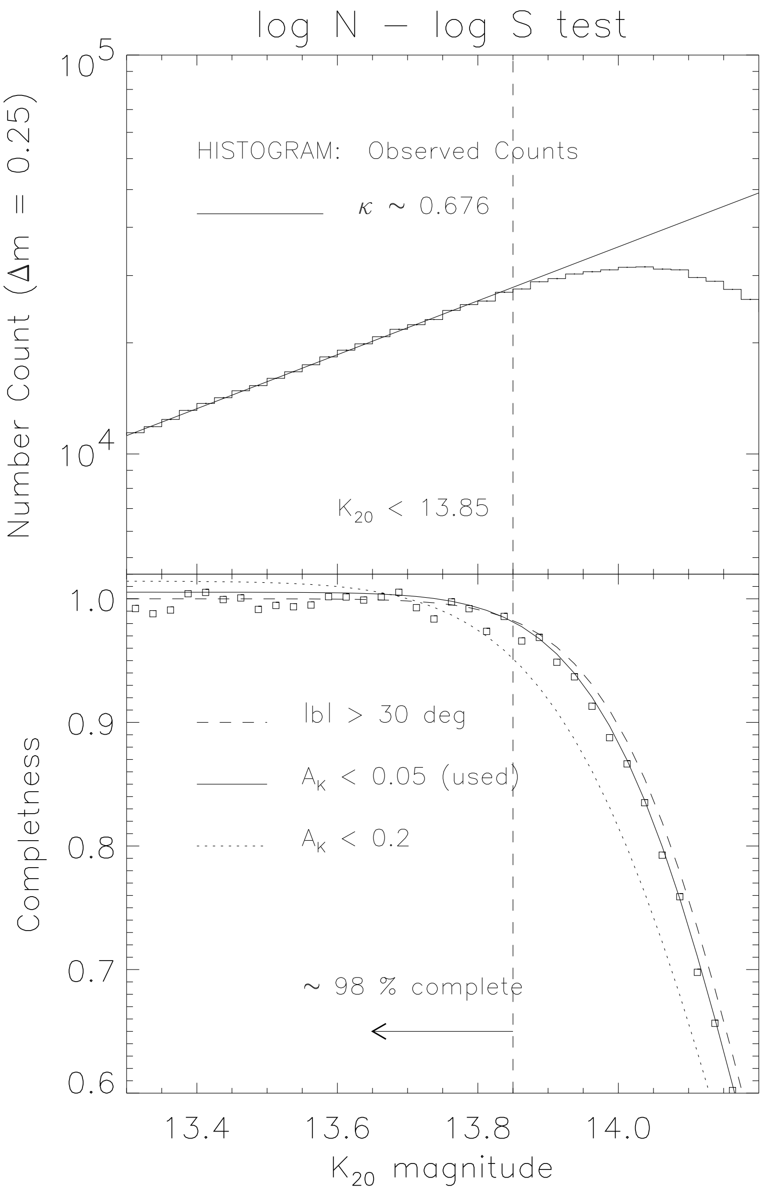

Fig. 3.1.— (Top panel) The histogram is the observed K_{20} number-magnitude relation for galaxies in regions with $A_K < 0.05$. The solid line is the model counts inferred using data from $|b| > 30°$ in the magnitude range $13.2 < K_{20} < 13.7$ where the extended source catalog(XSC) is most reliable. (Bottom panel) The square points gives the completeness as inferred from the difference between the observed and model counts. The *solid* curve is a fit to a parametric model that estimates both the incompleteness and contamination rate in a consistent manner. The *dotted* curve is a similar fit using data with a less stringent $A_K < 0.2$. The *dashed* curve is from $|b| > 30°$, which serves roughly as the completeness upper-bound for the XSC. The vertical line at $K_{20} = 13.85$ gives a completeness at 98% for data with $A_K < 0.05$ used in our analysis.

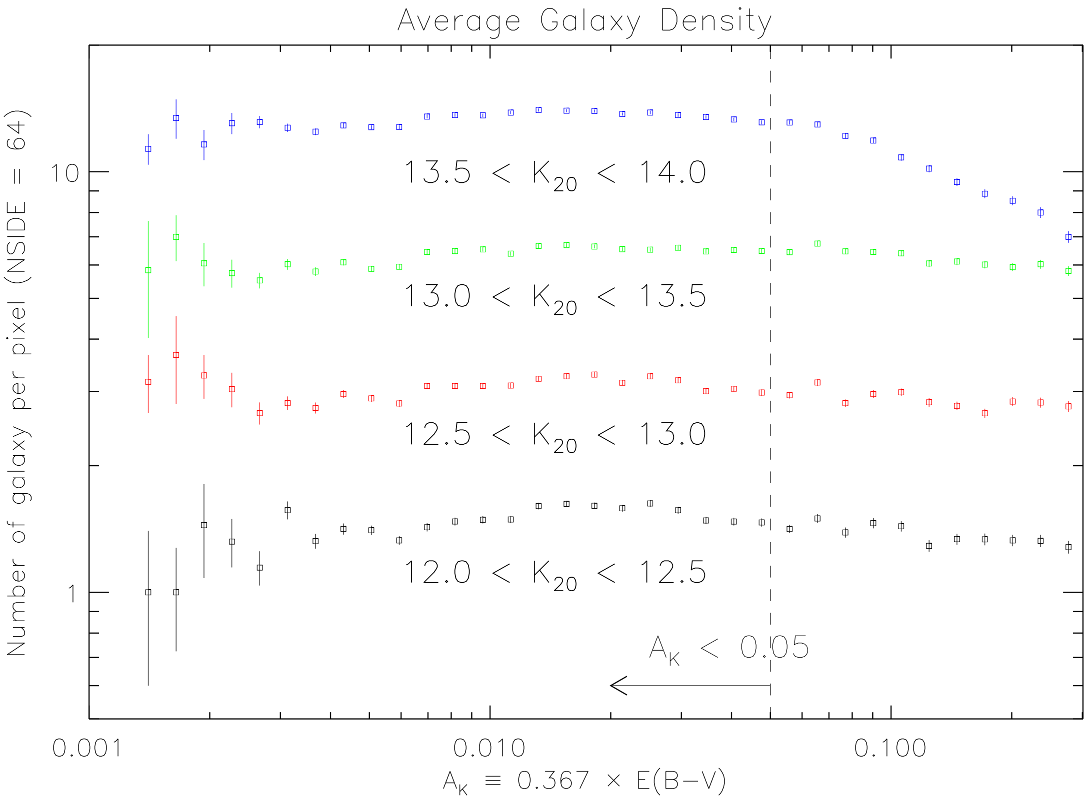

Fig. 3.2.— Average number of galaxies per 0.83 deg^2 pixel (HEALpix $N_{side} = 64$) as a function of extinction. For bright galaxies ($K_{20} < 13.5$), the galaxy density is constant up to extinction value ~ 0.25. For $13.5 < K_{20} < 14.0$, the density drops off at $A_K \sim 0.65$. We use only regions with $A_K < 0.05$ (*dashed vertical line*) for our analysis. Errors are estimated using jack-knife resampling.

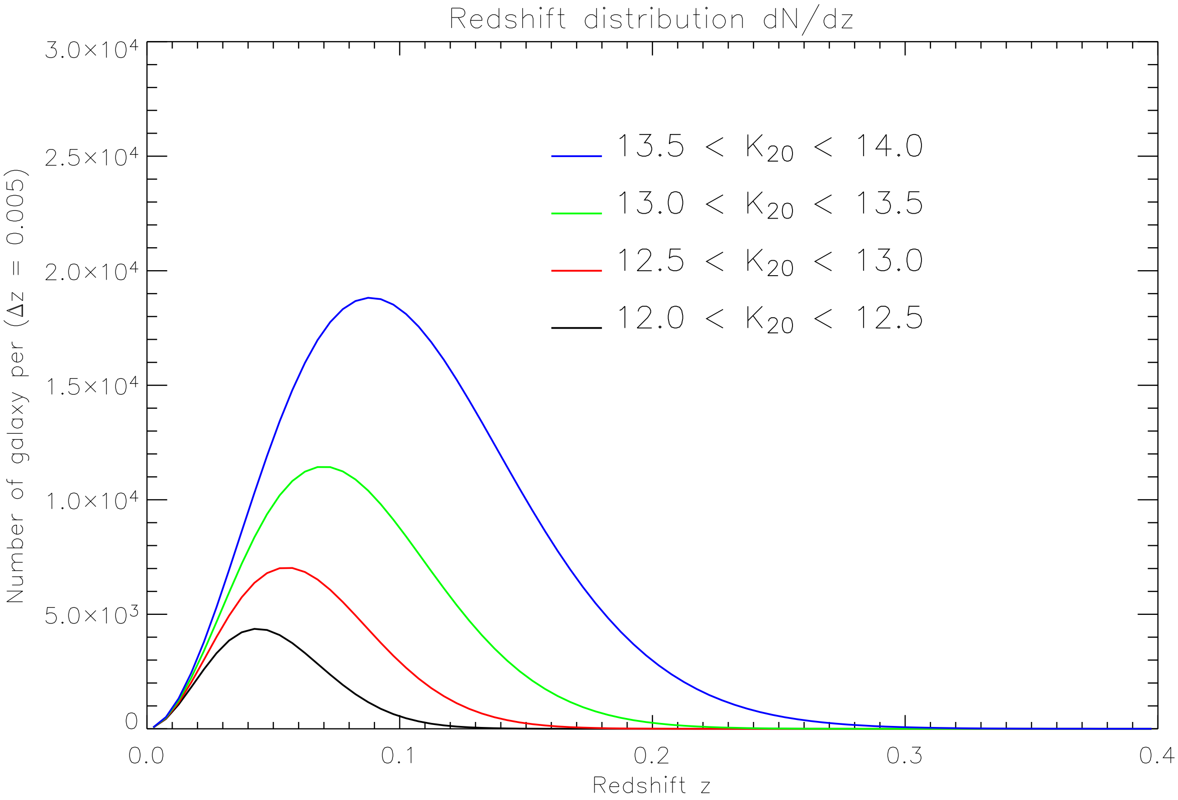

Fig. 3.3.— dN/dz for the four magnitude bins used in the analysis.

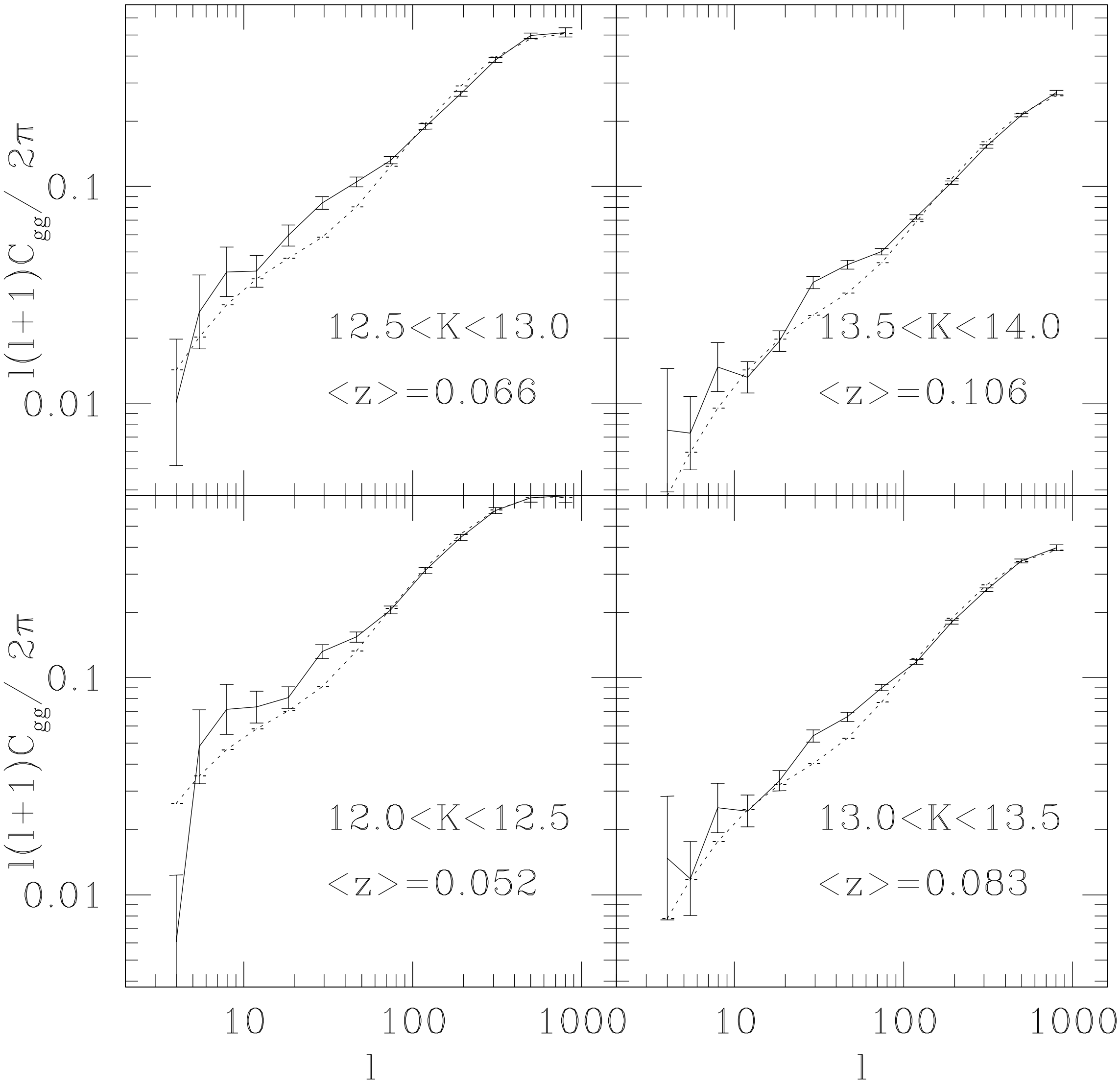

Fig. 3.4.— The auto-power for our four different magnitude bins. The solid curves show the observed auto-power multipoles with their estimated Gaussian errors (Eq. 3-23), while the dashed curves are the projected Peacock and Dodds (Peacock & Dodds, 1996) non-linear power spectra with the best fit constant bias. The best fit Poisson noise term is subtracted out.

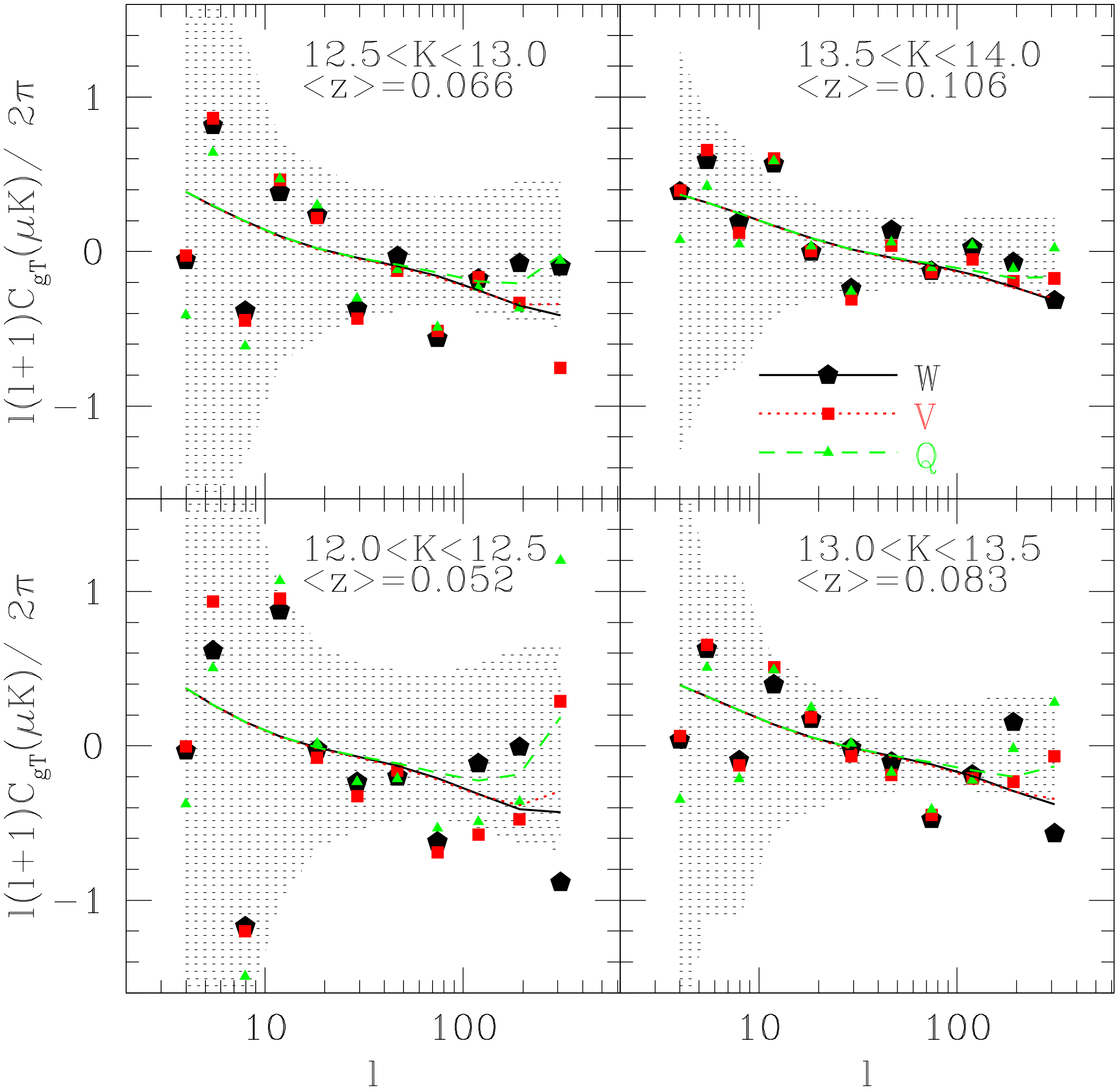

Fig. 3.5.— The cross-power for our four magnitude bins. The curves are the best fit model (ISW+SZ+Point Sources) for the three bands and the points show the data. The ISW/SZ components dominate the signal for ℓ's below/above 20. The Point Source contribution becomes important for the lower frequency bands at the highest ℓ's. The shaded region shows the $1-\sigma$ error centered at the null hypothesis. Note that, while different ℓ-bins are nearly independent, different cross-powers of bands with magnitude bins are highly correlated. As shot noise dominates the signal for our last two ℓ-bins, for clarity, we only show the first 11 ℓ-bins, for which the errors for the three WMAP bands are almost the same.

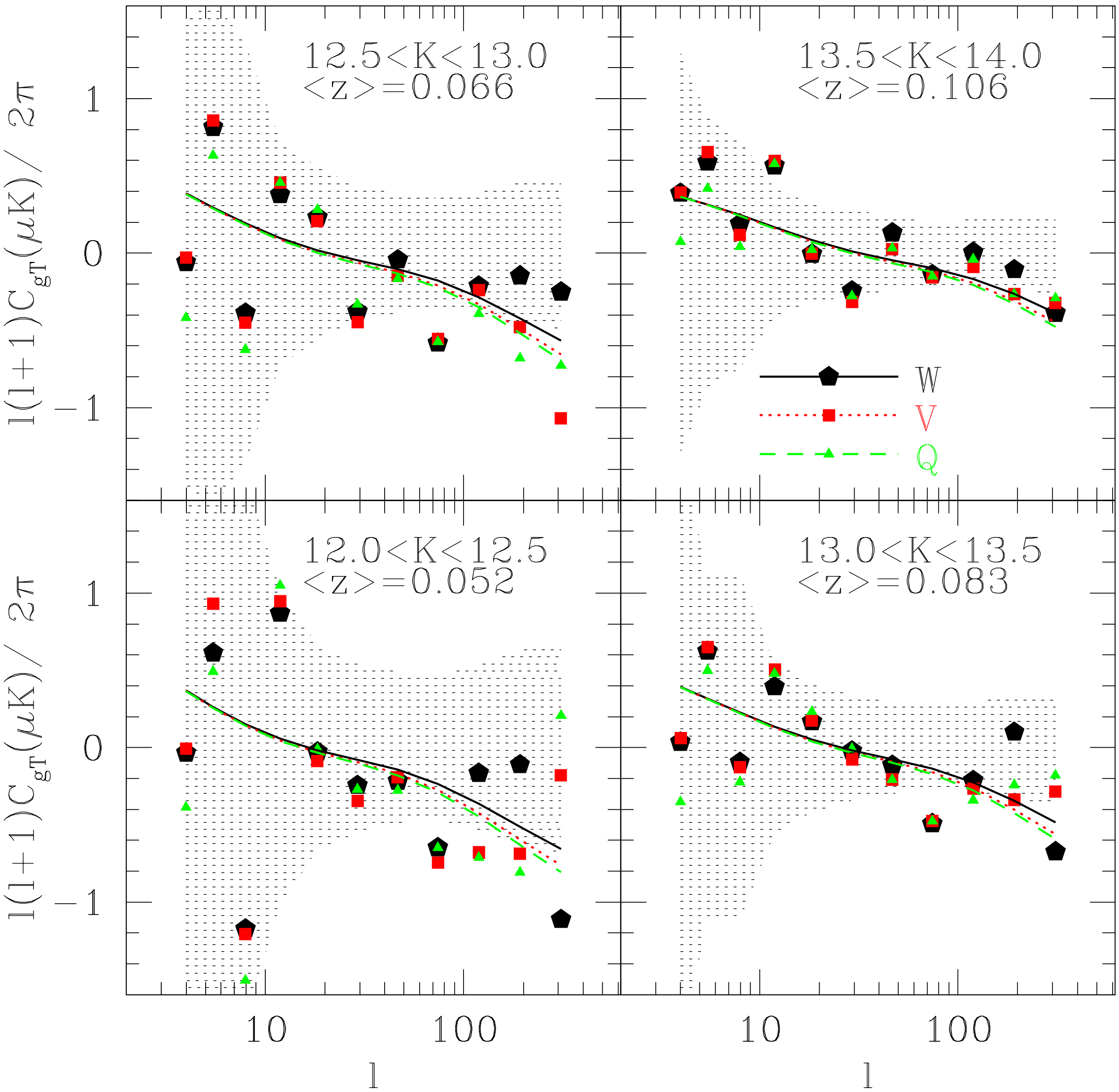

Fig. 3.6.— The same as Fig. (3.5), but with the Point Source contributions subtracted from both theory and data.

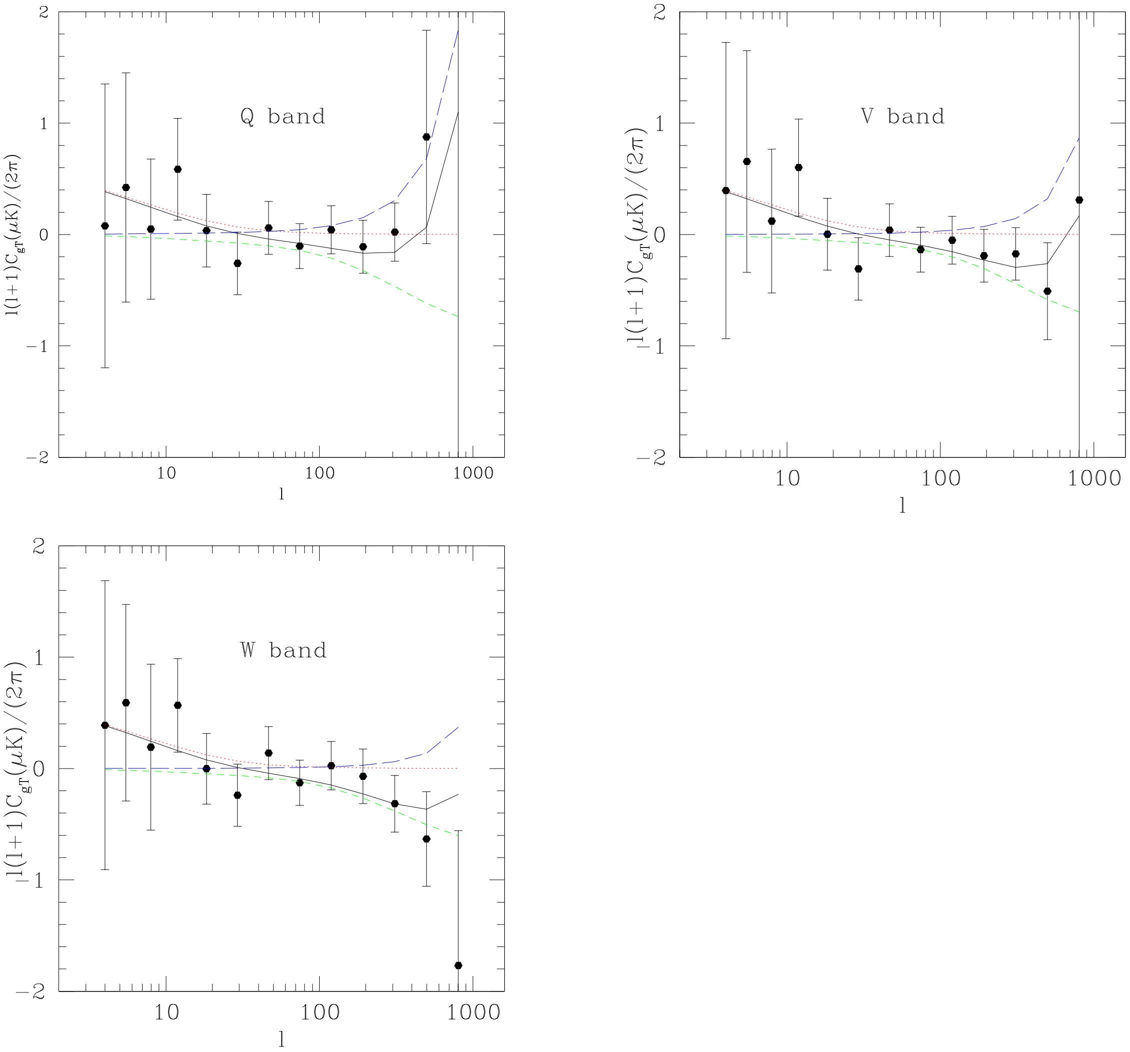

Fig. 3.7.— Different components of our best fit theoretical cross-power model, compared with the data for our faintest magnitude bin ($13.5 < K < 14$). The dotted(red) curves show the ISW component, while the short-dashed(green) and long-dashed(blue) curves are the SZ and Point Source components respectively. The black curves show the sum of the theoretical components, while the points are the observed cross-power data.

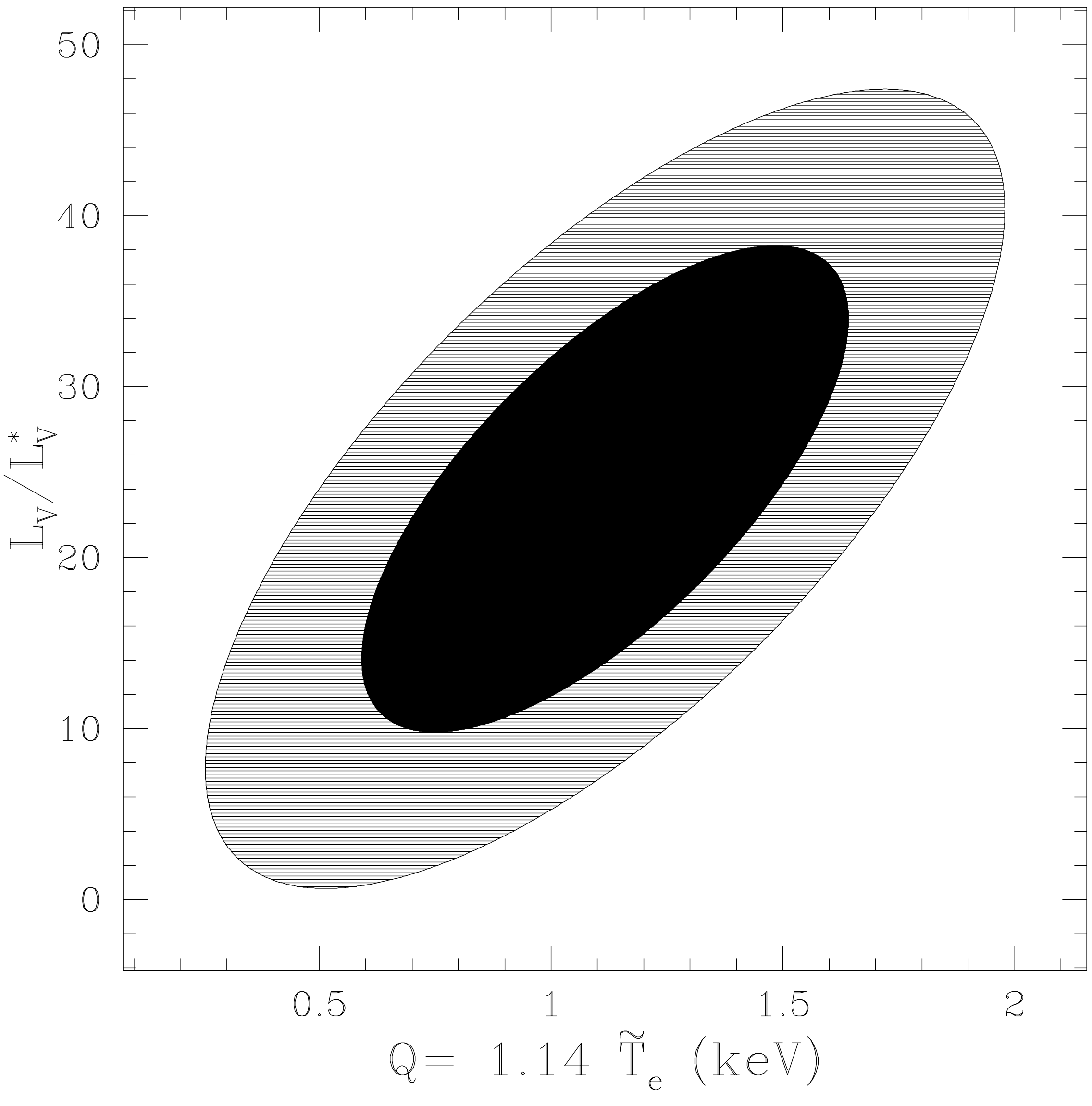

Fig. 3.8.— 1 and $2-\sigma$ likelihood regions of our SZ+Point Source signals, for a $\delta T_A \propto \nu^{-2}$ spectrum (see Table 3.2). Q (defined in Eq.A2) is the coefficient of the mass-temperature relation for galaxy clusters, while $\tilde{T}_e$ (defined in Eq. 3-7), is the product of gas pressure bias and the average electron temperature. L_V is the average WMAP V-band luminosity of the 2MASS sources, while L_V^* (defined in Eq.B6) is the same number, estimated for the Milky Way. The large correlation of Q (SZ signal) and L_V (Point Source signal) is due to the similar ℓ-dependence of the two signals (see Fig. 3.7). Note that the conversion between $\tilde{T}_e$ and Q depends on the assumed cosmological model (see Appendix A).

Bibliography

Abell, G.O., Corwin, H., Olowin, R., 1989, ApJS, 70, 1

Afshordi, N., & Cen, R. 2002, ApJ, 564, 669

Bell, E.F., et al. 2003, ApJS, 149, 289

Bennett, C. et al. 1996, ApJ, 464, L1

Bennett, C.L. *et al.* 2003, ApJS, 148, 1 (Bennett et al. 2003a); The public data and other WMAP papers are available at http://lambda.gsfc.nasa.gov/product/map

Bennett, C.L. *et al.* 2003, ApJS, 148, 97 (Bennett et al. 2003b)

Boughn, S. P. 2003, Private Communication.

Boughn, S. P. & Crittenden, R. G., Phys. Rev. Lett. 88, 021302 (2002)

Boughn, S. P. & Crittenden, R. G. 2003, astro-ph/0305001

Condon, J. et al. 1998, Astron. J. 115, 1693

Cooray, A. 2002, Phys. Rev. D, 65, 103510

Corasaniti, P.S. *et al.* 2003, PRL, 90, 091303

Crittenden, R.G., & Turok, N. 1996, PRL, 76, 575

Diego. J.M., Silk J., & Sliwa 2003, MNRAS, 346, 940

Efstathiou, G. 2003, astro-ph/0307515

Fosalba P., & Gaztañaga E. 2003, astro-ph/0305468

Fosalba P., Gaztañaga E., & Castander, F.J. 2003, ApJ, 597L, 89

Górski, K. M., Hivon, E., & Wandelt, B. D. 1998, in *Evolution of Large-Scale Structure: From Recombination to Garching*

Gunn, J., Gott, J. 1972, ApJ, 176, 1

Hernandez-Monteagudo, C., & Rubino-Martin, J.A. 2003, astro-ph/0305606

Hivon, E., Gorski, K. M., Netterfield, C. B., Crill, B. P., Prunet, S., & Hansen, F. 2002, ApJ, 567, 2

Hinshaw, G., et al. 2003, ApJS, 148, 135

Hu, W. & Dodelson, S. 2002, ARA&A, 40, 171

Huchra, J & Mader, J (2000) at http://cfa-www.harvard.edu/∼huchra/2mass/verify.htm

Ivezić, Ž. et al. in *IAU Colloquium 184: AGN Surveys, 18-22 June 2001, Byurakan(Armenia)*

Jarrett, T.H., et al. 2000, AJ, 119, 2498

Kaiser, N., et al. 2002, SPIE, 4836, 154

Kesden, K., Kamionkowski, M., & Cooray, A. 2003, astro-ph/0306597

Kochanek, C.S., et al. 2001, ApJ 560, 566

Kogut, C.L. *et al.* 2003a, ApJS, 148, 161

Komatsu, E., Afshordi, N., & Seljak, U. 2003, in preparation

Komatsu, E., & Seljak, U. 2001, MNRAS, 327, 1353

Limber, D.N. 1954, ApJ , 119, 655

Maddox, S. J., et al. 1990, MNRAS, 242, 43

Maller, A. H., et al. 2003, astro-ph/0304005

Myers, A.D., Shanks, T. Outram, P.J., Wolfendale, A.W. 2003, astro-ph/0306180

Nikolaev, S., et al. 2000, AJ, 120, 3340

Nolta, M.R., et al. 2003, astro-ph/030597

Peacock, J.A., & Dodds, S.J. 1996, MNRAS, 280L, 19

Peebles, P. J. E., & Ratra, B. 2003, Rev.Mod.Phys. 75, 599

Peiris, H., & Spergel, D.N. 2000, ApJ, 540, 605

Refregier A., Komatsu E., Spergel D. N., Pen U., 2000, Phys. Rev. D, 61,123001

Sachs, R. K. & Wolfe, A. M. 1967, ApJ, 147, 73

Schechter, P. 1976, ApJ 203, 296.

Schlegel, D.J., Finkbeiner, D.P. & Davis, M. 1998, ApJ 500, 525.

Scranton, R. et al. 2003, astro-ph/0305337

Seljak, U. & Zaldarriaga, M. 1996, ApJ, 469, 437

Sheth, R. K. & Tormen, G. 1999, MNRAS, 308, 119

Spergel, D.N. *et al.* 2003, ApJS, 148, 175

Skrutskie et al. 1997, in *The Impact of Large Scale Near-IR Sky Survey*, ed. F. Garzon et al. (Dordrecht: Kluwer), 187

Sunyaev, R. A. & Zel'dovich, Y. B. 1972, Comments on Astrophysics and Space Physics, 4, 173

Tegmark, M. 1997, Phys. Rev. D, 56, 4514

York, D.G. *et al.* 2000, AJ, 120, 1579

Zhang, P., & Pen, U. 2001, ApJ, 549, 18

Chapter 4

Dark Energy and the Integrated Sachs-Wolfe effect

Abstract

The Integrated Sachs-Wolfe (ISW) effect is a direct signature of the presence of dark energy in the universe, in the absence of spatial curvature. A powerful method for observing the ISW effect is through cross-correlation of the Cosmic Microwave Background (CMB) with a tracer of the matter in the low redshift universe. In this paper, we describe the dependence of the obtained cross-correlation signal on the geometry and other properties of a survey of the low redshift universe. We show that an all-sky survey with about 10 million galaxies, almost uniformly distributed within $0 < z < 1$ should yield a near optimal ISW detection, at $\sim 5\sigma$ level. In order to achieve this level of signal-to-noise, the systematic anisotropies in the survey must be below $\sim 0.1\%$, on the scale of ~ 10 degrees on the sky, while the systematic error in redshift estimates must be less than 0.05.

Then, we argue that, while an ISW detection will not be a good way of constraining the conventional properties of dark energy, it could be a valuable means of testing alternative theories of gravity on large physical scales.

1. Introduction

One of the fundamental pieces of our understanding of modern cosmology comes from the study of anisotropies in the Cosmic Microwave Background (CMB). First discovered by the DMR experiment on the COBE satellite in the early 90's (Smoot et al., 1992), the observations of CMB anisotropies matured through various ground-based/balloon-borne experiments (see Bennett et al., 2003a, for a list) until its latest climax by the first year data release of the observations of the WMAP satellite (Bennett et al., 2003a) in 2003, a cosmic variance limited map of the CMB sky with a resolution of $\lesssim 0.5$ degs.

While most of the fluctuations seen by WMAP and other CMB experiments were generated at $z \sim 1000$, low redshift ($z < 20$) physics generates additional fluctuations (e.g., Hu & Dodelson, 2002). These secondary anisotropies can be detected through cross-correlating CMB measurements with large scale structure observations (Crittenden & Turok, 1996; Peiris & Spergel, 2000; Cooray, 1999). Following the WMAP data release, various groups (Boughn & Crittenden, 2004; Nolta et al., 2004; Scranton et al., 2003; Fosalba, Gaztañaga, & Castander, 2003; Fosalba & Gaztañaga, 2004) claimed a possible observation of such correlation with various galaxy surveys, although at a small ($2-3\sigma$) significance level. Most recently, (Afshordi, Loh, & Strauss, 2004) claimed a correlation between WMAP maps and the 2MASS galaxy catalog, at both large and small angles.

In this paper, we focus on such correlations on angles larger than a few degrees, and their only known cosmological source, the Integrated Sachs-Wolfe (ISW) effect (Sachs & Wolfe, 1967). The purpose of this work is to provide comprehensive overview of various observational aspects and systematic limitations of an ISW detection in cross-correlation, in a flat universe. §2 and §3 will briefly review the physics of the expected signal and error in any ISW detection. In §4, we consider over what redshift range, and what angular scales, most of the ISW signal arises, and what the optimum signal-to-noise for an ISW detection may be. §5 deals with the limitations of realistic surveys, i.e. the Poisson noise, systematic contaminations, and redshift errors. Finally, in §6, we discuss what we may (or may not) learn from a detection of the ISW signal in cross-correlation, and §7 concludes the paper.

Throughout this paper, unless mentioned otherwise, we use the flat WMAP+CBI+ACBAR+2dF+Ly-α concordance cosmological model (Spergel et al., 2003), with a cosmological constant (i.e., $w = -1$), and a running spectral index. However, note that our conclusions are not sensitive to the details of the model.

2. The ISW effect in Cross-Correlation

The ISW effect is caused by the time variation in the cosmic gravitational potential, Φ, as CMB photons pass through it. In a flat universe, the anisotropy in CMB photon temperature due to the ISW effect (Sachs & Wolfe, 1967) is an integral over the conformal time η

$$\delta_{\rm ISW}(\hat{\mathbf{n}}) = \frac{\delta T_{\rm ISW}}{T} = 2\int_{\eta_{\rm LS}}^{\eta_0} \Phi'[(\eta_0-\eta)\hat{\mathbf{n}},\eta]\; d\eta, \tag{4-1}$$

where $\Phi' \equiv \partial\Phi/\partial\eta$, and $\hat{\mathbf{n}}$ is the unit vector along the line of sight. $\eta_{\rm LS}$ and η_0 are the conformal times at the last scattering and today. The linear metric is assumed to be

$$ds^2 = a^2(\eta)\{[1+2\Phi(\mathbf{x},\eta)]d\eta^2 - [1-2\Phi(\mathbf{x},\eta)]\mathbf{dx}\cdot\mathbf{dx}\}, \tag{4-2}$$

(the so-called longitudinal gauge) and η_0 is the conformal time at the present.

In a flat universe, in the linear regime, Φ does not change with time at any given comoving point for a fixed equation of state, and therefore observation of an ISW effect is an indicator of a change in the equation of state of the universe. Assuming that this change is due to an extra component in the matter content of the universe, the so-called dark energy, this component should have a negative pressure to become important at late times (Peebles & Ratra, 2003). Therefore, observation of an ISW effect in a flat universe is a signature of dark energy.

The ISW effect is observed at large angular scales because most of the power in the fluctuations of Φ is at large scales. Additionally, the fluctuations at small angles tend to cancel out due to the integration over the line of sight.

We are interested in finding the cross-correlation of the ISW effect with the galaxy distribution. Assuming Gaussian initial conditions, and full-sky coverage, different harmonic multipoles are statistically independent in the linear regime. Therefore, as the ISW effect is only important on large scales which are still linear, the statistical analysis is significantly simplified in harmonic space. For a galaxy survey with the average comoving density distribution $n_c(r)$ as a function of the comoving distance r, the Limber equation can be used to approximately describe the expected cross-correlation with the galaxy distribution [1] (see Afshordi, Loh, & Strauss, 2004, for a detailed derivation)

$$\begin{aligned} C_{gT}(\ell) &\equiv \langle \delta^{\rm 2D}_{g,\ell m} T^{*}_{\ell m} \rangle \\ &= \frac{2\,T}{\int dr\ r^2 n_c(r)} \int dr\ n_c(r) P_{\Phi',g}\left(\frac{\ell+1/2}{r}\right), \end{aligned} \tag{4-3}$$

where $\delta^{\rm 2D}_{g,\ell m}$ and $T_{\ell m}$ are the projected survey galaxy overdensity and the CMB temperature in the spherical harmonic space. If we assume that the galaxies follow the matter density with constant bias, b_g, (i.e,. $\delta_g = b_g \delta_m$), then $P_{\Phi',g}(k) \equiv \ {\rm Re}\langle \Phi'(k)\delta^{*}_{g}(k)\rangle$, the 3D cross-power spectrum of Φ' and galaxy overdensity for the comoving wave-number k, can be related directly to $P_{\Phi',m}$. We

---

[1] The error in the Limber approximation, in the form expressed here, is about 10% at $\ell = 2$ and drops as ℓ^{-2}.

then use the G_{00} Einstein equation (e.g. Mukhanov, Feldman, & Brandenberger, 1992)

$$(k^2 + 3\mathcal{H}^2)\Phi + 3\mathcal{H}\Phi' + 4\pi G a^2(\rho_m\delta_m + \rho_{DE}\delta_{DE}) = 0, \tag{4-4}$$

to relate the matter auto-power spectrum $P_{m,m}(k) = P(k) =< |\delta_m^2(k)| >$ to $P_{\Phi',g}$. Here, $\mathcal{H} = d\ln a/d\eta$ is the conformal Hubble constant, and ρ_{DE} and δ_{DE} are the average density and overdensity of the dark energy, respectively.

Note that, for a cosmological constant (a ΛCDM cosmology), $\delta_{DE} = 0$, and Eq. (4-4) reduces to the Poisson equation for $k \gg \mathcal{H}$. In this case, Eq. (4-3) reduces to

$$\begin{aligned} C_{gT}(\ell) = -\frac{3b_g H_0^2 \Omega_m}{\int dr\ r^2 n_c(r)} \times \\ \int dr\ r^2\ n_c(r) \cdot \frac{1+z}{(\ell+1/2)^2} \cdot \frac{g'}{g} P\left(\frac{\ell+1/2}{r}\right), \end{aligned} \tag{4-5}$$

where g is the linear growth factor of the gravitational potential,Φ, and g' is its derivative with respect to the conformal time.

For any alternative theory of dark energy, an independent equation for the evolution of δ_{DE} should be solved simultaneously.

3. The Error in ISW Detection

It is easy to see that the expected dispersion (see Afshordi, Loh, & Strauss, 2004, for details) [2] in the cross-correlation signal for harmonic multipole $C_{gT}(\ell)$ is given by

$$\Delta C_{gT}^2(\ell) \simeq \frac{C_{gg}(\ell)C_{TT}(\ell)}{f_{\rm sky}(2\ell+1)}, \tag{4-6}$$

---

[2] If the survey does not cover the whole sky, the nearby multipoles in the harmonic space will not be independent. However, if we bin a large number of multipoles together, we can use the increased standard deviation of Eq. (4-6) for each multipole and treat them as independent to estimate the error of each multipole bin.

where $f_{\rm sky}$ is the fraction of sky covered in the survey, and we assumed a small cross-correlation signal, i.e. $C^2_{gT}(\ell) \ll C_{gg}(\ell)C_{TT}(\ell)$, which is the case for the ISW effect (the expected ISW effect is much smaller than the primary anisotropies, but see Kesden, Kamionkowski, & Cooray, 2003).

$C_{TT}(\ell)$ is the observed CMB temperature auto-power, which includes both the intrinsic CMB fluctuations and the detector noise. As will become clear later on, since the ISW effect is observed at small ℓ, the WMAP observed auto-power spectrum (Hinshaw et al., 2003), which has negligible detector noise at low ℓ, should give the optimum power spectrum to use in Eq. (4-6). We again use the Limber approximation to obtain the projected galaxy auto-power

$$C_{gg}(\ell) \simeq \frac{\int dr\ r^2\ n_c^2(r)[b_g^2(r)\cdot P\left(\frac{\ell+1/2}{r}\right) + n_c^{-1}(r)]}{\left[\int dr\ r^2\ n_c(r)\right]^2}. \tag{4-7}$$

Fig. (4.1) shows an example of the expected cross-power signal and error for a survey with 10 million galaxies with $b_g = 1$, uniformly distributed between $0 < z < 1$.

4. The Perfect Galaxy Survey

To obtain the optimum signal-to-noise ratio for an ISW detection in cross-correlation, we assume that we have an (at least approximate) redshift estimate for each galaxy in the survey. Then we can divide the survey into almost independent shells of thickness δr, where

$$r_0 \ll \delta r \ll r,$$

where $r_0 \lesssim 5h^{-1}\,$Mpc is the galaxy auto-correlation length. Using Eq. (4-3), the expected ISW cross-power signal for a narrow redshift bin $(z, z+\delta z)$, at multipole ℓ, is

$$C_{gT}(\ell, z) = \frac{2b_g(r)}{r^2(z)} P_{\Phi',m}\left(\frac{\ell+1/2}{r}\right), \tag{4-8}$$

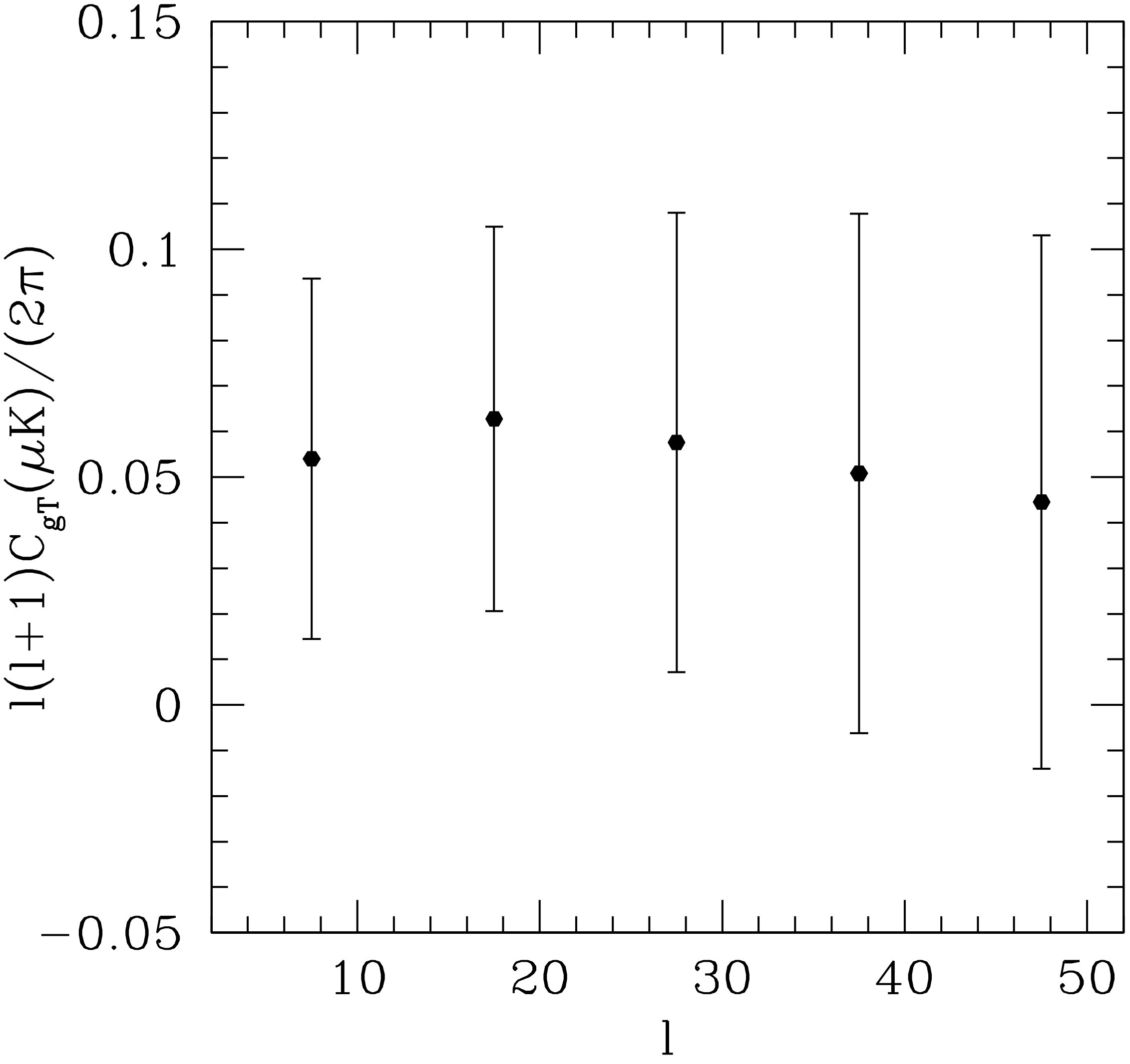

Fig. 4.1.— The expected cross-power spectrum of the ISW effect, for an all-sky survey with $b_g^2 dN/dz = 10^7$, and $z_{\rm max} = 1$

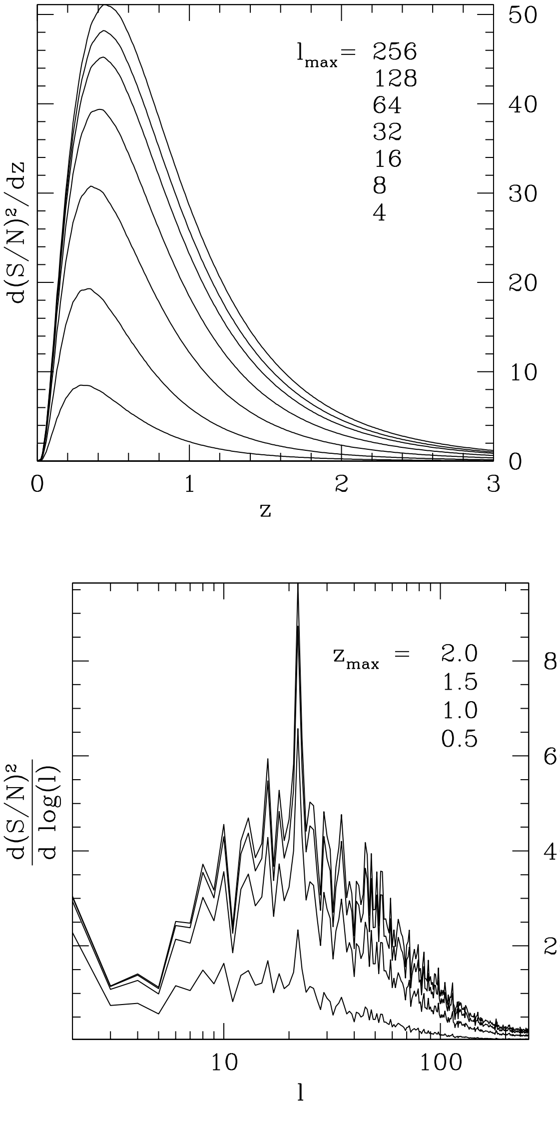

Fig. 4.2.— Figures show the expected $(S/N)^2$ distribution for a redshift or resolution limited full-sky ISW cross-correlation signal ($\ell_{\rm max}$ refers to the scale at which the (white) detector noise is equal to the true signal). In both figures, the enclosed area for the region covered by a survey, multiplied by its sky coverage, gives the optimum $(S/N)^2$ for the cross-correlation signal. The spikiness of the distribution in ℓ-space is due to the use of the actual observed WMAP power spectrum in Eq. (4-11). Note that for partial sky coverage, the low-ℓ multipoles that are not covered by the survey should also be excluded from the area under the curves.

while Eq.(4-6) gives the error in the cross-power spectrum

$$\Delta C^2_{gT}(\ell, z) = \frac{C_{TT}(\ell) C_{gg}(\ell, z)}{2\ell + 1}, \tag{4-9}$$

and Eq.(4-7) can be used to find $C_{gg}(\ell, z)$

$$C_{gg}(\ell, z) = \frac{b_g^2(r)}{r^2 \delta r} \left[P\left(\frac{\ell + 1/2}{r}\right) + (n_c b_g^2)^{-1} \right]. \tag{4-10}$$

Dividing Eq. (4-8) by Eq. (4-9), we find the expected signal-to-noise ratio for the cross-correlation signal in multipole ℓ, due to this shell

$$\delta(S/N)^2 = \frac{C^2_{gT}(\ell)}{\Delta C^2_{gT}(\ell)} = \frac{[r^{-2}\delta r \cdot (2\ell + 1)] \times 4P^2_{\Phi',m}(k)}{C_{TT}(\ell)[P(k) + (n_c b_g^2)^{-1}]}, \tag{4-11}$$

where $k = \frac{\ell+1/2}{r}$. Within the approximation of independent shells and multipoles, $(S/N)^2$ is cumulative, and we could simply add (or integrate over) the contribution due to different multipoles and shells that are included in the galaxy survey, and multiply it by the sky coverage, $f_{\rm sky}$, to obtain the optimum $(S/N)^2$ (in the absence of systematics) for the whole survey. Fig. (4.2) shows the $(S/N)^2$ density distribution for hypothetical all-sky surveys with limited (CMB) resolution, or redshift depth, in a ΛCDM cosmology, while we assumed that the Poisson noise is negligible ($n_c \to \infty$).

We see that the ISW cross-correlation signal is widely distributed over a redshift range between 0 and 1.5 (which is the era in which dark energy becomes cosmologically important), and peaks at $z \simeq 0.4$, below which the detection is limited by the available volume. Almost all the signal is due to multipoles with $\ell \lesssim 100$ ($\theta \gtrsim 2^\circ$), which implies that the WMAP 1st year all-sky temperature map (Bennett et al., 2003a), with $S/N \gg 1$ on scales larger than a degree ($\ell < 200$), captures almost all the ISW signal in the CMB sky, while the upcoming 2nd year WMAP data, or higher resolution CMB observations are unlikely to make a significant difference. The angular scale of the cross-correlation signal decreases with the depth of the survey. This is due to the fact that the angular correlation length of the galaxy distribution is smaller for a deeper (more distant) sample.

For our assumed ΛCDM cosmological model, the total S/N which could be achieved by a perfect survey is ~ 7.5. Let us compare this result with previous such estimates. The first estimate of S/N for a perfect survey (Crittenden & Turok, 1996) is, in fact, completely consistent with 7.5σ. Other such estimates (Peiris & Spergel, 2000; Cooray, 1999) focus on specific surveys, but seem to be roughly consistent with the values expected from Fig. (4.2) for those surveys. This is despite our use of Limber (Eq. 4-3) and independent redshift bins (Eq. 4-16) approximations, and demonstrates that these approximations are adequate for our purpose. Our approach allows us to visualize where in redshift-angular space one should look for the ISW signal. However, given a sample of galaxies in existence, we should emphasize that neither we, nor previous works, provide an optimum procedure to estimate this signal. For a realistic galaxy survey, such procedure would depend on possible survey contaminations or systematics, detailed geometry, and redshift information available for the survey (See the next section).

5. Sub-Optimal Galaxy Surveys

In this section we look into how different features of realistic surveys may reduce the optimum ISW signal-to-noise obtained in the last section.

5.1. Poisson Limited Surveys

For a realistic survey, an additional source of noise is Poisson fluctuations in the galaxy number density. The Poisson noise (the second term in the brackets in Eq.

4-7) is inversely proportional to the average number density of observed galaxies in the survey, which dominates the uncertainty in cross-correlation for a small galaxy sample.

Figs. (4.3-4.4) show how the total cross-correlation $(S/N)^2$ and its distribution depend on the number of galaxies in an all-sky survey. Although a fixed number of galaxies per unit redshift is assumed, different curves in Fig. (4.3) can be combined to obtain the signal-to-noise for an arbitrary redshift/bias distribution.

Fig. (4.4) shows that an ambitious all-sky survey with about 10 million galaxies (or one million clusters with $b_g \sim 3$), which uniformly cover the redshift range between 0 to 1, can only yield a S/N of $\simeq 5$. Although the Sloan Digital Sky Survey (SDSS; York et al., 2000) is unlikely to get a S/N better than 4σ due to its incomplete redshift and sky coverage, future galaxy surveys like LSST[3] and Pan-STARRS[4] could achieve a cosmic variance limited detection of ISW in cross-correlation, should they cover almost all of sky, and have sufficiently small systematic errors (see §5.2).

5.2. Observational Contamination

Another feature of a realistic galaxy survey is the presence of artificial structure in the sky maps. Such structures may be due to observational systematics, such as day to day changes of weather, seeing or photometric calibrations. Another possibility is the effective change of magnitude limit due to Galactic extinction, or Galactic contamination due to stars misidentified as galaxies. Depending on if

---

[3] http://www.lsst.org

[4] http://pan-starrs.ifa.hawaii.edu

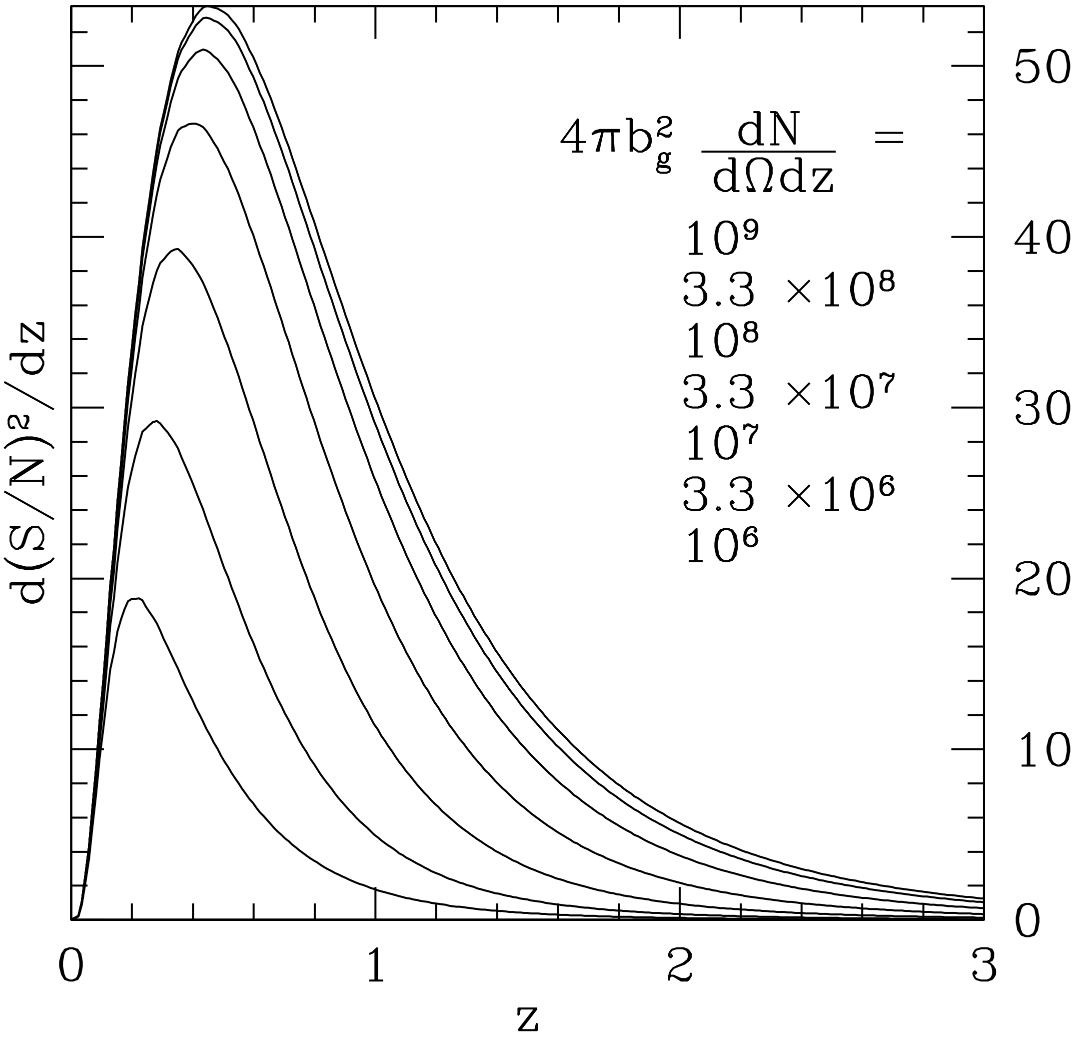

Fig. 4.3.— The distribution of $(S/N)^2$ for different galaxy redshift distributions. For partial sky coverage, the result should be multiplied by $f_{\rm sky}$.

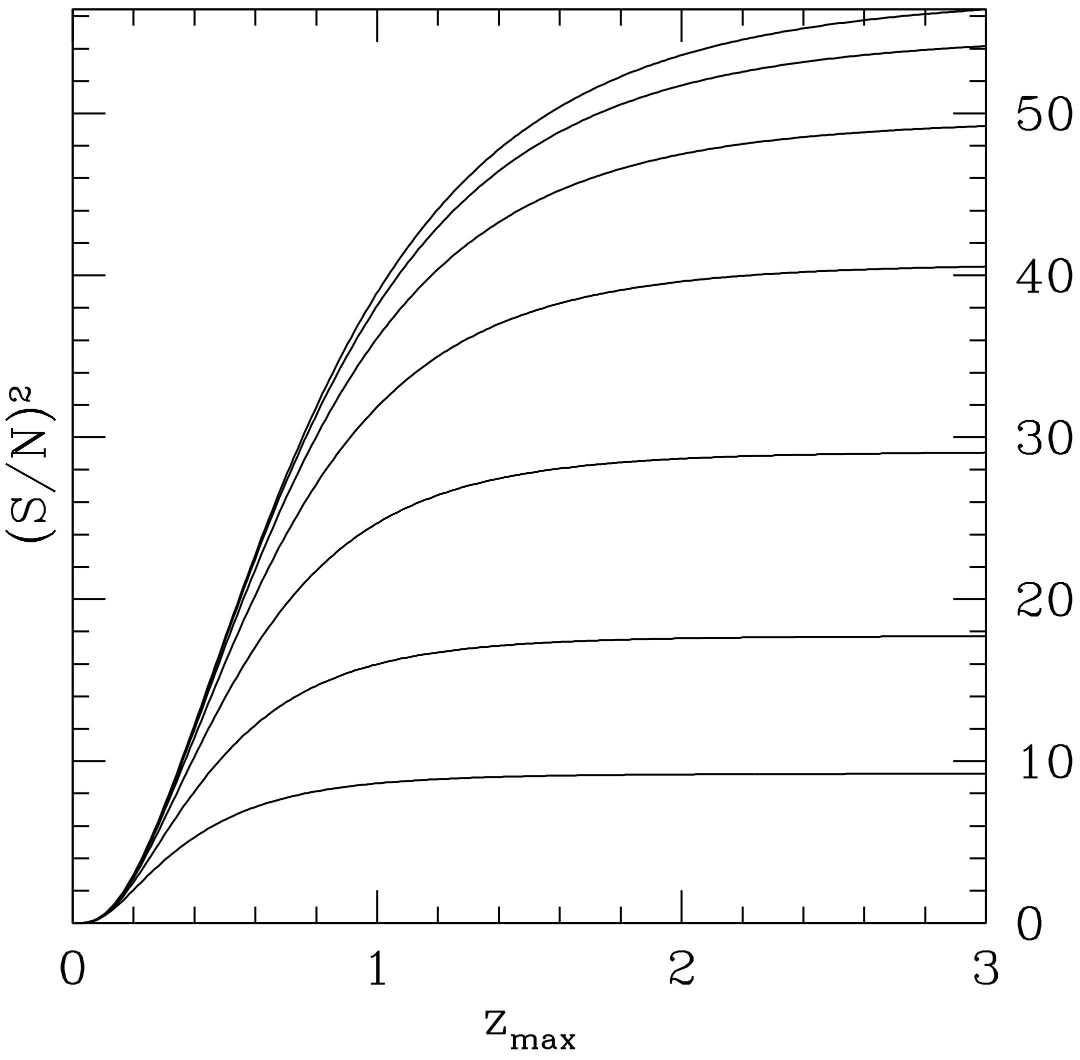

Fig. 4.4.— The total $(S/N)^2$ for a cnstant dN/dz up to $z_{\rm max}$, corresponding to the area under the curves in Fig. 4.3. In particular, for $z_{max} = 1$, and $b_g^2 dN/dz = 10^7$, the we expect $S/N \simeq 5$.

these contaminations are correlated with possible contaminations of the CMB maps, they can add extra random or systematic errors to the optimum error that may be achieved by a survey.

Uncorrelated Contaminations: Random Errors

If the contaminations of the galaxy survey is not correlated with the contaminations in the CMB map, they should not affect the expectation value of the cross-correlation function of the galaxy survey with the CMB. We do not expect the observational systematics of the galaxy/CMB surveys to be correlated. Therefore, the only effect will be to increase the random error through increasing the auto-powers of each survey (Eq. 4-6). Since the Galactic/systematic contributions to the power spectrum of the CMB are believed to be small and under control (Hinshaw et al., 2003; Bennett et al., 2003b), we focus on the contamination of the galaxy survey.

We again divide our galaxy sample into independent redshift bins. The harmonic components of the anisotropies in each redshift bin can be divided into real and systematic parts:

$$\tilde{\delta}_g(\ell, m; z) = \delta_g(\ell, m; z) + \delta_g^{sys}(\ell, m). \tag{4-12}$$

While the systematic contaminations, $\delta_g^{sys}(\ell, m)$, is also, in general, a function of redshift, for simplicity, we ignore this dependence. Of course, in practice, the level of systematics in the redshift range that contains the bulk of the ISW signal is the relevant quantity (see Figs. 4.2-4.3). Now, the contaminated auto-power spectrum will be

$$\tilde{C}_{gg}(\ell; z_1, z_2) = C_{gg}(\ell; z_1)\delta_{z_1,z_2} + C_{gg}^{sys}(\ell), \tag{4-13}$$

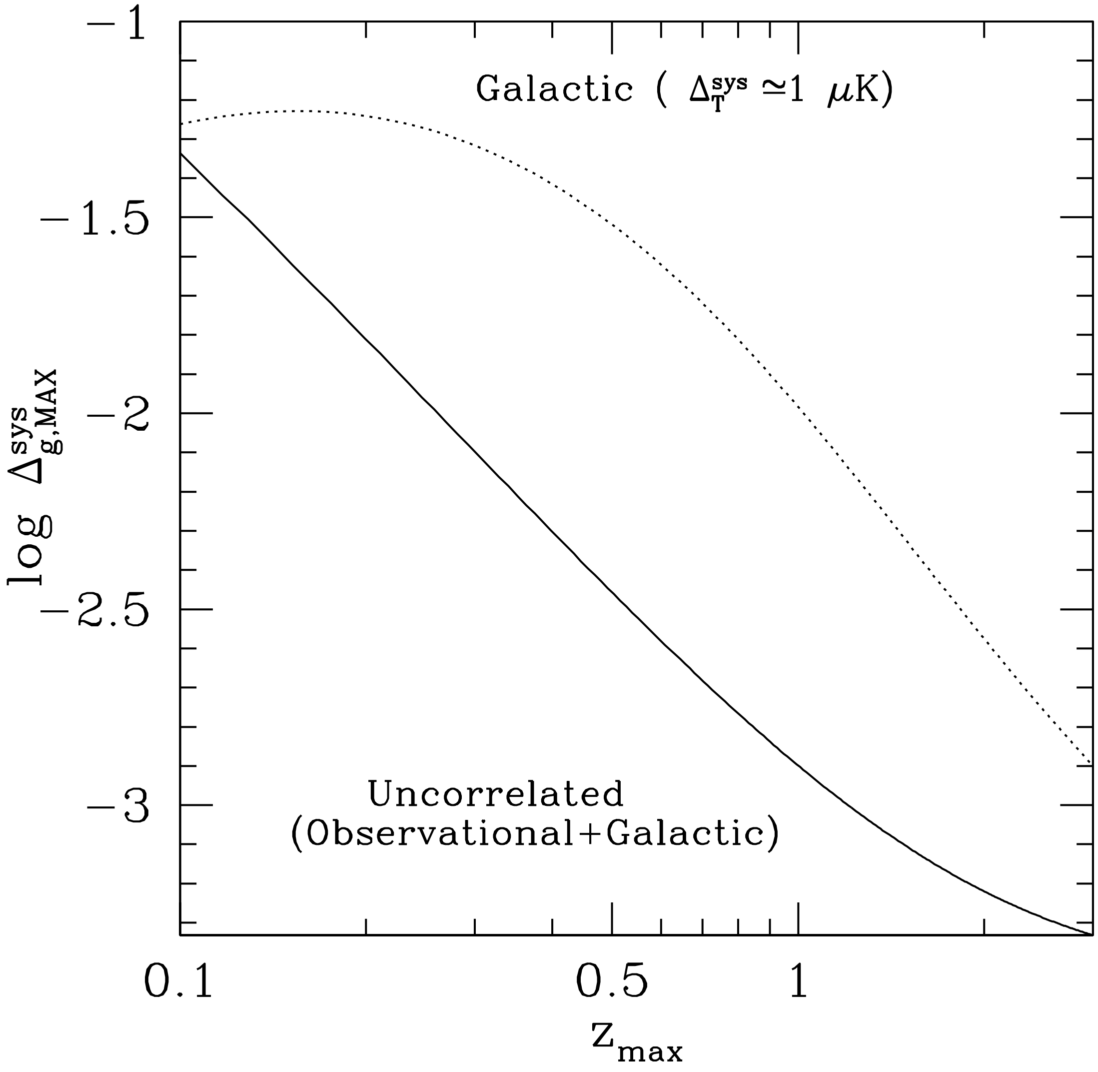

Fig. 4.5.— The graph shows the maximum allowed amplitude of anisotropies, Δ_g^{sys} introduced by possible systematics of the galaxy survey. The solid line shows the level of systematics that reduces the $(S/N)^2$ for an ISW detection by 50%. The dotted line shows the level of *correlated* contamination that introduces a systematic error in an ISW detection comparable to the cosmic variance. Here, we assume that the correlated amplitude of CMB contamination is $\sim 1\mu K$, consistent with the expected leftover Galactic contamination in WMAP foreground-cleaned W-band map (Bennett et al., 2003b).

where $C_{gg}(\ell, z)$ was defined in Eq. (4-10), and we ignore the cross-term, as we do not expect any correlation between the survey systematics and the intrinsic fluctuations in the galaxy density. Note that, unlike the previous sections, different redshift bins are now correlated, and we will need to invert the full covariance matrix to estimate the expected signal to noise. Eq. (4-6) can be generalized to get the covariance matrix of the cross-power spectrum for $f_{sky} = 1$

$$\begin{aligned}\tilde{\mathbf{C}}_{\ell;z_1,z_2} &= \langle \Delta C_{gT}(\ell, z_1) \Delta C_{gT}(\ell, z_2) \rangle \\ &= \frac{\tilde{C}_{gg}(\ell; z_1, z_2) C_{TT}(\ell)}{2\ell + 1}.\end{aligned} \tag{4-14}$$

For a low level of systematics, we can use a Taylor expansion to invert the covariance matrix

$$\tilde{\mathbf{C}}^{-1} \simeq \mathbf{C}^{-1} - \mathbf{C}^{-1} \mathbf{C}^{sys} \mathbf{C}^{-1}. \tag{4-15}$$

Now combining Eqs. (4-8,4-9, and 4-13-4-15) yields an approximate expression for the suppression of $(S/N)^2$ due to the presence of contaminations:

$$\begin{aligned}\delta(S/N)^2 &\simeq - \sum_{z_1, z_2, \ell} (2\ell + 1) \frac{C^{sys}_{gg}(\ell) C_{gT}(\ell, z_1) C_{gT}(\ell, z_2)}{C_{TT}(\ell) C_{gg}(\ell, z_1) C_{gg}(\ell, z_2)} \\ &= - \sum_{\ell} (2\ell + 1) \frac{C^{sys}_{gg}(\ell)}{C_{TT}(\ell)} \left(\sum_z \frac{C_{gT}(\ell, z)}{C_{gg}(\ell, z)} \right)^2.\end{aligned} \tag{4-16}$$

Let us define the amplitude of the systematic contaminations, Δ^{sys}_g as

$$\Delta^{sys}_g \equiv \sqrt{\frac{\ell(\ell + 1) C^{sys}_{gg}(\ell)}{2\pi}}. \tag{4-17}$$

Again, for simplicity, we assume that Δ^{sys}_g is independent of ℓ. Of course, the relevant amplitude for Δ^{sys}_g corresponds to the ℓ-range that contains the bulk of the ISW signal, i.e. $\ell \sim 20$ (see Fig. 4.2). The solid line in Fig. (4.5) shows the amplitude of uncorrelated contamination, required to reduce the $(S/N)^2$ by 50%. Thus, we see that since we need $z_{max} \gtrsim 1$ to capture most of the ISW signal (see §4), the level of systematic anisotropy in the galaxy survey should be less than 0.1% on scales of $\ell \sim 20$.

As an example, let us assume the systematic anisotropy in an optical survey is due to uncertainties in the magnitude calibration. Furthermore, let us assume that we know the (approximate) redshifts, and in a given redshift bin, the luminosity function is given by the Schechter function (Schechter, 1976):

$$\phi(L)\ dL = \phi^* \cdot (L/L^*)^\alpha \exp(-L/L^*)(dL/L^*) \tag{4-18}$$

where ϕ^*, L^*, and α are characteristic galaxy number density, luminosity, and slope of the luminosity function, respectively. Assuming that the survey is almost complete in the given redshift bin, i.e. $L_{min} \ll L^*$, the systematic anisotropy is given by:

$$\Delta_g^{sys} = \frac{\phi(L)\Delta L_{min}}{\int \phi(L)dL} = (L_{min}/L^*)^{1+\alpha} \frac{\Delta L_{min}/L_{min}}{\Gamma(1+\alpha)}. \tag{4-19}$$

For $\alpha \simeq -0.9$ (Blanton et al., 2003), we can ignore $1+\alpha$ in the exponent, and use $\Delta L/L = 0.4 \ln(10)\Delta m$, to arrive at

$$\Delta_g^{sys} \simeq \frac{0.4\ \ln 10\ \Delta m}{\Gamma(1+\alpha)} \simeq 0.1\ \Delta m < 10^{-3}, \tag{4-20}$$

where Δm is the uncertainty in the magnitude calibration. Thus, we see that Δm needs to be $\lesssim 0.01$, for the error to be dominated by cosmic variance. The accuracy of this calibration is currently ~ 0.02 for SDSS (Abazajian et al., 2003), and will remain a challenge for future surveys such as Pan-STARRS and LSST. Note that the magnitude uncertainty of individual galaxies, as long as they are not correlated on the scale of a few degrees on the sky, can be significantly larger.

Repeating this estimate for an incomplete survey. i.e. $L_{min} > L^*$, we see that a significantly higher precision of magnitude measurement will be required to capture the ISW signal:

$$\Delta m \lesssim \begin{cases} 0.01 & \text{for } L_{min} \ll L^*, \\ 10^{-3} \frac{L^*}{L_{min}} & \text{for } L_{min} \gg L^*. \end{cases} \tag{4-21}$$

Galactic Contaminations: Systematic Errors

As the Galactic sources of contamination in the CMB and galaxy surveys are correlated, they may cause a systematic over/underestimate of the cross-correlation signal. In order to model this effect, we assume that this correlated signal follows the Schlegel, Finkbeiner, and Davis (SFD) Galactic extinction map (**?**). Since the bulk of the ISW signal comes from $\ell \sim 20$, we normalize the amplitude of the contaminating signals at $\ell = 20$. The level of Galactic contamination in the foreground cleaned W-band of the WMAP satellite (Bennett et al., 2003b) is expected to be $\sim 1\ \mu K$ outside the Galactic plane, and thus we take

$$\Delta_T^{sys}(\ell) \equiv \sqrt{\frac{\ell(\ell+1)C_{gg}^{sys}(\ell)}{2\pi}} = 1\ \mu K, \quad \text{for } \ell = 20, \tag{4-22}$$

while we assume $C_{gg}^{sys} \propto C_{TT}^{sys} \propto C_{\rm SFD}$, for the ℓ-dependence of the correlated contamination. Here, $C_{\rm SFD}$ is the angular auto-power spectrum of the SFD extinction map.

The dotted line in Fig. (4.5) shows the amplitude of the correlated systematic anisotropy, normalized at $\ell = 20$, which yields a systematic error in the ISW signal equal to the cosmic variance error. Since this systematic error is proportional to $\Delta_T^{sys} \times \Delta_g^{sys}$, the upper bound, $\Delta_{g,\rm MAX}^{sys}$, shown in this figure decreases for larger Galactic contaminations in the CMB, inversely proportional to Δ_T^{sys}. Thus, we see that since the solid curve is below the dotted curve, as long as $\Delta_T^{sys} <$ few μK, the level of uncorrelated contamination puts a more stringent constraint on the systematics of the galaxy survey. As we discussed in §5.2, this requires the systematic anisotropy of the survey to be less than 0.1 %.

5.3. Redshift errors

Since the ISW kernel has such a broad distribution in redshift space, redshift errors are not expected to be a big limiting factor for ISW cross-correlation measurements.

We can simulate *random* errors in the estimated redshifts, via re-writing Eq. (4-16) for finite redshift bins of thickness $2\Delta z$. It turns out that even using bins as thick as $\Delta z \sim 0.5$ will not decrease the signal-to-noise by more than 5%.

Systematic errors in redshifts, or in redshift distribution, may also systematically bias the estimates of ISW amplitude. Taking the unbiased ISW amplitude to be one, the ISW amplitude, biased by the systematic redshift error Δz is given by

$$\begin{aligned} 1 + \frac{\delta \mathrm{ISW}}{\mathrm{ISW}} = & \sum_{\ell,z} \frac{C_{gT}(\ell, z+\Delta z)/C_{gT}(\ell,z)}{\Delta C^2_{gT}(\ell,z)/C^2_{gT}(\ell,z)} \\ & / \sum_{\ell,z} \frac{1}{\Delta C^2_{gT}(\ell,z)/C^2_{gT}(\ell,z)}, \end{aligned} \tag{4-23}$$

which, for small Δz, yields

$$\begin{aligned} \frac{|\delta \mathrm{ISW}|}{\mathrm{ISW}} & \simeq \\ \frac{1}{2}\left|\sum_{\ell,z} \frac{\Delta z \cdot \partial C^2_{gT}(\ell,z)/\partial z}{\Delta C^2_{gT}(\ell,z)}\right| & / \quad \sum_{\ell,z} \frac{C^2_{gT}(\ell,z)}{\Delta C^2_{gT}(\ell,z)} \\ & \lesssim 3\ \Delta z, \end{aligned} \tag{4-24}$$

where we used Eqs. (4-8-4-10) to estimate the numerical value of the above expression. Since the optimum signal-to-noise for an ISW detection is ~ 7, the redshift systematic errors may not dominate the errors if

$$\Delta z_{sys} \lesssim \frac{1}{3 \times 7} \simeq 0.05. \tag{4-25}$$

6. What does ISW tell us about Cosmology?

Let us study the optimum constraints that an ISW cross-correlation detection can give us about cosmology. For a nominal concordance cosmology $\mathcal{C}_0$, the expected significance level for ruling out the cosmology $\mathcal{C}$, χ, is given by

$$\chi^2 = \sum_{\ell,z} \frac{[C_{gT}(\ell, z; \mathcal{C}) - C_{gT}(\ell, z; \mathcal{C}_0)]^2}{\Delta C^2_{gT}(\ell, z; \mathcal{C}_0)}, \tag{4-26}$$

where C_{gT} and ΔC_{gT} are defined in Eqs. (4-8-4-10). Note that the bias factor, b_g, is cancelled from the numerator and the denominator, and the optimum significance level only depends on the fluctuations in matter density and gravitational potential.

Fig. (4.6) shows the optimum constraints that an ISW detection may yield on some of the properties of dark energy, i.e. its density, equation of state, and speed of sound (For details of the cosmological perturbation theory with dark energy, see Gordon & Hu, 2004). While such constraints are already comparable to the current bounds on these parameters (Spergel et al., 2003; Tegmark et al., 2004a; Bean & Doré, 2004), future observations of CMB and large scale structure (e.g. Hu & Haiman, 2003; Song & Knox, 2003) will significantly improve these bounds. However, ISW constraints could still be used to test possible systematics that may affect the accuracy of future measurements.

It has been claimed (Garriga, Pogosian, & Vachaspati, 2004) that the cross-correlation observations could be used to break the degeneracies in the so-called doomsday cosmological scenarios, which involve a varying equation of state. However, given the cosmic variance limited measurements of the ISW effect (Eq. 5-29), it does not seem that such constraints can significantly improve the expected combined constraints from the upcoming Planck and SNAP satellite experiments (Kratochvil, 2004; Kratochvil, Linde, Linder, & Shmakova, 2003)

A more intriguing application of an ISW detection is the possibility of testing our theories of matter/gravity on large scales (Lue, Scoccimarro, & Starkman, 2004). While the consistency of the power spectrum of 2dF and SDSS galaxy surveys (Tegmark, Hamilton, & Xu, 2002; Tegmark et al., 2004b) with the WMAP power spectrum confirms the consistency of the ΛCDM concordance cosmology at scales of $k \gtrsim 0.1\ h\ \mathrm{Mpc}^{-1}$, Fig.(4.7) shows that an ISW detection can do the same at scales of $k \sim 0.003 - 0.03\ h\ \mathrm{Mpc}^{-1}$. Therefore, current (Boughn & Crittenden, 2004; Nolta et al., 2004; Fosalba, Gaztañaga, & Castander, 2003; Fosalba & Gaztañaga, 2004; Scranton et al., 2003; Afshordi, Loh, & Strauss, 2004) and future observations of an ISW effect may confirm the consistency of our cosmological theories at the largest physical scales that they have ever been tested. While the cross-correlation statistics are almost free of systematic bias, the auto-correlation is often dominated by survey systematics on such scales.

7. Conclusions

In this paper, we study different aspects of the correlation between a galaxy survey and CMB sky, due to the ISW effect in a flat universe. The main source of noise is contamination by the primary CMB anisotropies. We see that, given this noise, most of the signal comes from $\ell \sim 20$, and $z \sim 0.4$ with negligible contribution from $\ell > 100$ and $z > 1.5$.

While the maximum significance level for an ISW detection is $\sim 7.5\sigma$ for a concordance ΛCDM cosmology, an all-sky survey with about 10 million galaxies within $0 < z < 1$ should yield an almost perfect ISW detection, at the $\sim 5\sigma$ level.

We show that, in order to achieve a cosmic-variance limited ISW detection, the systematic anisotropies of the galaxy survey must be below 0.1%, on the scale of ~ 10 degrees on the sky. Within this level of systematics, and given the current level of Galactic contamination in WMAP CMB maps ($\sim \mu K$), there should be a negligible over/underestimate of the ISW signal due to the systematic correlations of CMB and galaxy maps. We also argue that, while the random uncertainties in redshifts cannot significantly reduce the significance of an ISW detection, the systematic errors in redshift estimates need be less than 0.05, in order to achieve a cosmic-variance limited measurement.

It turns out that, due to the large noise induced by the primary anisotropies, the optimum constraints on the properties of dark energy from an ISW detection, are already comparable to the current accuracies, and will be outdone by future observations. However, the simplicity of the linear physics involved in the ISW effect, and the fact that the cross-correlation statistics are not biased by the systematics of CMB or galaxy surveys, makes ISW detection a useful indicator of possible systematics in more accurate methods.

Finally, we point out that the detection of the ISW effect provides a unique test of our concordance cosmological model on the largest physical scales that it has ever been tested.

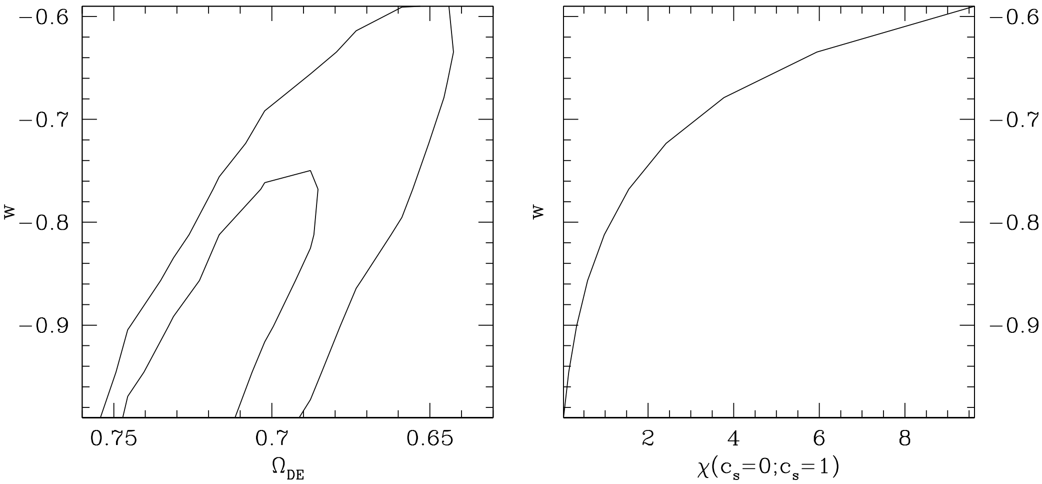

Fig. 4.6.— (Left) The $w - \Omega_m$ constraints (68% and 95% contours) based on an optimum ISW detection. (Right) The significance of ruling out $c_s = 0$, for a quintessence model with given w, and $c_s = 1$, based on an optimum ISW detection. In both graphs, other cosmological parameters are kept constant.

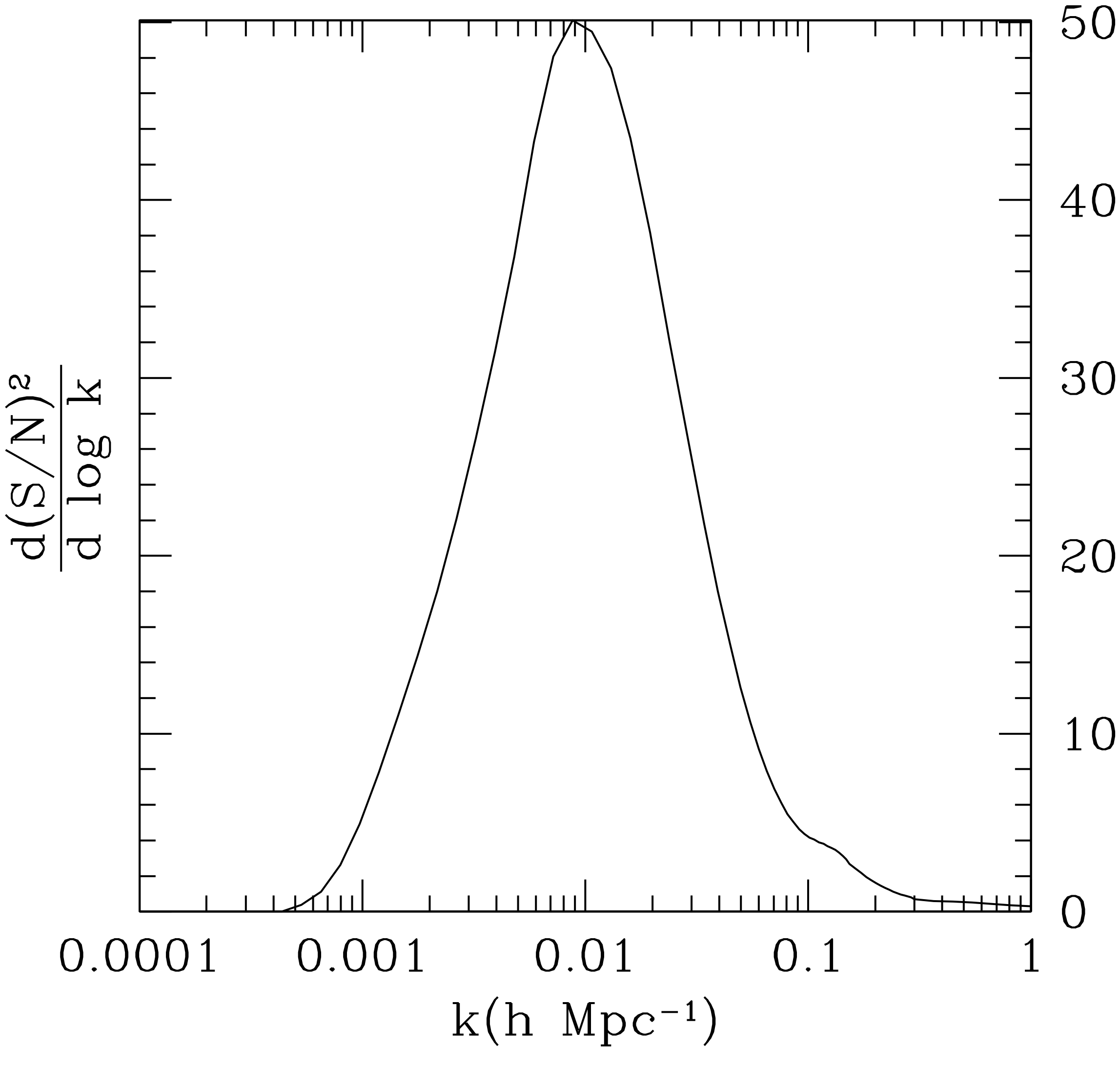

Fig. 4.7.— The distribution of $(S/N)^2$ of an ISW detection in k-space.

Bibliography

Abazajian, K., et al. 2003, AJ, 126, 2081

Afshordi, N., Loh, Y., & Strauss, M. A. 2004, Phys ReV D, 69, 083524 **(Chap. 3)**

Bean, R. & Doré, O. 2004, Phys ReV D, 69, 083503

Boughn, S. & Crittenden, R. 2004, Nature, 427, 45

Bennett, C. L., et al. 2003, ApJS , 148, 1 (Bennett et al. 2003a)

Bennett, C. L., et al. 2003, ApJS , 148, 97 (Bennett et al. 2003b)

Blanton, M. R., et al. 2003, ApJ , 592, 819

Cooray, A. 2002, Phys ReV D, 65, 103510

Crittenden, R. G. & Turok, N. 1996, Physical Review Letters, 76, 575

Fosalba, P., Gaztañaga, E., & Castander, F. J. 2003, Ap. J. Let. , 597, L89

Fosalba, P. & Gaztañaga, E. 2004, MNRAS , 350, L37

Garriga, J., Pogosian, L., & Vachaspati, T. 2004, Phys ReV D, 69, 063511

Gordon, C. & Hu, W. 2004, ArXiv Astrophysics e-prints, astro-ph/0406496

Hinshaw, G., et al. 2003, ApJS , 148, 135

Hu, W. & Dodelson, S. 2002, ARA&A, 40, 171

Hu, W. & Haiman, Z. 2003, Phys ReV D, 68, 063004

Kesden, M., Kamionkowski, M., & Cooray, A. 2003, Physical Review Letters, 91, 221302

Kratochvil, J. 2004, Private Communication

Kratochvil, J., Linde, A., Linder, E. V., & Shmakova, M. 2003, ArXiv Astrophysics e-prints, astro-ph/0312183

Lue, A., Scoccimarro, R., & Starkman, G. 2004, Phys ReV D, 69, 044005

Mukhanov, V. F., Feldman, H. A., & Brandenberger, R. H. 1992, Phys. Rep., 215, 203

Nolta, M. R., et al. 2004, ApJ , 608, 10

Peebles, P. J. & Ratra, B. 2003, Reviews of Modern Physics, 75, 559

Peiris, H. V. & Spergel, D. N. 2000, ApJ , 540, 605

Sachs, R. K. & Wolfe, A. M. 1967, ApJ , 147, 73

Schechter, P. 1976, ApJ , 203, 297

Schlegel, D. J., Finkbeiner, D. P., & Davis, M. 1998, ApJ , 500, 525

Scranton, R., et al. 2003, ArXiv Astrophysics e-prints, astro-ph/0307335

Song, Y. & Knox, L. 2003, ArXiv Astrophysics e-prints, astro-ph/0312175

Spergel, D. N., et al. 2003, ApJS , 148, 175

Smoot, G. F., et al. 1992, Ap. J. Let. , 396, L1

Tegmark, M., Hamilton, A. J. S., & Xu, Y. 2002, MNRAS , 335, 887

Tegmark, M., et al. 2004, Phys ReV D, 69, 103501 (Tegmark et al. 2004a)

Tegmark, M., et al. 2004, ApJ , 606, 702 (Tegmark et al. 2004b)

York, D. G., et al. 2000, AJ, 120, 1579

Chapter 5

WMAP constraints on the Intra-Cluster Medium

Abstract

We devise a Monte-Carlo based, optimized filter match method to extract the thermal Sunyaev-Zel'dovich (SZ) signature of a catalog of 100 low-redshift X-ray clusters from the first year data release of the Wilkinson Microwave Anisotropy Probe (WMAP). We detect an over-all amplitude for the SZ signal at the $\sim 7\sigma$ level, yielding a combined constraint of $f_{\rm gas}h = 0.07 \pm 0.01$ on the gas mass fraction of the Intra-Cluster Medium. We also compile X-ray estimated gas fractions from the literature for our sample, and show that they are consistent with the SZ estimates at the 2σ level. Nevertheless, our SZ estimated gas fraction is $30 - 40\%$ smaller than the concordance ΛCDM cosmic average.

Based on our analyses, we can also put an upper limit of 10^{28}erg/s/Hz on the average microwave luminosity of cluster galaxies in WMAP frequencies, and constrain the dark matter halo concentration parameter to $c_{\rm vir} = 3^{+3}_{-0.6}$, for clusters with $T_{\rm x} > 6$ keV.

1. Introduction

Clusters of galaxies are the largest relaxed concentrations of mass in the universe. They are interesting for cosmology as they probe the large scale structure of the universe (e.g., Mohr et al., 2002; Hu & Haiman, 2003), and they are interesting on their own, as we can resolve, probe, and study their inner structure in different frequencies, ranging from microwave to X-rays, and also through weak and strong gravitational lensing of background galaxies (e.g., Carlstrom, Holder, & Reese, 2002; Nichol, 2004; Markevitch, 2003; Hennawi & Spergel, 2004; Massey et al., 2004; Sand, Treu, Smith, & Ellis, 2004). What adds to this simplicity is that, at least for the massive clusters, almost all of the baryonic matter sits in the diffuse ionized Intra-Cluster Medium (ICM), which can be studied theoretically and observationally, with relatively simple physics, and give us a census of cosmic baryonic budget (see e.g., White, Navarro, Evrard, & Frenk, 1993; Evrard, 1997).

In this paper, we focus on the microwave signatures of galaxy clusters, the thermal Sunyaev-Zel'dovich (SZ) effect (Sunyaev & Zel'dovich, 1972), caused by the scattering of Cosmic Microwave Background (CMB) photons by hot gas in the diffuse ICM, and yielding characteristic spatial and spectral imprints on the CMB sky.

The thermal SZ effect has changed from the subject of theoretical studies to that of intense observational endeavor within the past decade, as various experiments have and are being designed to study this effect (see Bond, 2002, for an overview). The main reason behind this wide attention is the potential for using SZ detected clusters as standard candles to probe the cosmological evolution up to large redshifts (e.g., Haiman, Mohr, & Holder, 2001; Verde, Haiman, & Spergel, 2002). Compared to the SZ detection method, the X-ray detected clusters, which have been primarily used for this purpose until now (e.g., Henry, 2000; Vikhlinin et al., 2003; Henry, 2004), become much harder to detect at large redshifts, and are also believed to be more affected by complex astrophysics associated with galaxy formation, cooling or feedback within clusters (Carlstrom, Holder, & Reese, 2002).

Moreover, unlike X-ray observations which only sample regions of high gas density, thermal SZ observations probe the distribution of thermal energy in the cluster, and thus provide independent information about the over-all thermal history (Is there an entropy floor?; e.g., Voit, Bryan, Balogh, & Bower, 2002), and baryonic budget of the cluster (Are there missing baryons?; e.g., Cen & Ostriker, 1999).

Although various scaling relations of X-ray properties of clusters have been extensively studied in the literature, mainly due to the scarcity, incoherence, or low sensitivity of SZ observations of clusters, there have been only a few statistical analyses of SZ scaling properties in the literature (Cooray, 1999; McCarthy, Holder, Babul, & Balogh, 2003; Benson et al., 2004). Given the upcoming influx of SZ selected cluster catalogs, a good understanding of these scaling relations, and in particular, the SZ flux-Mass relation, which is of special significance for cosmological interpretations of these catalogs, is still lacking.

While the first year data release of the Wilkinson Microwave Anisotropy Probe (WMAP; Bennett et al., 2003a) has constrained our cosmology with an unprecedented accuracy, due to its low resolution and low frequency coverage, the SZ effect cannot be directly observed in the WMAP CMB maps (Huffenberger, Seljak, & Makarov, 2004). One possible avenue is cross-correlating CMB anisotropies with a tracer of the density (which trace clusters and thus SZ signal) in the late universe (Peiris & Spergel, 2000; Zhang & Pen, 2001). In fact, different groups have reported a signature of anti-correlation (which is what one expects from thermal SZ at WMAP frequencies) at small angles between WMAP maps and different galaxy or cluster catalogs, at a few sigma level (Bennett et al., 2003b; Fosalba, Gaztañaga,

& Castander, 2003; Fosalba & Gaztañaga, 2004; Myers et al., 2004; Afshordi, Loh, & Strauss, 2004). While thermal SZ is the clear interpretation of this signal, relating such observations to interesting cluster properties can be confused by the physics of non-linear clustering or galaxy bias.

An alternative method was used in (Hernández-Monteagudo & Rubiño-Martín, 2004; Hernandez-Monteagudo, Genova-Santos, & Atrio-Barandela, 2004), where they construct SZ templates based on given cluster or galaxy catalogs, and calculate the over-all amplitude of WMAP signal temperature decrement associated with that template. While the method yields significant SZ detections (2-5σ), the physical interpretation is complicated by the non-trivial procedure that they use to construct these templates.

In this paper, we follow the second line by devising an optimized filter match method based on an analytic model of ICM which is motivated by both numerical simulations and observations. We then apply the method to a sample of X-ray clusters, and construct templates of both SZ and potential point source contamination based on the X-ray temperatures of each cluster. Combining these templates with the WMAP maps yields constraints on the physical properties of our ICM model, namely the ICM gas mass fraction, and the dark matter halo concentration parameter.

While almost all the SZ observations up to date use an isothermal β model fit to the X-ray observations, in order to obtain the cluster SZ profile, it has been demonstrated that, as X-rays and SZ cover different scales inside the cluster, such extrapolation can lead to errors as big as a factor of 2 in the interpretation of SZ observations (Schmidt, Allen, & Fabian, 2004). Instead, Schmidt, Allen, & Fabian (2004) suggest using a physically motivated NFW profile (see §3) to model the X-ray and SZ observations simultaneously, which in their case, leads to consistent estimates of Hubble constant for three different clusters. We choose to follow their approach in choosing a physically motivated ICM model, rather than a mathematically convenient one.

We start in §2 by describing the WMAP CMB temperature maps and our compiled X-ray cluster catalog. §3 introduces our analytic ICM model, while §4 describes our statistical analysis methodology. In §5 we describe the results of our statistical analysis, listing the constraints on gas fraction, concentration parameter, and point source contamination of our clusters. At the end §6 discusses the validity of various assumptions that we made through the treatment, and §7 highlights the major results and concludes the paper.

Throughout the paper, we assume a ΛCDM flat cosmology with $\Omega_m = 0.3$, and $H_0 = 100h$ km/s/Mpc.

2. Data

2.1. WMAP foreground cleaned CMB maps

We use the first year data release of the observed CMB sky by WMAP for our analysis (Bennett et al., 2003a). The WMAP experiment observes the microwave sky in 5 frequency bands ranging from 23 to 94 GHz. The detector resolution increases monotonically from 0.88 degree for the lowest frequency band to 0.22 degree for the highest frequency. Due to their low resolution and large Galactic contamination, the two bands with the lowest frequencies, K(23 GHz) and Ka(33 GHz), are mainly used for Galactic foreground subtraction and Galactic mask construction (Bennett et al., 2003b), while the three higher frequency bands, which have the highest resolution and lowest foreground contamination, Q(41 GHz), V(61 GHz), and W(94

GHz), are used for CMB anisotropy spectrum analysis (Hinshaw et al., 2003). Bennett et al. (2003b) combine the frequency dependence of 5 WMAP bands with the known distribution of different Galactic components that trace the dominant foregrounds (i.e. synchrotron, free-free, and dust emission) to obtain the foreground contamination in each band. This foreground map is then used to clean the Q, V and W bands for the angular power spectrum analysis. Similarly, we use the cleaned temperature maps of these three bands for our SZ analysis. We also use the same sky mask that they use, the Kp2 mask which masks out 15% of the sky, in order to avoid any remaining Galactic foreground. However, we *stop short of* masking out the 208 identified WMAP point sources, as many of them happen to be close to our clusters. For example, there are 29 WMAP identified microwave sources within 3.6 degrees of 66 of our clusters. Instead, as we discuss in §3.2, we decide to model the point source contamination based on its frequency dependence.

The WMAP temperature maps and mask are available in HEALPix format of spherical coordinate system (Górski, Banday, Hivon, & Wandelt, 2002), which is an equal-area pixelization of the sphere. The resolution of the first year data is $N_{side} = 512 = 2^9$, implying $12 \times N_{side}^2 = 3,145,728$ independent data points (in lieu of masks) and $\simeq 0.1^\circ$ sized pixels, for each sky map.

2.2. Cluster Catalog

Our objective is to study the SZ signal in a large sample of galaxy clusters. To this end, we have assembled our sample from several existing X-ray cluster samples (Mohr et al., 1999; Reiprich & Böhringer, 2002; Finoguenov, Reiprich, & Böhringer, 2001; Sanderson et al., 2003; David et al., 1993; Jones & Forman, 1999), as X-ray observations may provide reliable cluster mass estimates, and avoid false detections due to chance projections. The selection criteria require that the clusters (1) must have *measured* X-ray emission weighted mean temperature ($T_{\rm x}$, defined below), (2) are reasonably away from the Galactic plane (Galactic latitude $|b| > 10°$), and (3) are at least 3 degrees away from the Galactic foreground Kp2 mask (§2.1).

The redshift information is obtained from NED and/or SIMBAD, and the above catalogs. The cluster temperature $T_{\rm x}$ is also from the literature cited above. We define the cluster center as the peak of the X-ray emission, either from the cluster catalogs or from archival *ROSAT* images. Our final cluster catalog contains 101 nearby clusters, ($0 \lesssim z \lesssim 0.18$), whose temperature ranges from 0.7 to 13 keV.

Our requirement that clusters have measured $T_{\rm x}$ is to ensure reliable mass estimates. Given $T_{\rm x}$, the observed mass-temperature relation (Finoguenov, Reiprich, & Böhringer, 2001, hereafter FRB01)

$$M_{500} = \left(1.78^{+0.20}_{-0.17} \times 10^{13} h^{-1} M_\odot\right) T_{\rm x}({\rm keV})^{1.58^{+0.06}_{-0.07}} \tag{5-1}$$

can be used to obtain $M_{500} \equiv (4\pi/3)500\rho_c r_{500}^3$, the mass enclosed by r_{500}, within which the mean overdensity is 500 times the *critical density* of the universe ρ_c. The wide range of cluster temperature in our sample implies that our clusters span two orders of magnitude in mass.

In order to facilitate comparisons of our SZ-derived gas fraction with the X-ray measurements, we compile the gas mass (within r_{500}) for all our clusters from the literature (Mohr et al., 1999; Sanderson et al., 2003; Jones & Forman, 1999). The gas masses provided by the latter studies are measured at a fixed metric radius of $0.5h^{-1}$ Mpc; we convert it to the nominal radius of r_{500} by the measured (or estimated) β-model profile, and then to r_{200} ($= r_{\rm vir}$; see §3), using the analytic model of §3.

Fig. (5.1) shows the distribution of redshifts and virial radii for our clusters (using the analytic model of §3 for $c = 5$). The solid lines show the resolution limits

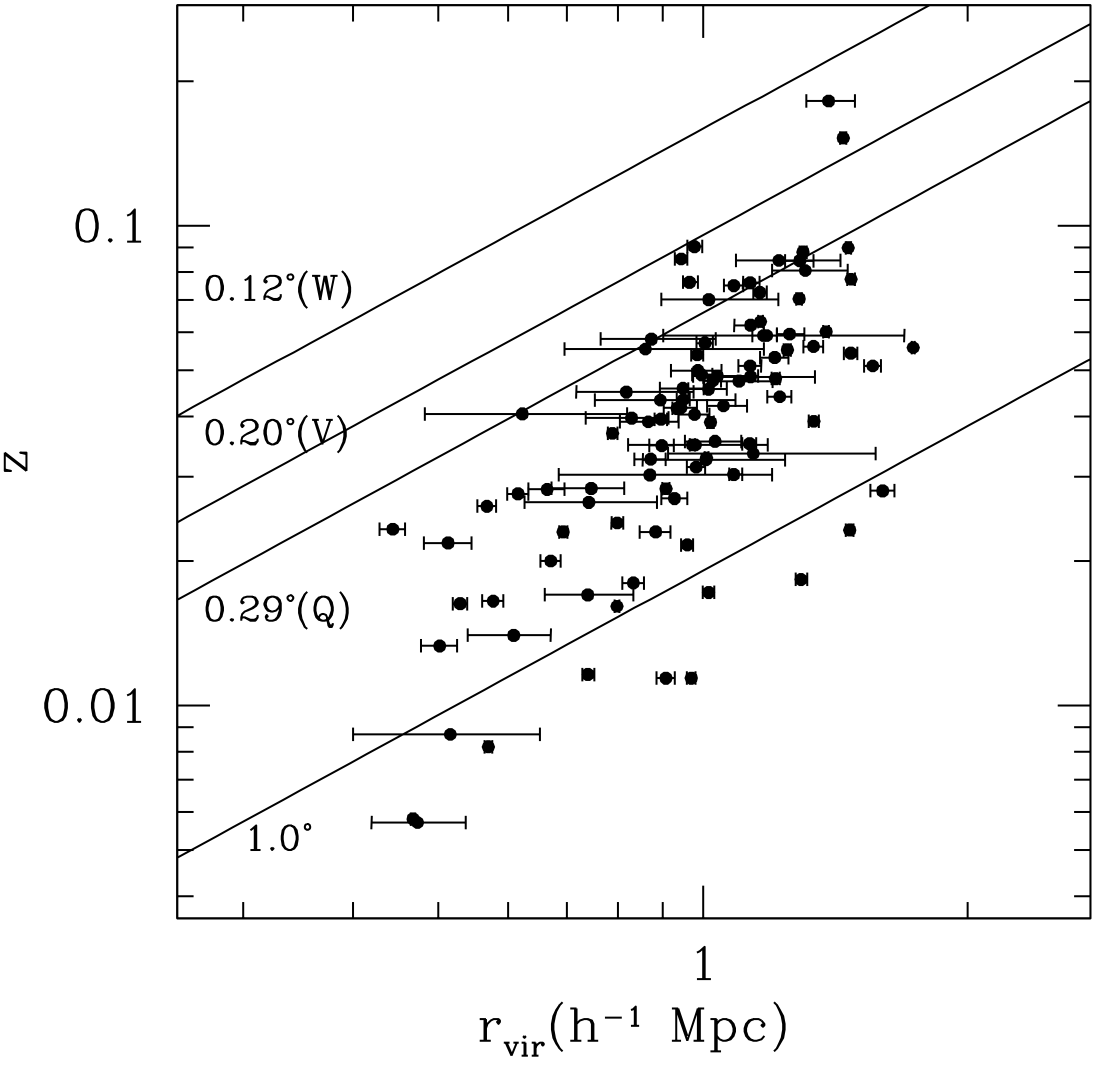

Fig. 5.1.— The distribution of cluster redshifts and virial radii (estimated from X-ray temperature, assuming $c = 5$; see §3). The three upper lines show the resolution of WMAP bands (associated with the radius of the disk with the same effective area as the detector beams; see Page et al., 2003), while the lower line shows the physical radius of the 1 degree circle at the cluster redshift.

of the three WMAP bands, as well as the physical radius of the 1 degree circle at the cluster redshift. We see that most of our clusters are in fact resolved in all the WMAP bands.

3. Analytic Modeling of the Intra-Cluster Medium

Numerical simulations indicate that the spherically averaged density distribution of dark matter, which also dominates the gravitational potential of galaxy clusters, may be well approximated by an NFW profile (Navarro, Frenk, & White, 1997, hereafter NFW)

$$\rho(r) = \frac{\rho_s}{(r/r_s)(1+r/r_s)^2}\ , \text{ for } r < r_{\rm vir} = c\, r_s, \tag{5-2}$$

where ρ_s and r_s are constants, and c, the so-called concentration parameter, is the ratio of $r_{\rm vir}$ to r_s. The virial radius, $r_{\rm vir}$, is defined as the boundary of the relaxed structure, generally assumed to be the radius of the sphere with an overdensity of $\Delta \simeq 200$ with respect to the *critical density* of the universe

$$\left(\frac{4\pi r_{\rm vir}^3}{3}\right)\left(\frac{3H^2}{8\pi G}\right)\Delta = M_{\rm vir} = \int_0^{cr_s} 4\pi r^2 dr\cdot\rho(r) = 4\pi\rho_s r_s^3\left[\ln(1+c) - c/(1+c)\right]. \tag{5-3}$$

Thus, fixing the mass of the cluster, $M_{\rm vir}$, and the concentration parameter, c, at a given redshift (which sets the critical density for given cosmology) fixes the dark matter profile (ρ_s and r_s), and the associated gravitational potential

$$\phi(r) = -\frac{GM_{\rm vir}}{r}\cdot\frac{\ln(1+r/r_s)}{\ln(1+c) - c/(1+c)}. \tag{5-4}$$

To model the distribution of the diffuse gas in the Intra-Cluster Medium (ICM), we assume that the gas follows a polytropic relation, i.e. $P_g(r) = \rho_g(r)T(r)/(\mu m_p) \propto [\rho_g(r)]^{\gamma_{\rm eff}}$, and that it satisfies Hydrostatic equilibrium in the NFW potential, which reduces to

$$\frac{d}{dr}\left[T(r) + \mu m_p(1-\gamma_{\rm eff}^{-1})\phi(r)\right] = 0. \tag{5-5}$$

Here, $P_g(r)$, $\rho_g(r)$, and $T(r)$ are gas pressure, density, and temperature respectively, while $\gamma_{\rm eff}$ is the effective polytropic index of the gas and m_p is the proton mass. $\mu = 4/(3+5X) \simeq 0.59$ is the mean molecular weight for a cosmic hydrogen abundance of $X \simeq 0.76$.

In order to integrate Eq. (5-5), we need to set the boundary condition for $T(r)$. Assuming an accretion shock at $r_{\rm vir}$ (Voit et al., 2003), which causes the cold infalling gas to come to stop, the gas temperature behind the shock should be $T(r_{\rm vir}) = \mu m_p v_{ac}^2/3$. In the spherical collapse model (Gunn, & Gott , 1972) $r_{\rm vir} \simeq 0.5 \times r_{ta}$, the turn-around radius, which implies $v_{ac}^2 = GM_{\rm vir}/r_{\rm vir}$, and respectively fixes $T(r)$

$$\frac{T(r)}{\mu m_p} \simeq -(1-\gamma_{\rm eff}^{-1})\left[\phi(r) - \phi(r_{\rm vir})\right] + \frac{GM_{\rm vir}}{3r_{\rm vir}}. \tag{5-6}$$

Note that, as our SZ signal is dominated by the most massive clusters (see §5), it is a fair approximation to neglect the non-gravitational heating/cooling processes, which only become significant for smaller clusters (e.g., Voit et al., 2003). Both simulations and observations seem to indicate that $\gamma_{\rm eff} \simeq 1.2$ (e.g., FRB01, Voit et al., 2003; Borgani et al., 2004, and refernces therein), and thus, for the rest of our analyses, we will use this value. Also, simulations only predict a weak mass dependence for the concentration parameter, c (e.g., NFW; Eke, Navarro, & Steinmetz, 2001; Dolag et al., 2004), and thus, for simplicity, we assume a mass-independent value of c.

Combining Eqs. (5-3),(5-4), and (5-6), we arrive at:

$$T(r) = \frac{\mu G M_{\rm vir} m_p}{r_{\rm vir}}\, f(r/r_{\rm vir}; c, \gamma_{\rm eff}), \tag{5-7}$$

where

$$f(x; c, \gamma_{\rm eff}) = \frac{1}{3} + (1 - \gamma_{\rm eff}^{-1}) \left[\frac{\ln(1 + cx)/x - \ln(1 + c)}{\ln(1 + c) - c/(1 + c)} \right], \tag{5-8}$$

and

$$r_{\rm vir} = \left(\frac{2\ GM_{\rm vir}}{H^2 \Delta} \right)^{1/3}. \tag{5-9}$$

The polytropic relation can be used to obtain the ICM gas density, $\rho_g(r) \propto [T(r)]^{1/(\gamma_{\rm eff}-1)}$, which yields

$$\rho_g(r) = f_{\rm gas} \left(\frac{M_{\rm vir}}{4\pi r_{\rm vir}^3} \right) g(r/r_{\rm vir}; c, \gamma_{\rm eff}), \tag{5-10}$$

where

$$g(x; c, \gamma_{\rm eff}) = \frac{[f(x; c, \gamma_{\rm eff})]^{1/(\gamma_{\rm eff}-1)}}{\int_0^1 [f(y; c, \gamma_{\rm eff})]^{1/(\gamma_{\rm eff}-1)}\ y^2 dy}, \tag{5-11}$$

and $f_{\rm gas}$ is the fraction of total mass in the ICM gas.

Now, let us obtain the observable quantities that are relevant to our study. Similar to previous works (e.g., Komatsu & Seljak, 2001), we approximate the observable X-ray temperature of clusters as the X-ray emission weighted gas temperature

$$T_{\rm x} \simeq \frac{\int T^{3/2}(r) \rho_g^2(r)\ r^2 dr}{\int T^{1/2}(r) \rho_g^2(r)\ r^2 dr} = \frac{\mu G M_{\rm vir} m_p}{r_{\rm vir}} \frac{\int_0^1 f^{3/2}(x) g^2(x)\ x^2 dx}{\int_0^1 f^{1/2}(x) g^2(x)\ x^2 dx}, \tag{5-12}$$

which should be contrasted with the virial (mass-weighted) temperature

$$T_{\rm vir} = \frac{\int T(r) \rho_g(r)\ r^2 dr}{\int \rho_g(r)\ r^2 dr} = \frac{\mu G M_{\rm vir} m_p}{r_{\rm vir}} \frac{\int_0^1 f(x) g(x)\ x^2 dx}{\int_0^1 g(x)\ x^2 dx}. \tag{5-13}$$

As an example, for a nominal value of $c = 5$, we find

$$T_{\rm x} = (9.9\ {\rm keV}) \left(\frac{M_{\rm vir}}{10^{15} h^{-1}\ {\rm M}_\odot} \right)^{2/3},\ \text{and}\ T_{\rm vir} = (7.6\ {\rm keV}) \left(\frac{M_{\rm vir}}{10^{15} h^{-1}\ {\rm M}_\odot} \right)^{2/3}, \tag{5-14}$$

which are weakly dependent on the value of c. We note that these relations are consistent, at the 10% level, with the predictions of the universal gas profile model by Komatsu & Seljak (2001). Observations of X-ray mass-temperature relation are often expressed in terms M_{500}, i.e. the mass enclosed inside the sphere with $\Delta = 500$ (see Eq. 5-3). For $c = 5$, Eq. (5-3) gives $M_{\rm vir} = M_{200} = M_{500}/0.722$, yielding

$$T_{\rm x} = (12.3 \text{ keV}) \left(\frac{M_{500}}{10^{15} h^{-1}\, {\rm M}_\odot}\right)^{2/3}, \tag{5-15}$$

which is consistent with the X-ray observations of massive clusters ($T_{\rm x} > 3$ keV; FRB01) [1]

$$T_{\rm x} = (11.8 \pm 1.4 \text{ keV}) \left(\frac{M_{500}}{10^{15} h^{-1}\, {\rm M}_\odot}\right)^{2/3}, \tag{5-16}$$

and thus, we will use Eq. (5-12) to relate the observed X-ray temperatures of our clusters to their virial masses and radii.

3.1. SZ profile

The contribution of the thermal SZ effect to the CMB temperature anisotropy (see Carlstrom, Holder, & Reese, 2002, for a review), at the frequency ν, is proportional to the integral of electron pressure along the line of sight

$$\delta T_{SZ}(\nu) = -\frac{\sigma_T\ T_{\rm CMB} F(h\nu/T_{\rm CMB})}{m_e c^2} \int P_e\ dr, \text{ where } F(x) = 4 - x\coth(x/2), \tag{5-17}$$

where σ_T is the Thomson scattering cross-section, and m_e is the electron mass. The SZ flux, defined as the integral of δT_{SZ} over the solid angle, $\delta\Omega$, is then given by

$$\overline{\delta T}_{SZ} \cdot \delta\Omega \equiv \int_{\delta\Omega} \delta T_{SZ}(\nu; \hat{\mathbf{n}})\, d^2\hat{\mathbf{n}} = -\frac{\sigma_T T_{\rm CMB} F(h\nu/T_{\rm CMB})}{m_e c^2} \int_{\delta\Omega} P_e(\mathbf{x}) \cdot d_A^{-2}(\mathbf{x})\, d^3\mathbf{x}. \tag{5-18}$$

---

[1] Borgani et al. (2004) argue that, on average, the beta model polytropic mass estimates overestimate masses by about 17%. We use this to correct for the observed mass-temperature relation in FRB01.

Here, d_A is the angular diameter distance, and $\mathbf{x}$ spans over the cone extended by the solid angle $\delta\Omega$. Now, assuming local thermal equilibrium

$$P_e = \left(\frac{2+2X}{3+5X}\right) P_g \simeq 0.52\ P_g, \tag{5-19}$$

the total SZ flux of a cluster is

$$\begin{aligned} S_{tot}(\nu) &= \overline{\delta T}_{SZ} \cdot \delta\Omega|_{tot} = -\frac{(1+X)\ \sigma_T\ T_{\rm CMB}\ F(h\nu/T_{\rm CMB})\ f_{\rm gas}\ M_{\rm vir}\ T_{\rm vir}}{2\ m_p\ m_e c^2\ d_A^2} \\ &= -(1.42\times10^{-2}\ {\rm mK})\,(0.1\ {\rm deg})^2 \left\{\frac{F(h\nu/T_{\rm CMB})\ f_{\rm gas}\ h}{[H_0 d_A(z)/c]^2}\right\} T_{\rm vir}({\rm keV}) \left(\frac{M_{\rm vir}}{10^{15} h^{-1}\,{\rm M}_\odot}\right), \end{aligned} \tag{5-20}$$

which can be combined with our analytic model (Eqs. 5-9, 5-12, and 5-13) to obtain

$$\begin{aligned} S_{tot}(\nu) &= -(2.16\times10^{-4}\ {\rm mK})\,(0.1\ {\rm deg})^2\ \left\{\tfrac{F(x)}{E(z)[H_0 d_A(z)/c]^2}\right\} T_{\rm x}^{5/2}({\rm keV})\,[B(c)\ f_{\rm gas}\ h] \\ &= -(1.63\times10^{-2}\ {\rm mJy})\ \left\{\tfrac{x^4\sinh^{-2}(x/2)F(x)}{E(z)[H_0 d_A(z)/c]^2}\right\} T_{\rm x}^{5/2}({\rm keV})\,[B(c)\ f_{\rm gas}\ h], \end{aligned} \tag{5-21}$$

where

$$x = h\nu/T_{\rm CMB}, \tag{5-22}$$

$$B(c) = \left(\frac{\int f\ g\ x^2 dx}{\int g\ x^2 dx}\right)\cdot\left(\frac{\int f^{3/2}\ g^2\ x^2 dx}{\int f^{1/2}\ g^2\ x^2 dx}\right)^{-5/2}, \tag{5-23}$$

$$E(z) = H(z)/H_0 = \left[\Omega_m(1+z)^3+\Omega_\Lambda\right]^{1/2}, \tag{5-24}$$

$$\text{and}\ \ H_0 d_A(z)/c = (1+z)^{-1}\int_0^z \frac{dz'}{E(z')}. \tag{5-25}$$

For the relevant range of $3 < c < 8$, $B(c)$ is a decreasing function of c which varies from 2.1 to 1.4. Note that all the factors in Eq. (5-21), with the exception of the last one, are fixed by observations. Therefore, $[B(c) f_{\rm gas} h]$ is the combination of model parameters which will be fixed by our SZ flux observations.

We then, use a Monte-Carlo method to reproduce the expected SZ flux of a given cluster. In this method, we equally distribute the total SZ flux of Eq. (5-21) among $N_{MC} = 4096$ random points, whose 3D density follow the ICM pressure, $P_g(r) \propto f(r/r_{\rm vir}) \cdot g(r/r_{\rm vir})$, around the center of a given cluster. While the method would be equivalent to exact projection in the limit $N_{MC} \to \infty$, the poisson error introduced due to a finite value of N_{MC} will be negligible comparing to the WMAP detector noise. The projected distribution of points should be then smeared by the WMAP beam window to get the expected distribution of the SZ flux. The expected SZ signal of the cluster in pixel i is proportional to n_i, the number of points that will fall into that pixel:

$$S_i(\nu) = \overline{\delta T}_{SZ,i} \cdot \delta\Omega_{\rm pixel} = \left(\frac{n_i}{N_{MC}}\right) \times S_{tot}(\nu). \tag{5-26}$$

3.2. Point Source Contamination

The frequency dependence of WMAP small angle anisotropies have been interpreted as a random distribution of point sources with a flat spectrum (i.e. Antenna temperature scaling as ν^{-2}; Bennett et al., 2003b). The majority of individually identified WMAP point sources are also consistent with a flat spectrum. Since the SZ signal has a small frequency dependence at the range of WMAP frequencies (41 GHz $< \nu <$ 94 GHz), we can use this frequency dependence to distinguish the point source contamination from the SZ signal. To do this, we assume a microwave point source with a flat (constant) luminosity per unit frequency, L_*, at each cluster galaxy, and that the galaxies follow the dark matter distribution (Eq. 5-2) inside each cluster. The total microwave flux associated with the point sources is then given by

$$\overline{\delta T}_{PS} \cdot \delta\Omega \equiv \int_{\delta\Omega} \delta T_{PS}(\nu; \hat{\mathbf{n}})\, d^2\hat{\mathbf{n}} = \frac{2h^2c^2}{k_B^3 T_{\rm CMB}^2} \cdot \frac{\sinh^2(x/2)}{x^4} \left(\frac{N_{\rm vir} L_*}{4\pi d_L^2}\right);\ x = \frac{h\,\nu}{k_B T_{\rm CMB}}, \tag{5-27}$$

where $N_{\rm vir}$ is the number of galaxies, above a certain magnitude limit, within the virial radius. For our analysis, we use the Lin, Mohr, & Stanford (2004) result for 2MASS near infrared selected galaxies:

$$N_{500}(M_K \leq -21) = 56 \pm 2 \left(\frac{M_{500}}{1.4 \times 10^{14} h^{-1}\, {\rm M}_\odot}\right)^{0.85 \pm 0.04}, \tag{5-28}$$

which can be extended to the virial radius, using the NFW profile. Thus, our L_* is defined as the total point source luminosity per unit frequency associated with the cluster, divided by the number of galaxies brighter than the near infrared K-band magnitude of -21, within the virial radius of the cluster.

4. Statistical Analysis Methodology

For a low resolution CMB experiment such as WMAP, the main sources of uncertainty in the SZ signal are the primary CMB anisotropies, as well as the detector noise. Since both of these signals are well described by gaussian statistics, we can write down the χ^2 which describes the likelihood of observing a given model of the cluster SZ+Points Source profile (see §3.1):

$$\chi^2 = \sum_{i,j;a,b} \left[T_{ia} - S_i(\nu_a)/\delta\Omega_{\rm pixel}\right] C^{-1}_{ia,jb} \left[T_{jb} - S_j(\nu_b)/\delta\Omega_{\rm pixel}\right], \tag{5-29}$$

where a and b run over WMAP frequency bands (i.e. Q, V, or W), and i and j run over the WMAP pixels. Here, T_{ia} and $S_i(\nu_a)$ are the observed temperature and expected SZ+Point Source flux in pixel i and band a, while $C_{ia,jb}$ is the covariance matrix of pixel temperatures:

$$C_{ia,jb} = n_{ia}^2 \delta_{ij}\delta_{ab} + \sum_{\ell} \left(\frac{2\ell+1}{4\pi}\right) |W_{\rm pixel}(\ell)|^2\, W_{\rm beam}(\ell;a) W_{\rm beam}(\ell;b)\, C_\ell P_\ell(\cos\theta_{ij}). \tag{5-30}$$

Here, n_{ia} is the pixel detector noise, $W_{\rm pixel}$ and $W_{\rm beam}$ are the HEALPix pixel and WMAP beam transfer functions (Page et al., 2003), while C_ℓ's and P_ℓ's are the primary CMB multipoles and Legendre polynomials respectively. We use CMBfast code (Seljak & Zaldarriaga, 1996) in order to generate the expected values of C_ℓ's for the WMAP concordance ΛCDM cosmology (Bennett et al., 2003a).

Note that WMAP detector noise only varies on large angular scales. Therefore, n_{ia} can be assumed to be almost constant if we limit the analyses to the neighborhood of a cluster, yielding

$$C_{ia,jb} \simeq \sum_\ell \left(\frac{2\ell+1}{4\pi}\right) |W_{\rm pixel}(\ell)|^2 \; K_{ab}(\ell) \; P_\ell(\cos\theta_{ij}), \tag{5-31}$$

$$K_{ab}(\ell) = W_{\rm beam}(\ell;a) W_{\rm beam}(\ell;b) \; C_\ell + n_a^2 \delta_{ab} \delta\Omega_{\rm pixel}, \tag{5-32}$$

where we used

$$\delta\Omega_{\rm pixel} \sum_\ell \left(\frac{2\ell+1}{4\pi}\right) |W_{\rm pixel}(\ell)|^2 P_\ell(\cos\theta_{ij}) = \delta_{ij}. \tag{5-33}$$

Now, it is easy to check that, in the small angle limit, we have

$$C^{-1}_{ia,jb} \simeq \delta\Omega^2_{\rm pixel} \sum_\ell \left(\frac{2\ell+1}{4\pi}\right) |W_{\rm pixel}(\ell)|^2 \; K^{-1}_{ab}(\ell) \; P_\ell(\cos\theta_{ij}), \tag{5-34}$$

We can again use the Monte-Carlo method, described at the end of §3.1, to evaluate $\mathbf{C^{-1}S} = \mathbf{C^{-1}W}_{\rm beam}\mathbf{S_0}$, where $\mathbf{S_0}$ is the raw projected SZ profile. To do so, instead of smearing $\mathbf{S_0}$ by the detector beam window, $\mathbf{W}_{\rm beam}$, we can smear $\mathbf{S_0}$ by $\mathbf{C}^{-1}\mathbf{W}_{\rm beam}$, which is given by

$$D_{ia,jb} = C^{-1}_{ia,kb} W_{{\rm beam};k,j;b} \simeq \delta\Omega^2_{\rm pixel} \sum_\ell \left(\frac{2\ell+1}{4\pi}\right) |W_{\rm pixel}(\ell)|^2 \; K^{-1}_{ab}(\ell) \; W_{\rm beam}(\ell;b) \; P_\ell(\cos\theta_{ij}). \tag{5-35}$$

Since the SZ signal is dominant at small angles, and at the same time we want to avoid the non-trivial impact of the CMB masks on the covariance matrix inversion, we cut off $D_{ia,jb}$ if the separation of pixels i and j is larger than $\theta_D = 3^\circ$. We do not expect this to impact our analysis significantly, as the CMB fluctuations are dominated by smaller angles. As $T_i = S_i/\delta\Omega_{\rm pixel}$ still minimizes χ^2, this truncation cannot introduce systematic errors in our SZ or point source signal estimates. However, it may cause an underestimate of the covariance errors. As we discuss in the §4.1, independent tests of covariance error should alleviate this concern.

The χ^2, given in Eq. (5-29) is quadratic in $B(c)f_{\rm gas}h$ and L_*, and thus, can be minimized analytically. After this minimization, the resulting χ^2 can be used to constrain the value of the concentration parameter c.

4.1. Error Estimates

While the covariance matrix obtained from the χ^2 in Eq. (5-29) gives a natural way to estimate the errors, our Monte-Carlo based approximation of the covariance matrix, as well as its truncation beyond $\theta_D = 3^\circ$, may reduce the accuracy of our error estimates.

In order to test the accuracy of our error estimates, we use our primary CMB power spectrum (from CMBfast), combined with the WMAP noise and beam properties to generate 99 Monte-Carlo Realizations of WMAP CMB maps in its three highest frequency bands (Q, V, & W). Neglecting the contamination of cluster signals by background points sources, these maps can then be used to estimate the error covariance matrix for our $f_{\rm gas}h$ and L_* estimators, within an accuracy of $\sqrt{3/99} \simeq 17\%$.

5. Results

In this section, we use the framework developed in §4 to combine the WMAP temperature maps with our cluster catalog. It turns out that about 30% of our clusters are within 3°, and about 8% within 1° of another cluster in our sample, implying possible correlations between the signals extracted from each cluster. However, in order to simplify the analysis and interpretation of our data, we ignore such possible correlations, and thus assume that the values of $f_{\rm gas}$ and L_*, obtained for each cluster is almost independent of the values for the rest of the sample. As we argue below, there is no evidence that this approximation may have biased our error estimates of global averages significantly.

One of our clusters (A0426) shows an 18σ ($L_* = (1.69 \pm 0.09) \times 10^{29}$erg/s/Hz/galaxy) signature for frequency dependent point source signal. It turns out that the 5th brightest microwave source, detected by the WMAP team (WMAP#94; NGC 1275) happens to be at the center of this cluster. As this point source overwhelms the SZ signal, we omit A0426 from our analysis, which leaves us with a sample of only 100 X-ray clusters.

5.1. Global ICM gas fraction and Point Source Luminosity

The most straightforward application of the statistical framework introduced in §4 is to obtain a global best fit for the gas fraction $f_{\rm gas}$ and galaxy microwave luminosity L_* for a given value of concentration parameter c. Table 5.1 shows the results of our global fits for a nominal value of $c = 5$ and different temperature cuts, which are compared with the estimates from our compiled X-ray observations. To get the X-ray gas fraction, the X-ray gas mass (§2.2) is divided by the virial mass estimated from observed $T_{\rm x}$ (Eq. 5-12).

While the overall significance of our model detections are in the range of $5 - 7\sigma$, we see that the significance of our SZ detection is $\sim 7\sigma$, and there is a signature of point source contaminations at 2.7σ level. Given that this value may be contaminated by the contribution of background sources, we can set an upper limit on the average microwave luminosity of cluster members

$$\langle L_* \rangle (60\text{ GHz}; M_K < -21) < 1.1 \times 10^{28} \text{erg/s/Hz/galaxy } (3\sigma), \tag{5-36}$$

Surprisingly, this number is very close to the diffuse (WMAP) V-band luminosity of Milky Way and Andromeda (Afshordi, Loh, & Strauss, 2004), which are ~ 2 and 4×10^{27}erg/s/Hz. *If a significant fraction of cluster members have a similar diffuse emission, this upper limit indicates that, on average, nuclear (AGN) activity cannot overwhelm the diffuse microwave emission from cluster galaxies.*

The errors obtained from our 99 Monte-Carlo realizations are generically within 20% of the covariance matrix error estimates, quoted in Table 5.1. Given the accuracy of the Monte-Carlo error estimates, we believe that they are consistent with the covariance errors. We should also note that there is a significant correlation between ($\sim 80\%$) between the errors in SZ and point source signals.

As an independent way of testing the accuracy of our error estimates, we can evaluate the χ^2 for the residuals of our global fit for $f_{\rm gas}h = 0.07 \pm 0.01$ (first row in Table 5.1). Our residual χ^2 is 94, which is within the expected range for 100 degrees of freedom, i.e. 99 ± 14. Since correlation of errors among close clusters may decrease this value, while systematic underestimate of errors tends to increase the residual χ^2, we conclude that, unless these two effects accidentally cancel each other, we do not see any evidence for either of these systematics.

Surprisingly, the average values of gas fraction estimated from X-ray observations and our SZ estimates are almost identical. However, as we limit the sample to higher X-ray temperatures, we see that X-ray estimated values become systematically larger than the SZ estimates. Despite the fact that our random errors are quite small and under control, the rather low value of $f_{\rm gas}h$ for our hottest (and thus most

Table 5.1: The global best fit values to the gas fraction and point source parameters for different temperature cuts, and assuming $c = 5$, compared with X-ray estimates (see the text). $\Delta\chi^2$ shows the relative significance of the best fit with respect to no-cluster model.

$f_{\rm gas}h$ (X-ray)	$f_{\rm gas}h$ (SZ)	$L_*(10^{28}$erg/s/Hz/gal)		#	$\Delta\chi^2$
0.071 ± 0.003	0.070 ± 0.010	0.50 ± 0.19	all clusters	100	-45.9
0.084 ± 0.003	0.063 ± 0.011	0.24 ± 0.25	$T_{\rm x} \geq 3$ keV	69	-39.9
0.096 ± 0.005	0.079 ± 0.013	0.82 ± 0.46	$T_{\rm x} \geq 5$ keV	31	-44.5
0.105 ± 0.006	0.076 ± 0.015	1.02 ± 0.50	$T_{\rm x} \geq 8$ keV	8	-28.4

massive) clusters may reflect systematic uncertainties in our theoretical modeling, or systematic bias in X-ray gas mass estimates. We will address this issue in §6. Nevertheless, the SZ detections are always consistent with the X-ray observations at the 2-σ level.

However, our gas fractions are significantly ($\sim 2.5\sigma$) lower than the cosmic average baryon fraction for ΛCDM concordance model (Spergel et al., 2003) $\Omega_b h/\Omega_m = 0.12 \pm 0.01$. If taken at the face value, this would imply that about $30 - 40\%$ of the baryons have been removed from the diffuse ICM.

5.2. Dependence on the Cluster Temperature

Let us study the dependence of our inferred cluster properties on the cluster X-ray temperature, which can also be treated as a proxy for cluster mass (Eq. 5-12). Since the errors for individual cluster properties are large, we average the them within 2 keV bins. The binned properties are shown in Figs. (5.2) & (5.3), and listed in Table 5.2. Similar to the previous section, we have also listed estimated gas fractions based on our compilation of X-ray observations.

Fig. (5.2) compares our SZ and X-ray estimated gas fractions. The dashed errorbars show the Monte-Carlo error estimates for our SZ observations, while the triangles are the X-ray estimates.

We first notice that the covariance matrix and Monte-Carlo estimated errors are consistent. However, similar to the global averages (Table 5.1), with the exception of first and last bin, our points are systematically lower than the X-ray gas mass estimates. Nevertheless, even for the four middle bins which show this systematic behavior, the χ^2 for the difference of X-ray and SZ bins is 8.8 which is just outside the 1-σ expectation range of 4 ± 3.5, for 4 random variables. Therefore, similar to §5.1, we again see that the signature for any discrepancy is less than 2-σ.

Another signature of consistency of our X-ray and SZ data points is the monotonically increasing behavior of gas fraction with $T_{\rm x}$. Indeed, this behavior has been observed in other X-ray studies (e.g., Mohr et al., 1999; Lin, Mohr, & Stanford, 2003), and has been interpreted as a signature of preheating (Bialek, Evrard, & Mohr, 2001) or varying star formation efficiency (Bryan, 2000).

Fig. (5.3) shows that, after removing A0426, none of our bins show more than 2-σ signature for point sources. The fact that the observed amplitude of point sources changes sign, and is consistent with zero implies that any potential systematic bias of the SZ signal due to our modeling of point sources (§3.2) must be negligible.

5.3. Constraining the Concentration Parameter

It is clear that the assumption of $c = 5$, which we made up to this point, is an oversimplification. In fact the average value of the concentration parameter is known to be a weak function of cluster mass in CDM simulations ($\propto M^{-0.1}$; e.g., NFW,

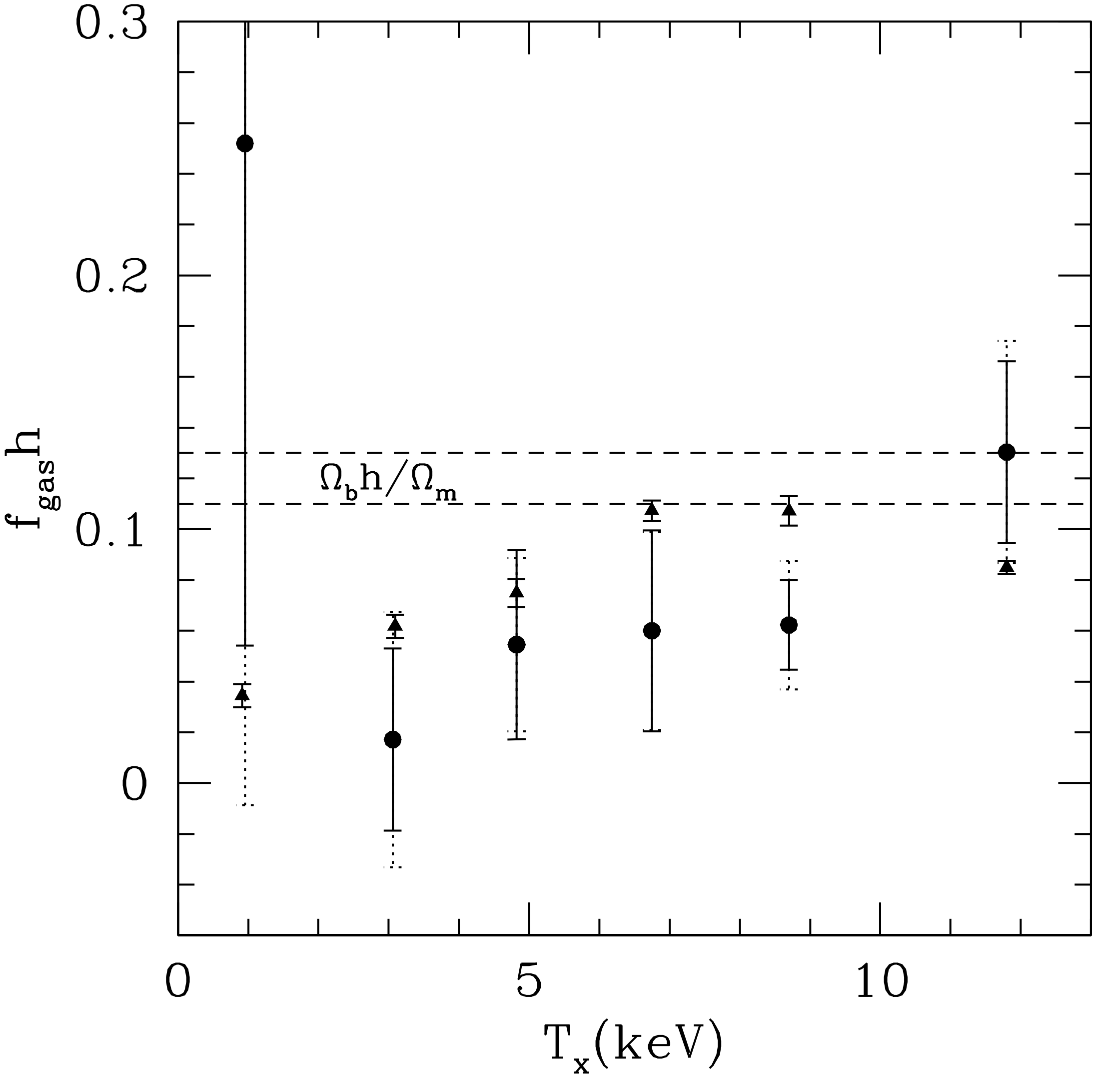

Fig. 5.2.— The binned values of gas fractions, inferred from our SZ measurements (assuming $c = 5$). The solid circles/errorbars show the covariance error estimated bins, while the dotted errorbars show the Monte-Carlo error estimates. The solid triangles are the X-ray estimates for $f_{\rm gas}h$ (see the text), while the region enclosed by the dashed lines is the upper limit from the WMAP concordance model (Spergel et al., 2003).

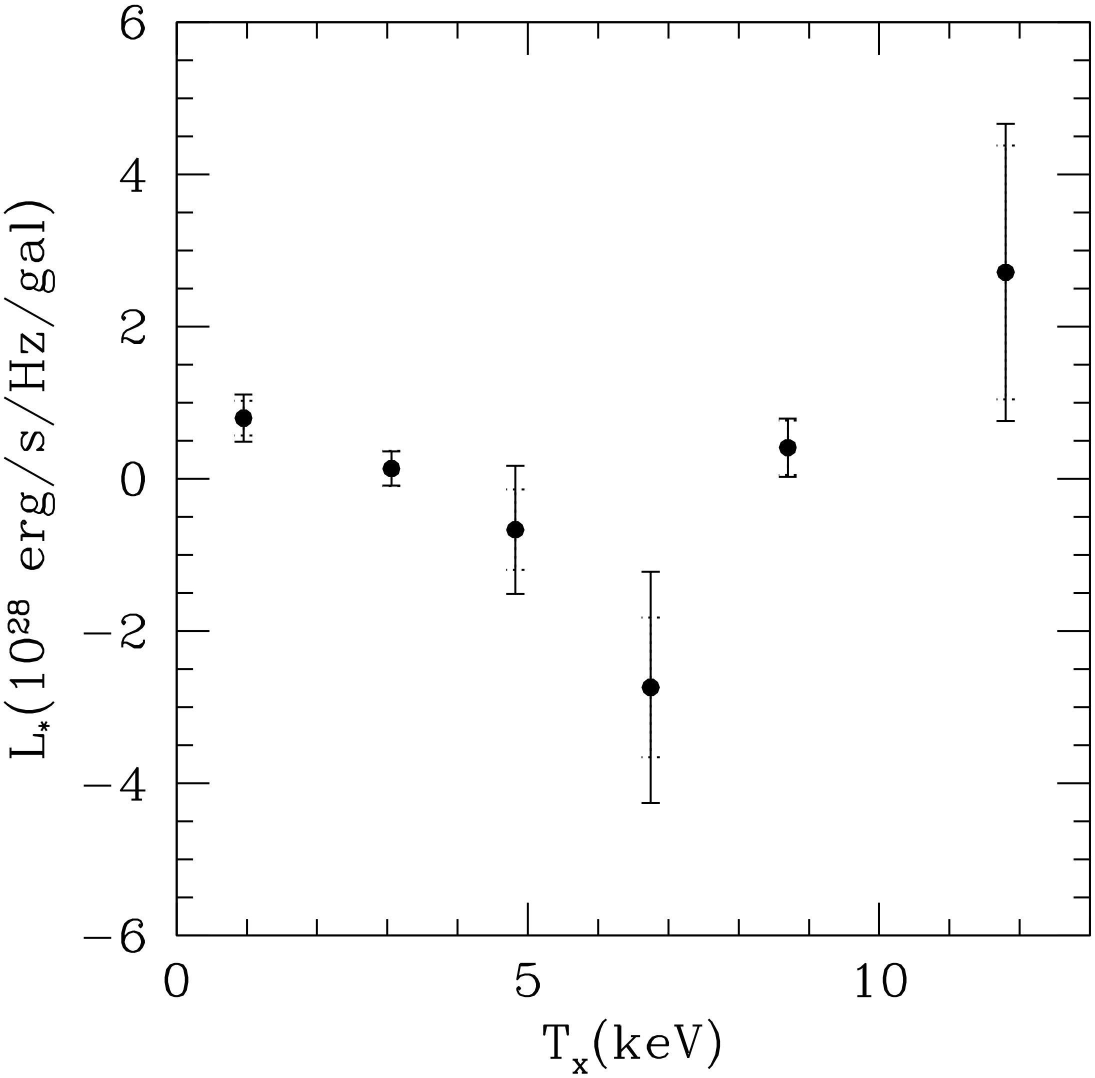

Fig. 5.3.— The binned values of the average microwave luminosity per galaxy, L_*, assuming a flat spectrum. The solid circles/errorbars show the covariance error estimated bins, while the dotted errorbars show the Monte-Carlo error estimates.

Table 5.2: The global best fit values to the gas fraction and point source parameters for different temperature bins, and assuming $c = 5$, compared with X-ray estimates (see the text). $\Delta\chi^2$ shows the relative significance of the best fit with respect to no-cluster model.

$f_{\rm gas}h$ (X-ray)	$f_{\rm gas}h$ (SZ)	$L_*(10^{28}$erg/s/Hz)	$T_{\rm x}$(keV)	$\overline{T}_{\rm x}$(keV)	#	$\Delta\chi^2$
0.034 ± 0.005	0.252 ± 0.197	0.77 ± 0.40	0-2	0.95	16	-4.0
0.062 ± 0.005	0.017 ± 0.036	0.17 ± 0.30	2-4	3.1	42	-0.4
0.075 ± 0.006	0.055 ± 0.037	-0.25 ± 1.21	4-6	4.8	23	-5.7
0.107 ± 0.004	0.060 ± 0.040	-3.04 ± 2.20	6-8	6.7	10	-16.9
0.107 ± 0.006	0.062 ± 0.018	0.75 ± 0.52	8-10	8.7	8	-13.8
0.085 ± 0.003	0.130 ± 0.036	4.31 ± 2.88	10-12	11.8	1	-17.4

Eke, Navarro, & Steinmetz, 2001), and even for a given mass, it follows a log-normal distribution (Bullock et al., 2001; Dolag et al., 2004), which may also depend on mass (Afshordi & Cen, 2002).

As discussed at the end of §4, we can repeat our Monte-Carlo template making procedure for different values of c, which yields analytic expressions for χ^2, and thus enables us to draw likelihood contours in the $f_{\rm gas}h - c$ plane. Since most of our signal is due to our hottest 19 clusters with $T_{\rm x} \geq 6$ keV (see Table 5.2), we restrict the analysis to this sample. Fig. (5.4) shows the result, where we have explicitly computed the χ^2 for integer values of c, and then interpolated it for the values in-between. The solid contours show our 68% and 95% likelihood regions. We see that our data only loosely constrains the concentration parameter of the dark matter halos, to $c_{\rm vir} = 3^{+3}_{-0.6}$. The dotted contours show the same likelihoods for the ΛCDM concordance model, which show its inconsistency with the SZ data at the 95% level.

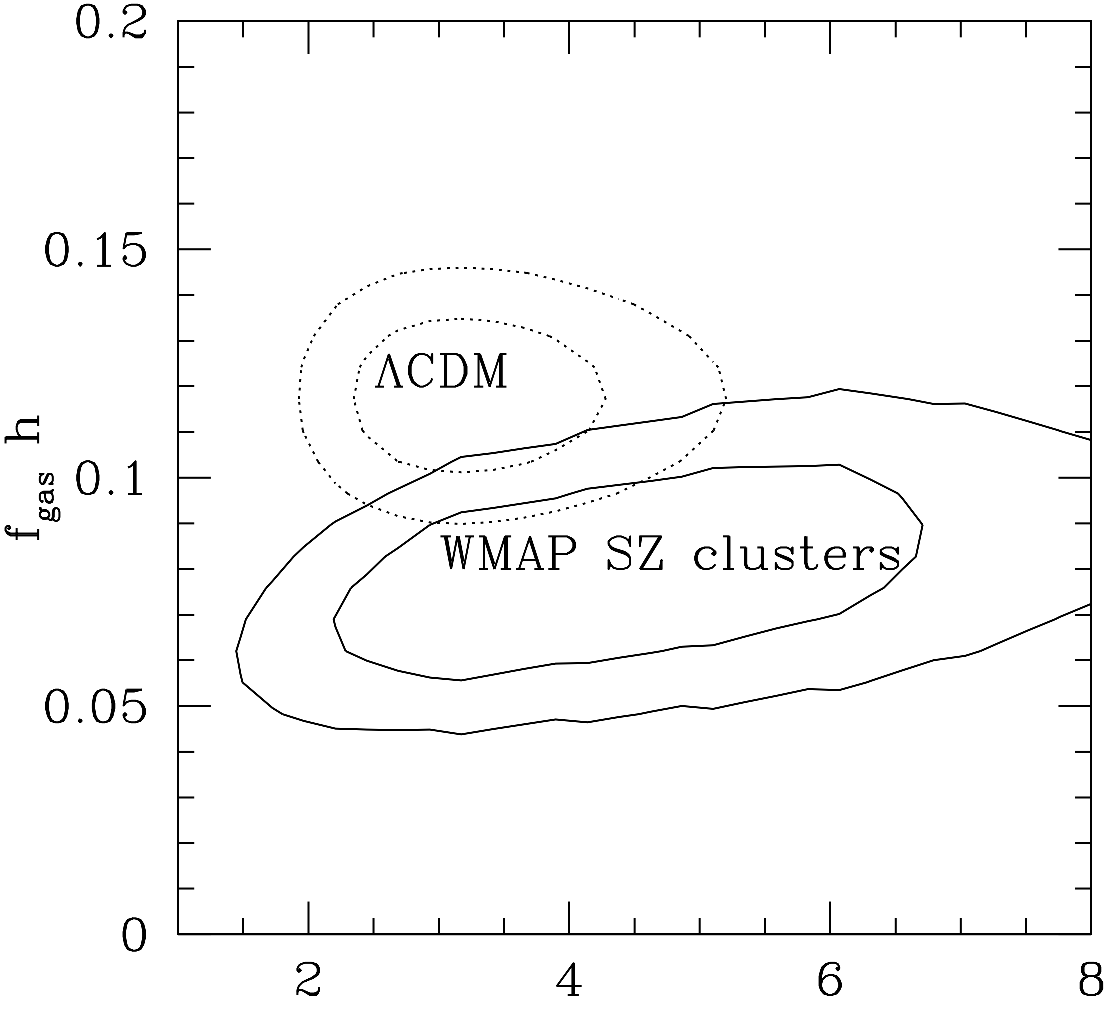

Fig. 5.4.— The 68% and 95% likelihood contours in the $f_{\rm gas}h - c_{\rm vir}$ plane for clusters with $T_{\rm x} \geq 6$ keV. The solid contours show the result from our SZ analysis, as described in the text. The dotted contours are for the ΛCDM concordance model, where $f_{\rm gas}h$ is quoted from Spergel et al. (2003), while the concentration parameter and its uncertainty are obtained in Afshordi & Cen (2002) and Dolag et al. (2004).

6. Discussions

6.1. ICM Gas Fraction

In §5, we demonstrated that, while we are able to detect the thermal SZ effect at the 7-σ level from the first year data release of WMAP temperature maps, the inferred gas fractions are typically smaller than the X-ray estimates, as well as the cosmological upper limit ($= \Omega_b h/\Omega_m = 0.12 \pm 0.01$). The SZ (as well as X-ray) observations have been often used, in combination with the nucleosynthesis bound on Ω_b, to constrain Ω_m, through replacing the upper limit by equality (Myers et al., 1997; Mason, Myers, & Readhead, 2001; Grego et al., 2001; Lancaster et al., 2004). Nevertheless, similar to our finding, such determinations have consistently yielded lower values than, the now well-established, upper limit. In fact, cooling and galaxy formation do lead to a depletion of the ICM gas. To make the matters worse, supernovae feedback can make the gas profile shallower, also leading to smaller baryonic fraction within a given radius. After all, clusters may not be such accurate indicators of the baryonic census in the universe.

X-ray only determinations of the ratio of cluster gas to virial mass have seemingly been more successful in reproducing the cosmic average (e.g., Lin, Mohr, & Stanford, 2003). However, we should note that, as the X-ray emissivity is proportional to the square of local plasma density, any smooth modeling of the ICM which may be used to infer the gas mass from the X-ray map of a cluster, tends to overestimate this value due to the contribution of unresolved structure to the X-ray emissivity (i.e. $\langle n^2 \rangle > \langle n \rangle^2$). The hydrodynamical simulations can suffer from the same problem, and thus fail to estimate the full magnitude of the effect. We believe this can be the reason for larger values of $f_{\rm gas}$ in X-ray observations, while the real ICM gas fractions may well be below the cosmic average.

6.2. Model Uncertainties

The relationship between the observed SZ flux and the ICM gas fraction (Eq. 5-21), relies on the accuracy of the (electron) virial temperature-mass relation (Eq. 5-13). Although our X-ray temperature-mass relation (Eq. 5-12) is consistent with observations, the (emission weighted) X-ray temperature only probes the inner parts of the cluster, and there can still be significant deviations from our simple picture of the uniform ICM in the cluster outskirts.

For example, Voit et al. (2003) argue that, compared to a uniform homogeneous accretion, inhomogeneous accretion will inevitably lead to smaller entropy production. Although this may not significantly affect the central part of a cluster, it can significantly change the boundary condition (see Eq. 5-6) behind the accretion shock. This can be also interpreted as incomplete virialization which can lead to smaller virial temperatures.

Another possibility is the breakdown of Local Thermal Equilibrium (LTE) in the cluster outskirts. While the hydrodynamic shocks heat up the ions instantly, the characteristic time for heating up the electrons (via Coulomb interactions) can be significantly longer (Fox & Loeb, 1997; Chieze, Alimi, & Teyssier, 1998; Takizawa, 1999), and thus the electron temperature can be lower by as much as 20% in the outer parts of clusters. Since the thermal SZ effect is proportional to the electron temperature, the breakdown of LTE can be a source low SZ signals. Interestingly, the effect is expected to be bigger for more massive clusters which have longer Coulomb interaction times.

6.3. Radio Source spectrum

While we assumed an exactly flat spectrum for all our point source contamination, a more realistic model would include a random spread in the spectral indices of the point sources. In fact, although the average spectral index of the WMAP identified sources is zero (flat; Bennett et al., 2003b), there is a spread of ~ 0.3 in the spectral index of individual sources. Moreover, although most of the bright microwave sources have an almost flat spectrum, an abundant population of faint unresolved sources may have a different spectral index, and yet make a significant contribution to the cluster microwave signal.

In order to test the sensitivity of our SZ signal to the point source spectrum, we repeat the analysis for the spectral power indices of -1 and 1. Our over-all SZ signal changes by less than 2%, implying the insensitivity of our results to the assumed spectrum.

7. Conclusions

In this work, using a semi-analytic model of the Intra-Cluster Medium, we devised a Monte-Carlo based optimal filter match method to extract the thermal SZ signal of identified X-ray clusters with measured X-ray temperatures. We apply the method to a catalog of 100 low redshift X-ray clusters, compiled from the literature, and detect the SZ signal, at $\sim 7\sigma$ level. We also see a 2.7σ signature for point source contamination, which we model based on the assumed spectral characteristics and spatial distribution of point sources.

The inferred point source signal puts the upper limit of 10^{28}erg/s/Hz/galaxy at the 3σ level, on the average microwave luminosity of cluster galaxies at $\nu \sim 60$ GHz.

While our observed SZ signal constrains the gas fraction of the Intra-Cluster Medium to $60 - 70\%$ of the cosmic average, it is systematically lower than, (although within 2σ of) the expected signal based on the X-ray estimated gas mass.

Bibliography

Afshordi, N. & Cen, R. 2002, ApJ , 564, 669

Afshordi, N., Loh, Y., & Strauss, M. A. 2004, Phys ReV D, 69, 083524 **(Chap. 3)**

Bennett, C. L., et al. 2003, ApJS , 148, 1 (Bennett et al. 2003a)

Bennett, C. L., et al. 2003, ApJS , 148, 97 (Bennett et al. 2003b)

Benson, B. A., Ade, P. A. R., Bock, J. J., Ganga, K. M., Henson, C. N., Thompson, K. L., & Church, S. E. 2004, ArXiv Astrophysics e-prints, astro-ph/0404391

Bialek, J. J., Evrard, A. E., & Mohr, J. J. 2001, ApJ , 555, 597

Bond, J. R. 2002, ASP Conf. Ser. 257: AMiBA 2001: High-Z Clusters, Missing Baryons, and CMB Polarization, 327

Borgani, S., et al. 2004, MNRAS , 348, 1078

Bryan, G. L. 2000, Ap. J. Let. , 544, L1

Bullock, J. S., Kolatt, T. S., Sigad, Y., Somerville, R. S., Kravtsov, A. V., Klypin, A. A., Primack, J. R., & Dekel, A. 2001, MNRAS , 321, 559

Carlstrom, J. E., Holder, G. P., & Reese, E. D. 2002, ARA&A, 40, 643

Cen, R. & Ostriker, J. P. 1999, ApJ , 514, 1

Chieze, J., Alimi, J., & Teyssier, R. 1998, ApJ , 495, 630

Cooray, A. R. 1999, MNRAS , 307, 841

David, L. P., Slyz, A., Jones, C., Forman, W., Vrtilek, S. D., & Arnaud, K. A. 1993, ApJ , 412, 479

Dolag, K., Bartelmann, M., Perrotta, F., Baccigalupi, C., Moscardini, L., Meneghetti, M., & Tormen, G. 2004, A & A , 416, 853

Eke, V. R., Navarro, J. F., & Steinmetz, M. 2001, ApJ , 554, 114

Evrard, A. E. 1997, MNRAS , 292, 289

Finoguenov, A., Reiprich, T. H., & Böhringer, H. 2001, A & A , 368, 749 (FRB01)

Fosalba, P., Gaztañaga, E., & Castander, F. J. 2003, Ap. J. Let. , 597, L89

Fosalba, P. & Gaztañaga, E. 2004, MNRAS , 350, L37

Fox, D. C. & Loeb, A. 1997, ApJ , 491, 459

Górski, K. M., Banday, A. J., Hivon, E., & Wandelt, B. D. 2002, ASP Conf. Ser. 281: Astronomical Data Analysis Software and Systems XI, 11, 107; http://www.eso.org/science/healpix/

Grego, L., Carlstrom, J. E., Reese, E. D., Holder, G. P., Holzapfel, W. L., Joy, M. K., Mohr, J. J., & Patel, S. 2001, ApJ , 552, 2

Gunn, J. E. & Gott, J. R. I. 1972, ApJ , 176, 1

Haiman, Z., Mohr, J. J., & Holder, G. P. 2001, ApJ , 553, 545

Hennawi, J. F. & Spergel, D. N. 2004, ArXiv Astrophysics e-prints, astro-ph/0404349

Henry, J. P. 2000, ApJ , 534, 565

Henry, J. P. 2004, ArXiv Astrophysics e-prints, astro-ph/0404142

Hernández-Monteagudo, C. & Rubiño-Martín, J. A. 2004, MNRAS , 347, 403

Hernandez-Monteagudo, C., Genova-Santos, R., & Atrio-Barandela, F. 2004, ArXiv Astrophysics e-prints, astro-ph/0406428

Hinshaw, G., et al. 2003, ApJS , 148, 135

Hu, W. & Haiman, Z. 2003, Phys ReV D, 68, 063004

Huffenberger, K. M., Seljak, U., & Makarov, A. 2004, ArXiv Astrophysics e-prints, astro-ph/0404545

Jones, C. & Forman, W. 1999, ApJ , 511, 65

Komatsu, E. & Seljak, U. 2001, MNRAS , 327, 1353

Lancaster, K., et al. 2004, ArXiv Astrophysics e-prints, astro-ph/0405582

Lin, Y., Mohr, J. J., & Stanford, S. A. 2003, ApJ , 591, 749

Lin, Y., Mohr, J. J., & Stanford, S. A. 2004, ArXiv Astrophysics e-prints, astro-ph/0402308

Markevitch, M. 2003, AAS/High Energy Astrophysics Division, 35

Mason, B. S., Myers, S. T., & Readhead, A. C. S. 2001, Ap. J. Let. , 555, L11

Massey, R., et al. 2004, AJ, 127, 3089

McCarthy, I. G., Holder, G. P., Babul, A., & Balogh, M. L. 2003, ApJ , 591, 526

Mohr, J. J., Mathiesen, B., & Evrard, A. E. 1999, ApJ , 517, 627

Mohr, J. J., O'Shea, B., Evrard, A. E., Bialek, J., & Haiman, Z. 2003, Nucl. Phys. Proc. Suppl. 124, 63, ArXiv Astrophysics e-prints, astro-ph/0208102

Myers, S. T., Baker, J. E., Readhead, A. C. S., Leitch, E. M., & Herbig, T. 1997, ApJ , 485, 1

Myers, A. D., Shanks, T., Outram, P. J., Frith, W. J., & Wolfendale, A. W. 2004, MNRAS , 347, L67

Navarro, J. F., Frenk, C. S., & White, S. D. M. 1997, ApJ , 490, 493 (NFW)

Nichol, R. C. 2004, Clusters of Galaxies: Probes of Cosmological Structure and Galaxy Evolution, 24

Page, L., et al. 2003, ApJS , 148, 39

Peiris, H. V. & Spergel, D. N. 2000, ApJ , 540, 605

Reiprich, T. H. & Böhringer, H. 2002, ApJ , 567, 716

Sand, D. J., Treu, T., Smith, G. P., & Ellis, R. S. 2004, ApJ , 604, 88

Sanderson, A. J. R., Ponman, T. J., Finoguenov, A., Lloyd-Davies, E. J., & Markevitch, M. 2003, MNRAS , 340, 989

Schmidt, R. W., Allen, S. W., & Fabian, A. C. 2004, ArXiv Astrophysics e-prints, astro-ph/0405374

Seljak, U. & Zaldarriaga, M. 1996, ApJ , 469, 437

Spergel, D. N., et al. 2003, ApJS , 148, 175

Sunyaev, R. A. & Zel'dovich, Y. B. 1972, Comments on Astrophysics and Space Physics, 4, 173

Takizawa, M. 1999, ApJ , 520, 514

Verde, L., Haiman, Z., & Spergel, D. N. 2002, ApJ , 581, 5

Vikhlinin, A., et al. 2003, ApJ , 590, 15

Voit, G. M., Bryan, G. L., Balogh, M. L., & Bower, R. G. 2002, ApJ , 576, 601

Voit, G. M., Balogh, M. L., Bower, R. G., Lacey, C. G., & Bryan, G. L. 2003, ApJ , 593, 272

White, S. D. M., Navarro, J. F., Evrard, A. E., & Frenk, C. S. 1993, Nature, 366, 429

Zhang, P. & Pen, U. 2001, ApJ , 549, 18